分类号_____ 密级_____

UDC_____ 编号_____

华中师范大学

博士学位论文

RHIC-STAR 固定靶金核金核碰撞中质子和轻核的产生

学位申请人姓名: 刘慧

申请学位学生类别: 全日制博士

申请学位学科专业: 粒子物理与原子核物理

指导教师姓名: 罗晓峰 教授

Norbert Herrmann 教授

许怒 教授

忠诚博雅，朴实刚毅

Dedicated to my family

谨献给我的家人

博士学位论文

论文题目：RHIC-STAR 固定靶金核金核碰撞中质子和轻核的产生

论文作者：刘慧

指导教师：罗晓峰 教授，
Norbert Herrmann 教授，
许怒 教授

学科专业：粒子物理与原子核物理

研究方向：相对论重离子碰撞物理

华中师范大学物理科学与技术学院

2024 年 5 月

Dissertation

Production of Protons and Light Nuclei in Au+Au Collisions with the STAR Detector at RHIC

By

Hui Liu

Supervisor: Prof. Xiaofeng Luo,

Prof. Norbert Herrmann, Prof. Nu Xu

Specialty: Particle Physics and Nuclear Physics

Research Area: Physics of Relativistic Heavy Ion Collision

College of Physical Science and Technology

Central China Normal University

May, 2024

华中师范大学学位论文原创性声明和使用授权说明

原创性声明

本人郑重声明：所呈交的学位论文，是本人在导师指导下，独立进行研究工作所取得的研究成果。除文中已经标明引用的内容外，本论文不包含任何其他个人或集体已经发表或撰写过的研究成果。对本文的研究做出贡献的个人和集体，均已在文中以明确方式标明。本声明的法律结果由本人承担。

作者签名：　　日期：2024 年 5 月 20 日

学位论文版权使用授权书

学位论文作者完全了解华中师范大学有关保留、使用学位论文的规定，即：研究生在校攻读学位期间论文工作的知识产权单位属华中师范大学。学校有权保留并向国家有关部门或机构送交论文的复印件和电子版，允许学位论文被查阅和借阅；学校可以公布学位论文的全部或部分内容，可以允许采用影印、缩印或其它复制手段保存、汇编学位论文。（保密的学位论文在解密后遵守此规定

保密论文严格按照《华中师范大学涉密研究生与涉密学位论文管理办法》进行管理。非保密论文注释：本学位论文不属于保密范围，适用本授权书。

因特殊情况需延期发布的论文，同意论文提交后延期 □ 半年；□ 一年；□ 二年发布。到期后适用本授权书。

作者签名：　　导师签名：

日期：2024 年 5 月 20 日　　日期：2024 年 5 月 20 日

Contents

摘　要

宇宙大爆炸理论认为，大约在 138 亿年前，整个宇宙起源于一个极端高能量的点，即所谓的奇点，其温度和密度是无穷大的。初始状态后的极短时间内，宇宙膨胀，温度和能量密度迅速下降。宇宙中的物质逐渐冷却和凝聚，形成各种基本粒子，如夸克、胶子、电子等。最终形成氢、氦等轻元素。夸克和胶子携带一种称为色荷的量子数，在自然界中，它们处于色禁闭状态，被束缚在强子内部。为了研究夸克和胶子之间的相互作用，1972 年，默里 · 盖尔曼 (Murray Gell-Mann) 和哈拉尔德 · 弗里奇 (Harald Fritzsch) 提出量子色动力学 (QCD) 理论。在高温高密下，强相互作用物质会发生相变 (QCD 相变)，此时禁闭在核子中的夸克、胶子将从核子中逃逸出来，形成由夸克和胶子组成的夸克胶子等离子体 (QGP)。QCD 的相结构被绘制在一张横坐标是重子化学势 (μ_B)，纵坐标是温度 (T) 的二维相图上。从第一性原理出发研究 QCD 理论的非微扰理论方法，格点 QCD 预测，在相图上的高温低重子密度区，从强子物质相到夸克胶子等离子体 (QGP) 相的转变是连续的平滑穿越。而在低温，高重子密度区，两相之间是一阶相变。一阶相变的终结点，被称为 QCD 临界点 (CP)。

相对论重离子碰撞实验为研究极端条件下 QCD 相图和强相互作用核物质的特性提供了独特的实验工具。实验上，利用不同加速能量加速初始重离子，获得不同的温度和重子化学势，从而探索 QCD 相图上不同区域的物质性质，寻找一阶相边界和临界点。在临界点附近，系统的关联长度 (ξ) 发散，此时系统中的局域重子数密度会出现不同程度的涨落。轻核 (至少包含一个中子和一个质子) 是在相对论重离子碰撞系统中可以被直接测量到的粒子。近年来，实验和理论上关于轻核的形成机制进行了大量的研究，其中核子合并模型和统计热力学模型是两个较为成功的理论。核子合并模型认为轻核是由碰撞末态系统中的质子和中子合并而成的，因此其产额与系统的体积，运动学冻结温度等密切相关。理论预言，轻核的产额比 ($N_t \times N_p/N_d^2$) 可以有效地消除单个轻核产额中的体积，温度等效应，与系统的中子数密度涨落直接相关，是探索 QCD 临界点和一阶相变的敏感观测量。

美国布鲁克海文国家实验室（BNL）的相对论重离子对撞机 (RHIC) 和欧洲核子研究中心 (CERN) 的大型强子对撞机 (LHC) 是进行相对论重离子碰撞实验的两个著名设施。STAR 探测器是目前 RHIC 上还在运行的主要探测器，从 2010 年至今，STAR 进行了第一能量扫描阶段，第二能量扫描阶段，以及固定靶模式下的金核 + 金核碰撞的数据采集。涵盖了质心系能

量$\sqrt{s_{\mathrm{NN}}}$ = 3.0 – 200 GeV，重子化学势 μ_B = 750 – 25 MeV 的大范围相图区域。为研究相图，寻找相边界和临界点提供了有利的条件。在 STAR 第一能量扫描 (BES-I) 阶段，即质心系碰撞能量为 7.7 – 200 GeV 范围内的研究发现，轻核复合产额比 ($N_t \times N_p/N_d^2$) 在 19.6 和 27 GeV 下 0-10% 的对心碰撞中呈现出能量依赖的非单调行为，该比值偏离理论基线有 4.1σ 倍的增强。本文主要针对质心碰撞能量$\sqrt{s_{\mathrm{NN}}}$ = 3.0 GeV 的实验数据开展了研究。系统测量了大快度范围的质子及轻核 (氘核、氚核、氦-3 和氦-4) 的横动量谱及产额, 并首次提取了全空间的积分产额。得到了对 QCD 临界点以及一阶相变敏感的轻核复合产额比。测量结果为进一步理解轻核的产生机制和高重子密度下的 QCD 相结构提供了重要实验依据。同时，利用爆炸波模型对质子和轻核的横动量谱进行拟合，提取了运动学冻结温度和平均横向膨胀速度，结果显示冻结参数与 7.7 – 200 GeV 对撞中的测量结果呈现出不同的中心度依赖趋势。暗示着 3 GeV 碰撞能量下产生的热致密介质可能与高能下产生的介质具有不同的状态方程。

本文首次测量了固定靶模式下金核 + 金核碰撞$\sqrt{s_{\mathrm{NN}}}$ = 3.0 GeV 的质子及轻核的产生。论文主要由以下部分组成：第 1 章是绪论，介绍了量子色动力学的基本信息以及本文的研究动机。第 2 章介绍了 RHIC-STAR 探测器，本研究用到的子探测器，以及固定靶模式的信息。第 3 章介绍了数据的选择和筛选，粒子的鉴别，效率修正，以及分析中各阶段系统误差的估计。第 4 章展示了分析结果，我们测量了质子 (p) 和轻核 ($d, t,^3$He, 和 ^{4}He) 在不同中心度和快度下的横动量 (p_T) 谱，计算了平均横动量及粒子产额的中心度和快度依赖。给出了粒子的全空间产额，计算了轻核的复合产额比，并与多个模型进行对比。第 5 章单独讨论了爆炸波模型的变种及拟合结果。第 6 章是关于 3 GeV 质子及轻核分析的总结和展望。在 3 GeV 的分析结果中我们发现，低能量所在的高重子密度区有很多与高能不同的物理信息，对研究系统的性质以及轻核的形成机制有着重要的意义。

关键词：量子色动力学；相对论重离子碰撞；临界点；轻核；全空间粒子产额；复合产额比。

Abstract

The Big Bang theory holds that approximately 13.8 billion years ago, the entire universe originated from an extremely high-energy point, known as the singularity. The temperature and density at this point of origin were infinite. Within a very short period of time after the initial state, the universe expanded, and its temperature and energy density dropped rapidly. The matter in the universe gradually cooled and condensed, to form various elementary particles such as quarks, gluons, electrons, and so on. These elementary particles further combine to form atoms, which in turn form light elements such as hydrogen and helium. Quarks and gluons carry a quantum number called the color charge, In nature, they are in a state of color confinement, bound inside hadrons. In order to study the interaction between quarks and gluons, in 1972, Murray Gell-Mann and Harald Fritzsch proposed the quantum chromodynamics (QCD) theory. At high temperatures and high densities, the strongly interacting matter will undergo a phase transition (QCD phase transition), at which time the quark and gluon confined in the nucleus will escape from the nucleus, forming a quark-gluon plasma (QGP) composed of quark and gluon. The phase structure of QCD is depicted on a two-dimensional phase diagram with the baryon chemical potential (μ_B) as the horizontal coordinate and the temperature (T) as the vertical coordinate. A non-perturbative theoretical approach to QCD theory from first principles, lattice QCD, predicts that in the high temperature (low baryon density) region of the phase diagram, the transition from the hadronic matter phase to the quark gluon plasma (QGP) phase is a continuous smooth traverse. In contrast, in the region of low temperature (high baryon density), there is a first-order phase transition between the two phases. The end point of the first-order phase transition is called the QCD critical point (CP).

Relativistic heavy-ion collision experiments provide a unique experimental tool for studying the quantum chromodynamics (QCD) phase diagram and the properties of strongly interacting nuclear matter under extreme conditions. Experimentally, the initial heavy ions are accelerated with different acceleration energies to obtain different temperatures and baryon chemical potentials. This enables the exploration of the material properties in various regions

of the QCD phase diagram, with the aim of searching for the first-order phase boundary and the critical point. The correlation length (ξ) of the system diverges near the critical point. At this juncture, there are fluctuations in the local baryon density to varying degrees. Light nuclei (containing at least one neutron and one proton) are particles that can be directly detected by detectors in relativistic heavy-ion collisions. In recent years, there has been a great deal of experimental and theoretical studies on the formation mechanisms of light nuclei, among which the coalescence model and the statistical thermodynamic model are two more successful theories. The coalescence model suggests that light nuclei are clusters formed by protons and neutrons in the final state of the collision system, and therefore their yield is closely related to the volume of the system, the kinematic freeze-out temperature, and so on. Theory predicts that the yield ratio of light nuclei ($N_t \times N_p/N_d^2$) can effectively eliminate the volume, temperature and other effects in the yield of a single light nucleus. It is directly related to the fluctuation of the neutron number density of the system and is a sensitive observation of the QCD critical point and the first-order phase transition.

The Relativistic Heavy Ion Collider (RHIC) at Brookhaven National Laboratory (BNL) in the United States and the Large Hadron Collider (LHC) at CERN are two renowned experimental facilities for relativistic heavy-ion collision. The STAR detector is the primary detector still in operation at RHIC. From 2010 to the present, STAR has collected data at Au + Au collisions in the first beam energy scan (BES-I), the second beam energy scan (BES-II), and the Fixed-target mode (FXT). It covers a wide range of the phase diagram area with center-of-mass collision energies $\sqrt{s_{\rm NN}}$ = 3.0 – 200 GeV and baryon chemical potential μ_B = 750 – 25 MeV. These extensive datasets provide favorable conditions for studying the phase diagram, searching for phase boundaries, and identifying critical points. In the BES-I at the STAR experiment, i.e., the center-of-mass collision energy range from 7.7 to 200 GeV, it was found that the light nuclei composite yield ratio ($N_t \times N_p/N_d^2$) exhibits an energy-dependent non-monotonic behavior in central collisions (0-10%) at 19.6 and 27 GeV, deviating from the theoretical baseline by an enhanced factor of 4.1σ. This study primarily focuses on data at center-of-mass collision energy $\sqrt{s_{\rm NN}}$ = 3.0 GeV. The transverse momentum spectra and yields of protons and light nuclei (deuterons, tritons, ^{3}He, and ^{4}He) are systematically measured over a wide rapidity range, and for the first time, the full phase-space yields (4π yields) are extracted. The study obtains composite yield ratios of light nuclei that are sensitive to the QCD critical point and the first-order phase transition. The measurement results provide important experimental basis for further understanding the production mechanism of light nuclei and the QCD phase structure at high baryon densities. Additionally, by fitting the transverse momentum spectra of protons and light nuclei using the blast-wave model, the kinetic freeze-out

temperature and average transverse expansion velocity are extracted. The results show that the freeze-out parameters exhibit a different centrality dependence trend compared to those measured in $\sqrt{s_{\rm NN}}$ = 7.7 – 200 GeV collisions. It is implied that the hot and density medium produced at 3 GeV collisions may have a different equation of state (EOS) compared to the medium produced at higher energies.

The thesis presents the first measurements of the protons and light nuclei production in FXT Au + Au collisions at $\sqrt{s_{\rm NN}}$ = 3.0 GeV. The thesis consists of the following parts: Chapter 1 is an introduction, which introduces the basic information of QCD and the motivation of this study. Chapter 2 introduces the RHIC-STAR detector, the sub-detectors used in this study, and information on the FXT mode. Chapter 3 includes the datasets and data selection, particle identification, efficiency correction, and estimation of systematic errors at each stage of the analysis. Chapter 4 shows the analysis results. We measured the transverse momentum (p_T) spectra of protons (p) and light nuclei ($d, t,^3$He, and ^{4}He) at different centralities and rapidities, calculated the centrality and rapidity dependence of average transverse momentum ($\langle p_T \rangle$)) and particle yield (dN/dy). The full phase space (4π) yield of particles is given. The compound yield ratio of light nuclei ($N_t \times N_p/N_d^2$, $N_{^4\rm He} \times N_p/\left(N_{^3\rm He} \times N_d\right)$, and $N_{^4\rm He} \times N_t \times N_p^2/\left(N_{^3\rm He} \times N_d^3\right)$) are calculated and compared with several models. Chapter 5 discusses the traditional blast-wave model and non-boost-invariant blast-wave model. Chapter 6 is a summary and outlook on the analysis. In this 3 GeV analysis, we have observed that the region of high baryon density at low energies contains a wealth of physical information distinct from high energies. This holds significant importance for the study of system properties and the formation mechanisms of light nuclei.

Keywords: Quantum Chromodynamics; Relativistic heavy ion collision; QCD critical point; Light nuclei; 4π particle yield; Compound yield ratio.

List of Figures

List of Tables

Chapter 1

Introduction

1.1 Standard Model

There are four fundamental interactions in nature: Strong Interaction, Electromagnetic Interaction, Weak Interaction, and Gravitational Interaction. The relative strengths of the four interactions, in terms of the strong interaction force, are shown in the Tab. 1.1.

Table 1.1: Relative strengths of the fundamental interaction forces [1].

Strong Interaction	Electromagnetic Interaction	Weak Interaction	Gravitational Interaction
1	$1/60 - 1/20$	10^{-13}	10^{-39}

The Standard Model of particle physics is an important tool for understanding particle physics and serves as a theoretical framework for describing strong nuclear force, electromagnetic force, and weak nuclear force. The Standard Model has successfully explained a wide range of experimental results and provides a comprehensive understanding of the fundamental particles that make up matter and their interactions.

The Standard Model contains 12 "flavors" of fermions, as shown in the left three columns of Fig. 1.1.1. Of the three particles that make up most matter: protons, neutrons, and electrons, only the electron is the fundamental particle of this theory. Protons and neutrons are simply composed of elementary quarks attracted by the strong force. These fermions can be divided into three generations. The first generation, shown in the first column on the left of Fig. 1.1.1, consists of up quarks, down quarks, electrons, and electric neutrinos. All ordinary matter is made up of particles from this generation. The second and third columns are the second and

[1] https://zh.wikipedia.org/wiki/基本相互作用

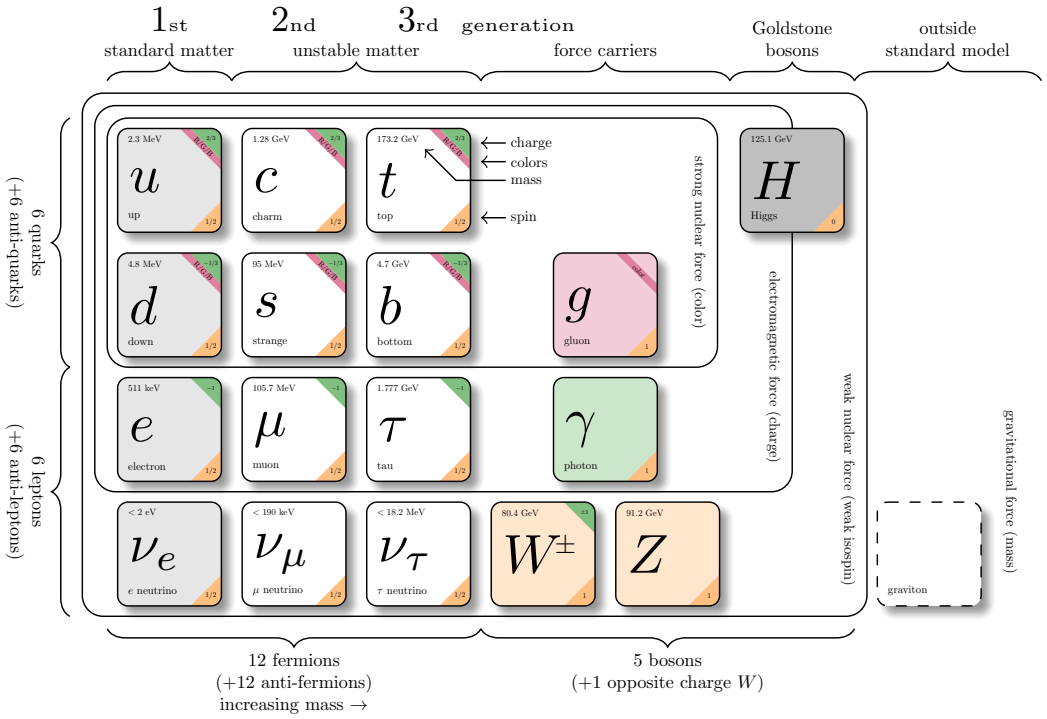

Figure 1.1.1: The standard model of elementary particles. Figure taken from [1].

third generations, respectively, which are unstable matter that can only be created by cosmic rays or high-energy experiments, and will decay into first generation particles within a short period of time. The two rows of fermions containing the up and down quarks, and considering the corresponding antiquarks and the three colors of each quark, there are 36 species of quarks in total. The two rows of fermions containing the electron and the electric neutrino are leptons, and considering the corresponding antiparticles, there are a total of 12 species of leptons. The column on the right is the gauge boson, which is responsible for transmitting various forces. On the far right is the Higgs particle, discovered in 2012 by Large Hadron Collider (LHC) at CERN. According to the Higgs mechanism, elementary particles gain mass due to coupling with the Higgs field. However, the Standard Model also has limitations. It cannot incorporate gravitational force, and cannot account for dark matter and dark energy, which together make up an important part of the mass and energy of the universe. In the future, it is necessary to continue exploring extensions and modifications to the standard model and to seek more comprehensive theories to address its shortcomings.

1.2 Quantum Chromodynamics

In 1972, Murray Gell–Mann proposed Quantum Chromodynamics (QCD) to describe the strong interaction [2]. It is a standard dynamic theory describing the strong interaction between quarks and gluons. It has two unique properties: color confinement and asymptotic freedom. At low energies, quarks and gluons interact strongly and they are confined in hadronic matter. For example, one quark and antiquark form a meson, and three quarks form a baryon. Asymptotic freedom is an important property of QCD discovered by David Jonathan Gross, Frank Anthony Wilczek, and Hugh David Politzer in 1973. They found that the strong interaction operates only over extremely short distances, whereas at long distance, the interaction between the color charges becomes weaker.

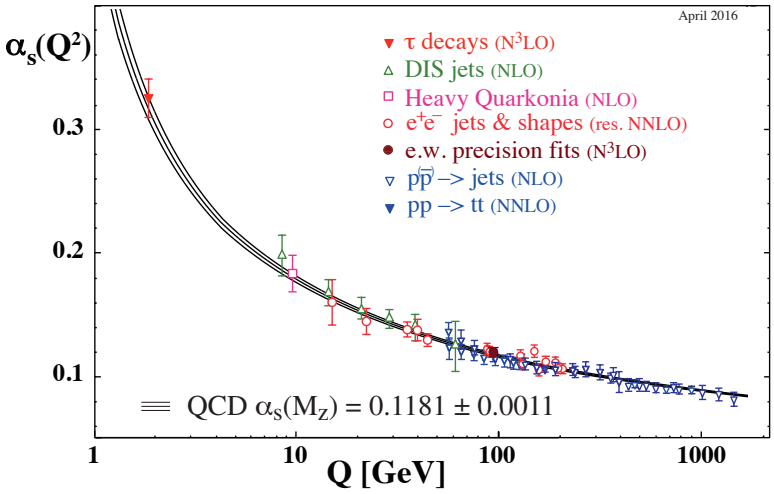

Figure 1.2.1: QCD coupling constant as a function of the energy scale Q. Figure taken from [3].

A parameter that describes the strength of the interaction between quarks and gluons, the quantum chromodynamic coupling constant [4] is expressed as

$$\alpha_s(Q^2) = \frac{g_s^2}{4\pi} = \frac{4\pi}{\beta_0 ln\frac{Q^2}{\Lambda^2}} \tag{1.2.1}$$

where $\beta_0 = (33 - 2N_f)/12\pi$, N_f is the quark flavor number, Λ is the QCD scale parameter, Q is the energy scale. α_s becomes larger at low energy scales, resulting in strong interactions between quarks and gluons, while at high energy scales, α_s becomes smaller due to asymptotic freedom, indicating that quarks and gluons move almost like free particles. As shown in Fig. 1.2.1, this conclusion has been confirmed both theoretically and experimentally.

1.3 QCD Phase Diagram and Critical Point

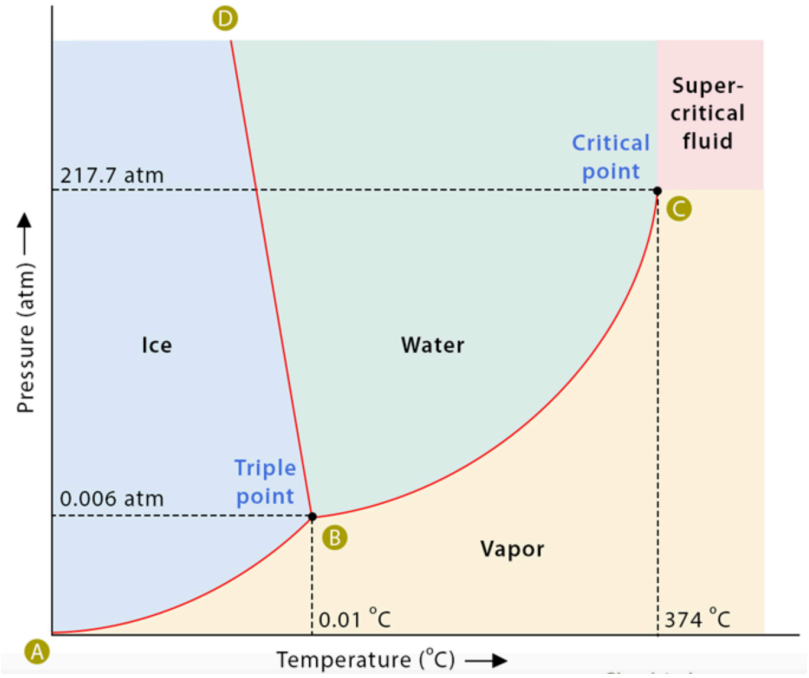

Figure 1.3.1: Phase diagram of water.

Phase transition is the process by which a substance changes from one phase to another. The phase transition behavior of water is a very common phenomenon in nature, extensively studied in both daily life and scientific research. The three phases of water are solid, liquid, and gas. To illustrate the relationship among the three phases, a water phase diagram is constructed, depicted in Fig. 1.3.1, where temperature is represented on the X-axis and pressure on the Y-axis. This diagram delineates the phase behavior of water under different temperature and pressure conditions. In the upper right corner of Fig. 1.3.1, there is a critical point (CP) at the end of the gas-liquid phase boundary. When the temperature and pressure increase and reach this point, it will be difficult to distinguish which state the water is in. This state is referred to as a supercritical fluid.

In the field of high energy physics, the study of phase diagrams also plays an important role. Nuclear matter driven by strong interactions can undergo phase transitions in low-energy heavy-ion collisions, as in the liquid-gas phase transition of water [6–9]. The QCD phase diagram is usually plotted on the temperature-baryon chemical potential plane [5], as shown in Fig. 1.3.2. The two color patches represent the hadronic matter phase and the Quark-

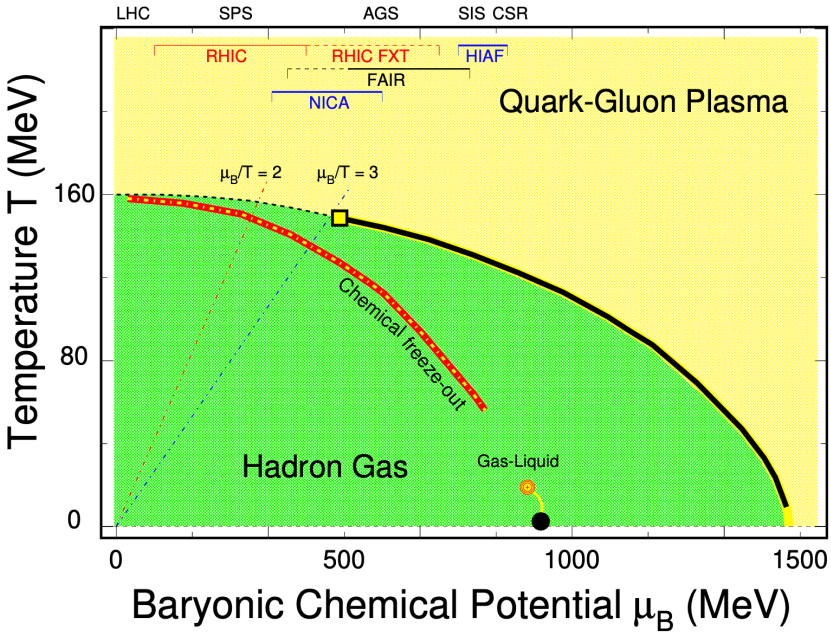

Figure 1.3.2: The QCD phase diagram of temperature T and baryon chemical potential μ_B. Figure taken from [5].

Gluon Plasma (QGP) phase respectively. At vanishing baryon chemical potential ($\mu_B = 0$ MeV), Lattice QCD [10–13] calculations reveal that the transition between hadronic matter and QGP is a smooth crossover at high temperature about $T = 150$ - 160 MeV (dashed line). At high baryon chemical potential, QCD-based models predict that there is a first-order phase transition (black solid line), and the first-order phase boundary line will terminate close to the smooth crossover, i.e., there is a critical point (open square) at the finite baryon chemical potential [9, 14–20]. The chemical freeze-out parameters extracted from the experiment by measuring the hadron yields are shown as the red line. Understanding the details of the QCD phase diagram, especially under high density and high temperature conditions, is challenging and has been an active area of research for a long time. The top of the phase diagram marks the regions on the phase diagram corresponding to different experimental collision energies.

1.4 Relativistic Heavy Ion Collision

Relativistic Heavy Ion Collisions (RHIC) aim to recreate the early moments of the universe, when temperatures and energy densities were unusually high just a few microseconds after the Big Bang, to study the properties of the quark-gluon plasma mentioned above. The RHIC at

Brookhaven National Laboratory (BNL) in the United States and the Large Hadron Collider (LHC) at CERN are two prominent facilities that conduct such experiments.

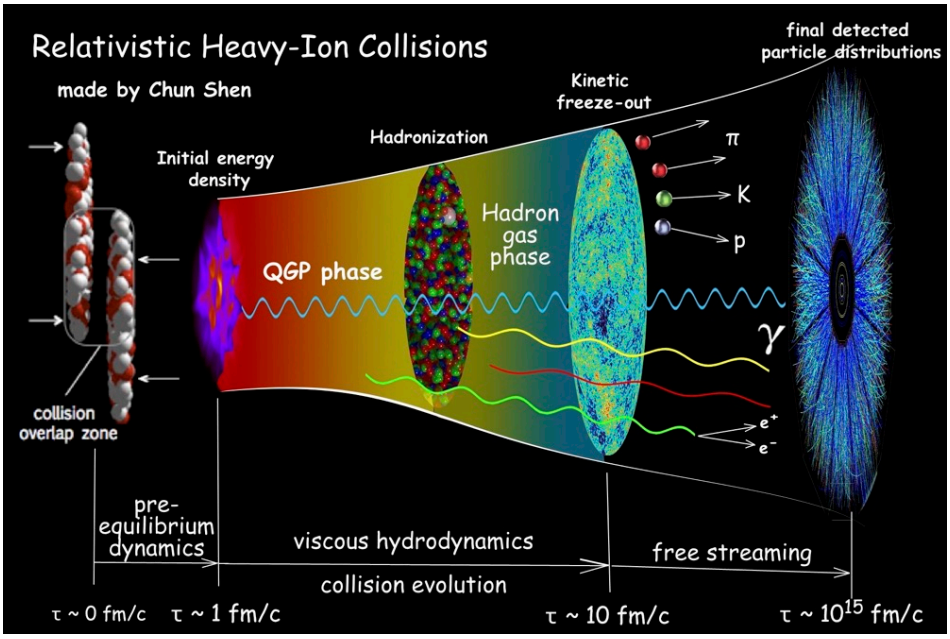

Figure 1.4.1: The time evolution of relativistic heavy ion collisions experiment. It comprises four phases: the initial state preceding the collision, the formation of quark-gluon plasma immediately after the collision, hadronization occurring as the quark-gluon plasma expands and cools down, and the freeze-out stage when the inelastic scattering process concludes. Figure taken from [21].

In these experiments, two nuclei moving in opposite directions are accelerated to nearly the speed of light. The Lorentz contraction causes the nuclei to assume a pancake-shaped form, as depicted in Fig. 1.4.1. When they collide at extremely high energies, it induces localized temperatures and energy densities of considerable magnitude. Under these conditions of high temperatures and densities, atomic nuclei disintegrate into quarks and gluons, forming a quark-gluon plasma. As the system undergoes expansion and cooling, the quarks and gluons subsequently recombine to form hadrons once again. In the process of hadronic evolution, the system continues to expand and cool, undergoing two stages of freeze-out. The first stage is chemical freeze-out, after which the types of hadrons are determined, and the system no longer undergoes inelastic collisions. The second stage is kinetic freeze-out, after which the momentum of the hadrons no longer changes, and elastic collisions cease. Ultimately, detectors positioned around the collision point capture the diverse particles generated in the collision. These data are then experimentally analyzed to gain insights into the formation and properties

of quark-gluon plasma.

1.5 Light Nuclei Production and Neutron Density Fluctuation

1.5.1 Light Nuclei

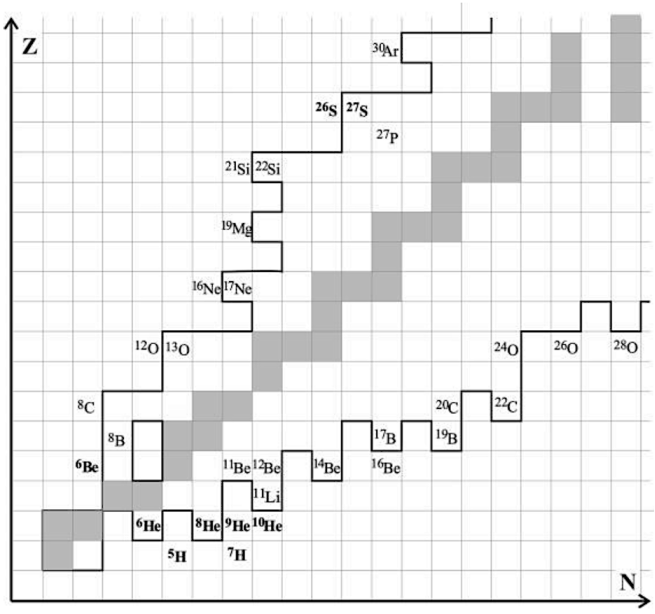

Figure 1.5.1: Light nuclei near the neutron/proton drip line. N is the number of neutrons, Z is the number of protons. The gray box outlines the stability interval. Figure taken from [22].

The term 'light nucleus' is subjective and typically denotes a nucleus with a relatively small number of nucleons (protons and neutrons) compared to heavier nuclei. Nuclei with a proton number less than 20 are generally considered to be light nuclei. In a nuclide diagram, where the number of neutrons (N) is represented on the X-axis and the number of protons (Z) on the Y-axis, as shown in Fig. 1.5.1, there are two boundary lines, called "nuclear drip lines". These two lines represent the proton-rich side and the neutron-rich side respectively. The area enclosed by these two lines signifies a relatively stable combination of neutrons and protons within the atomic nucleus. This diagram shows all stable light nuclei [22]. In a broad sense, light nuclei encompass elements such as Hydrogen (H), Helium (He), Lithium (Li), Beryllium (Be), Boron (B), and their corresponding isotopes. They are clusters containing at least one

proton and one neutron, and can be detected directly. Thus the study of light nuclei can explore nuclear forces and discover rich nuclear structures.

1.5.2 Neutron Density Fluctuation

Near the critical point, the correlation length ξ of fluctuations in the system increases sharply, and the spatial correlation tends to long-range correlation. This can be expressed in terms of correlation length by Eq. (1.5.1)

$$\xi = \xi_0 \left(T - T_c\right)^{-2/d} \tag{1.5.1}$$

where d is the space dimension, T_c is the critical temperature. This means that at critical point, the correlation length diverges due to $T = T_c$. The long-range interactions near the critical point give rise to a temporary, ordered structure on a finite scale, consequently leading to critical fluctuations in the system.

In heavy-ion collision, the higher order cumulants of conserved quantities, such as net-baryon (B) number, net-charge (Q) number, and net-strangeness (S) number, are highly sensitive to the correlation length. These are employed as sensitive observables in experiments to search for the QCD critical point and the first-order phase transition boundary [23–28]. Similarly, the neutron density fluctuation is a possible physical quantity to study the system evolution and to find phase boundaries and critical point. However, neutrons are uncharged and cannot be detected easily by detectors. Therefore, there is a need to find an observable that can reflect neutron density fluctuations. As mentioned before, light nuclei contain at least one neutron, so the measurement of light nuclei is considered as such an observable. The specific research methods and existing research results will be discussed in the Sec. 1.5.3.

1.5.3 History and Current Status of Light Nuclei Research

Clusters are very important in heavy ion collisions, not only because they are emitted, but also because the formation and existence of light clusters (with small binding energy, 2.24 MeV for d and 8.48 MeV for t) largely affect the global reaction dynamics and the properties of bulk nuclear species. Whether theoretically [29–34] or experimentally [35, 36], the study of light nuclei has a long history. In recent decades, the production of light nuclei and anti-nuclei has been measured in many experiments in heavy ion collisions, mainly the Schwerionensynchrotron (SIS) [37, 38], the Alternating Gradient Synchrotron (AGS) [39–46], the Super Proton Synchrotron (SPS) [47–53], the RHIC [54–62], and the LHC [63–73]. The energy regions of these experiments cover almost the entire QCD phase diagram. Theoretical

calculations propose the two most popular mechanisms, the nucleon coalescence [74–83] and thermal emission [84–87], to explain the production of light nuclei in heavy ion collisions.

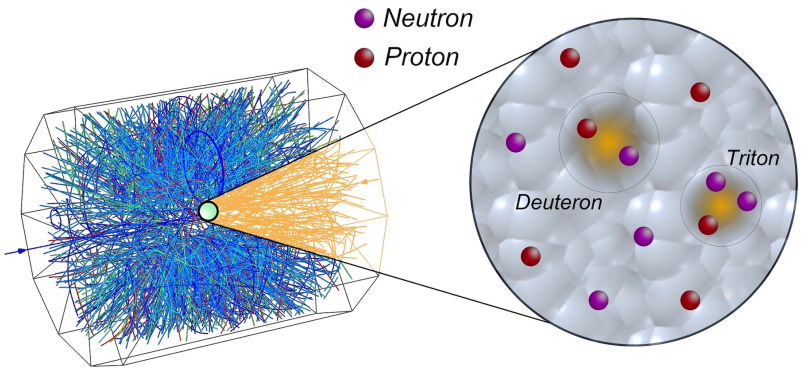

Figure 1.5.2: Schematic diagram of the nuclear coalescence in heavy-ion collisions.

In the picture of the coalescence model, the idea is that nucleons come together and "coalesce" to form a composite particle when the nucleons are close to each other in coordinate space and momentum space as shown in Fig. 1.5.2. Taking the deuteron as an example, the momentum distribution of the deuteron in this model is expressed as Eq. (1.5.2)

$$\frac{d^3N_d}{dp_d^3} = g\int d^3x_p d^3x_n d^3p_p d^3p_n \frac{d^6N_p}{dx_p^3 dp_p^3}\frac{d^6N_n}{dx_n^3 dp_n^3} \times f_W\left(\mathbf{x}_p', \mathbf{x}_n'; \mathbf{p}_p', \mathbf{p}_n'\right)\delta^{(3)}\left(\mathbf{p}_d - \mathbf{p}_p - \mathbf{p}_n\right) \tag{1.5.2}$$

where $g = 3/4$ is the statistical factor that is given by the spin of the nucleons and deuterons. $d^6N_p/dx_p^3dp_p^3$ and $d^6N_n/dx_n^3dp_n^3$ are the proton and neutron phase-space distributions. Assuming that the internal wave function of the deuteron is represented using the harmonic oscillator wave function, the Wigner function [88] of deuteron is

$$f_{\mathrm{W}}\left(\mathbf{x}_p', \mathbf{x}_n'; \mathbf{p}_p', \mathbf{p}_n'\right) = 8\exp\left(-\mathbf{p}^2\sigma^2 - \mathbf{x}^2/\sigma^2\right) \tag{1.5.3}$$

where $\sigma = 1/\sqrt{\mu\omega}$ and $\mu = m_N/2$ is the reduced mass. The relative coordinates and relative momentum of protons and neutrons are expressed as

$$\mathbf{x} = \mathbf{x}_p' - \mathbf{x}_n', \quad \mathbf{p} = \frac{1}{2}\left(\mathbf{p}_p' - \mathbf{p}_n'\right) \tag{1.5.4}$$

In the coalescence production mechanism, the spectral distribution of the composite nuclei

is related to the one of the primordial nucleons via

$$E_A \frac{d^3N_A}{d^3p_A} = B_A \left(E_p \frac{d^3N_p}{d^3p_p} \right)^Z \left(E_n \frac{d^3N_n}{d^3p_n} \right)^{A-Z} \tag{1.5.5}$$

where B_A is the coalescence parameter. The coalescence model describes the process by which nuclei are created from emitted nuclei as a hot fireball cools as it expands. The quantum mechanical mutation approximation [44, 89] is assumed and the density matrix form [75] is used, taking into account both the positions and moments of the nuclei. B_A can be related to the effective volume in coordinate space with $B_A \propto (1/V_{eff})^{A-1}$. Experimental studies also clearly show the dependence of the light-nucleus yield (ratio) on the volume of the emitted fireball [42, 59, 83].

The conclusion that B_A is proportional to $(1/V_{eff})^{A-1}$ was also found in the thermal model, which assume that the system is at least in local thermal equilibrium, so that the production of single particles and composite particles is controlled by a single temperature and chemical potential. In the statistical thermal model [86, 90], based on the Eq. (1.5.6), the light nuclei yields (dN/dy) are sensitive to the chemical freeze-out temperature ($T_{\rm chem}$).

$$dN/dy \propto (2J_A + 1)\exp(-\frac{m_A - \mu_B}{T_{\rm chem}}) \tag{1.5.6}$$

where $2J_A + 1$ is the spin degeneracy factor [43, 91] for particles. However, research has found that the thermal model can successfully describe experimental results at high energies at LHC ($\mu_B \sim 0$) [86, 92], but has obvious deviations at lower energies. One potential explanation is the significant impact of hadronic rescatterings during the hadronic expansion phase.

Assuming that protons and neutrons have the same mass and that the density fluctuations are completely correlated, the coalescence model gives the relationship between compound yield ratio and neutron density fluctuation [90, 93, 94] with

$$\frac{N_p \times N_t}{N_d^2} = g\frac{1 + (1 + 2\alpha)\Delta n}{(1 + \alpha\Delta n)^2} \tag{1.5.7}$$

where the correlation coefficient (α) is 1 with above assumptions. $\Delta n = \langle(\delta n)^2\rangle / \langle n\rangle^2$ is the relative density fluctuation of neutrons. So far, the observation quantity of using light nuclei to find the first-order phase transition boundary and critical point of QCD has been proposed.

In RHIC BES-I, the STAR experiment measured the production of deuterons [59] and tritons [62] in Au+Au collisions at $\sqrt{s_{\rm NN}}$ = 7.7 – 200 GeV. An enhancement of $N_t \times N_p/N_d^2$ relative to the coalescence baseline was observed in the 0-10% central Au+Au collisions at

$\sqrt{s_{\rm NN}}$ = 19.6 and 27 GeV with a combined significance of 4.1σ [62]. To determine whether the enhancements are related to a first-order phase transition or CP, dynamical modeling of heavy-ion collisions with a realistic equation of state is needed to compare with the experimental data. In addition, it was observed that the yield ratio $N_t \times N_p / N_d^2$ monotonically decreases with increasing of the charged-particle multiplicity ($dN_{ch}/d\eta$) and exhibited a scaling behavior. The observed decreasing trend and scaling behavior can be nicely explained by coalescence models while the thermal model predicts an opposite trend. Thus, the systematic measurement of light nuclei production in heavy-ion collisions across a wide energy range serves as a valuable tool not only to probe the QCD phase structure, but also to gain insight into the underlying production mechanism.

1.6 Thesis Motivation

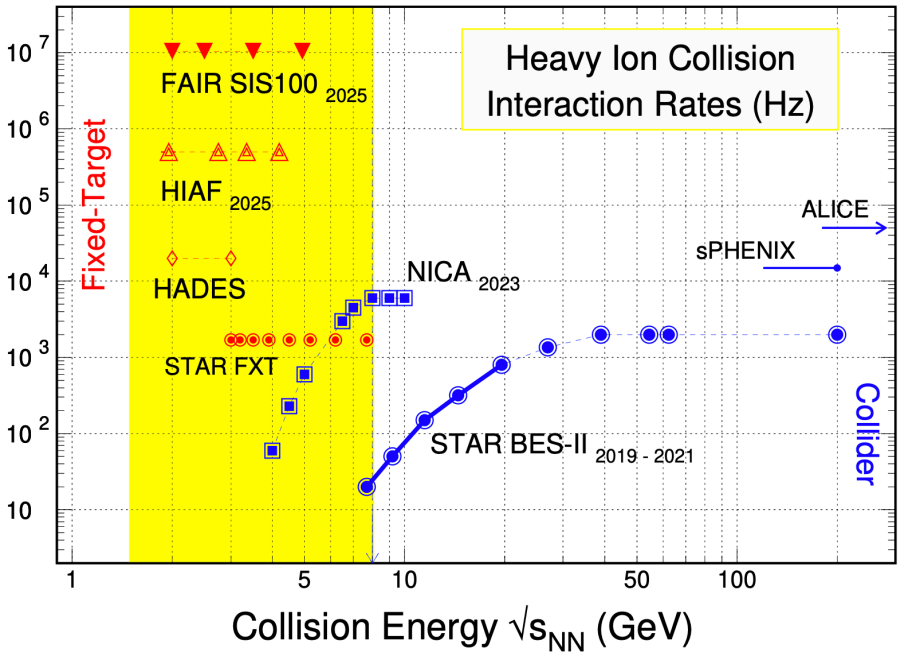

Figure 1.6.1: Interaction rates for heavy ion collision. Figure taken from [5].

A series of studies have shown that the QCD structure in the high baryon density region is complex and not yet understood. Reference [5] summarizes a series of physical observations. *Collectivity* (collective flow v_1 and v_2) show different trend at lower collision energies ($\sqrt{s_{\rm NN}}$ < 15 GeV). *Criticality* (fourth order fluctuations of net-proton $\kappa\sigma^2$ and light nuclei yield ratio

$N_t \times N_p/N_d^2$) show non-monotonic energy dependence in central Au+Au collisions, with a minimum and peak around 20 GeV, respectively.

As shown in Fig. 1.6.1, the RHIC STAR BES-II and FXT experiments focus on the lower energy (3 GeV $< \sqrt{s_{\rm NN}} <$ 20 GeV) range. This covers baryon chemical potential up to 750 MeV, providing us with a unique opportunity to explore the QCD phase structure. Therefore, our main work will focus on the production of light nuclei in high baryon density regions to provide more information for finding the critical point of QCD phase transition.

Chapter 2

Experiment Setup

2.1 Relativistic Heavy Ion Collider

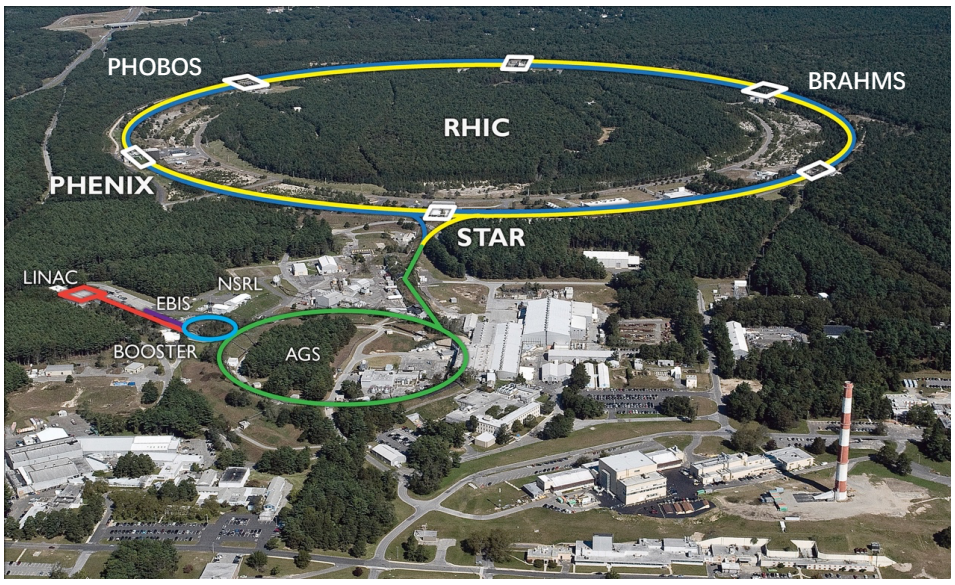

Figure 2.1.1: The Relativistic Heavy Ion Collider ring located in Brookhaven National Laboratory of the USA [95].

The Brookhaven National Laboratory [1], located on Long Island in the United States, is a

[1] https://www.bnl.gov

highly significant research laboratory for studying the evolution of cosmic matter. The Relativistic Heavy Ion Collider (RHIC) at this laboratory, depicted in Fig. 2.1.1, is considered the brightest proton spin polarization collider in the world. RHIC accelerates beams of particles (e.g., the nuclei of heavy atoms such as gold) to nearly the speed of light, and smashes them together to recreate a state of the process of high-temperature and high-density matter produced within a few microseconds after the Big Bang. By accelerating and colliding polarized protons, RHIC can explore how the proton gets its spin and intrinsic magnetism from its quark and gluon constituents. It provides physicists with the possibility to study the formation of matter in the universe.

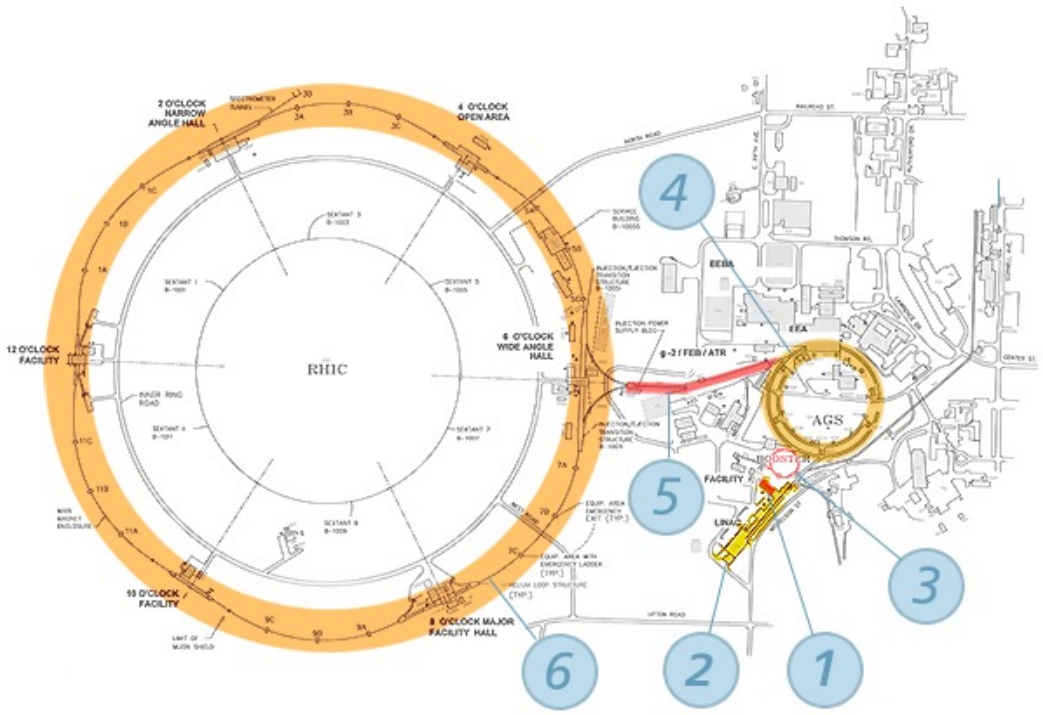

Figure 2.1.2: Detailed diagram of the RHIC particle accelerator [96]. 1: Electron Beam Ion Source (EBIS); 2: Linear Accelerator (Linac); 3: Booster Synchrotron; 4: Alternating Gradient Synchrotron (AGS); 5: Beamline; 6: RHIC ring.

The RHIC [96] complex is actually composed of a long "chain" of particle accelerators, shown in Fig. 2.1.2. Heavy ions are emitted from the Electron Beam Ion Source accelerator (EBIS), Subsequently, the ions progress to the circular Booster, where they undergo successive accelerations, reaching higher energy levels with each pass. The ions then enter the Alternating Gradient Synchrotron, where they are injected into two rings of the RHIC via a dedicated

beamline. Within the RHIC, the beam receives a final energy boost via radio waves. Once accelerated, the ions can "orbit" within the ring for a long time. As mentioned at the outset, RHIC is also equipped for collision beam experiments involving polarized protons, which undergo initial acceleration in the Linac and subsequent stages in the Booster, AGS, and RHIC.

The RHIC ring was completed in 1999 and has a circumference of approximately 2.4 miles. The ring includes four detectors, namely BRAHMS (located at 2 o'clock), STAR (located at 6 o'clock), PHENIX (located at 8 o'clock), and PHOBOS (located at 10 o'clock). The first physics program started in 2000, and over the past two decades, RHIC has successfully accelerated and collided with different beam types: p+p, p+Al, p+Au, He+Au, Cu+Cu, Cu+Au, Au+Au, U+U. These detectors take "snapshots" of collisions to reveal the basic components of visible matter, quarks and gluons. In 2020, the U.S. Department of Energy announced its plans to construct an Electron Ion Collider (EIC) [2] at BNL. They announced that the EIC will be a novel tool for exploring the inner microcosm dominated by gluons, to reveal the arrangement of the quarks and gluons that make up the protons and neutrons of nuclei [97].

2.2 STAR Detector System

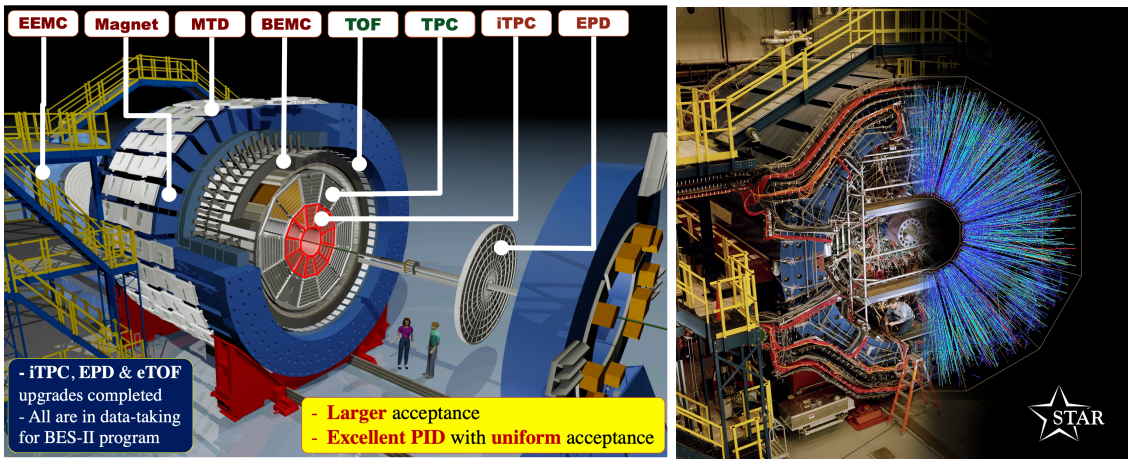

Figure 2.2.1: Left: STAR detector perspective view, cutaway to view internal detector system. Right: Beam's eye view of STAR detector [98].

The STAR detector holds a pivotal role in the heavy-ion collision detection systems situated along the RHIC ring, representing one of the few systems of its kind in the world. It has a very large and uniform acceptance, covering a broad azimuthal angle around the mid-rapidity.

[2] https://www.bnl.gov/eic/

Figure 2.2.1 left visually illustrates the STAR detector. The main purpose of the STAR experiment is to explore the existence of new states of matter at extremely high energy densities and to study quantum chromodynamics (QCD) phase structures. The detector has been carefully designed to utilize high spatial and temporal resolution for particle identification and momentum analysis, and can measure hadronic products with wide solid angles. Ultimately, the search for indications of quark-gluon plasma (QGP) phase transitions and the fundamental nature of the strong interaction at high energy densities is carried out by simultaneous measurements of various observables.

2.2.1 Time Projection Chamber

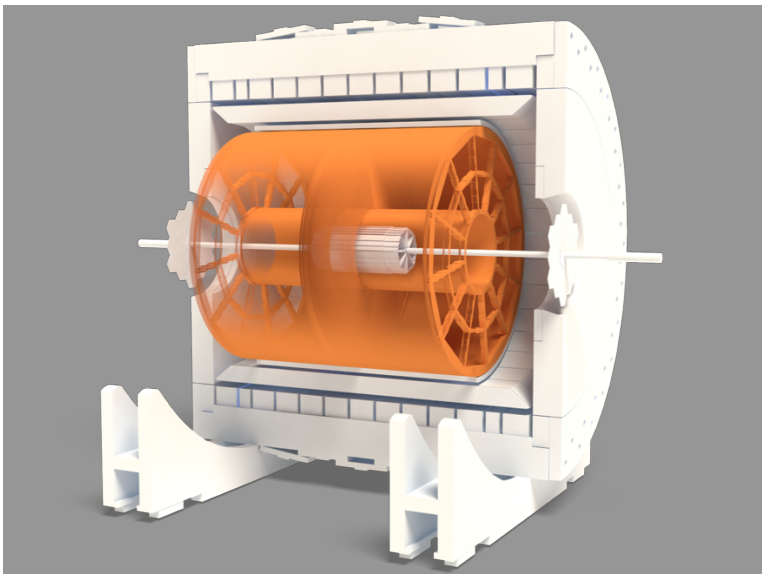

Figure 2.2.2: The Time Projection Chamber detector is a sub-detector of the STAR detector system, as shown by the orange cylinder in the figure. [3].

The Time Projection Chamber (TPC) [99] is a primary tracking device of STAR, it is the central element in a suite of detectors that surrounds the interaction vertex. As shown in Fig 2.2.2, which is placed in a large volume solenoid magnet with a magnetic field strength of 0.5 T. It is a cylinder with a length of 4.2 m and a diameter of 4 m as depicted in Fig. 2.2.3. A uniform drifting electric field with a field strength of about 135 V/cm is placed in its interior.

The working gas inside the TPC is P10 gas (90% Argon + 10% Methane), charged particles traverse the volume liberating electrons from the Argon causing electron avalanches, which drift

[3]https://nsww.org/projects/bnl/star/sub-systems.php

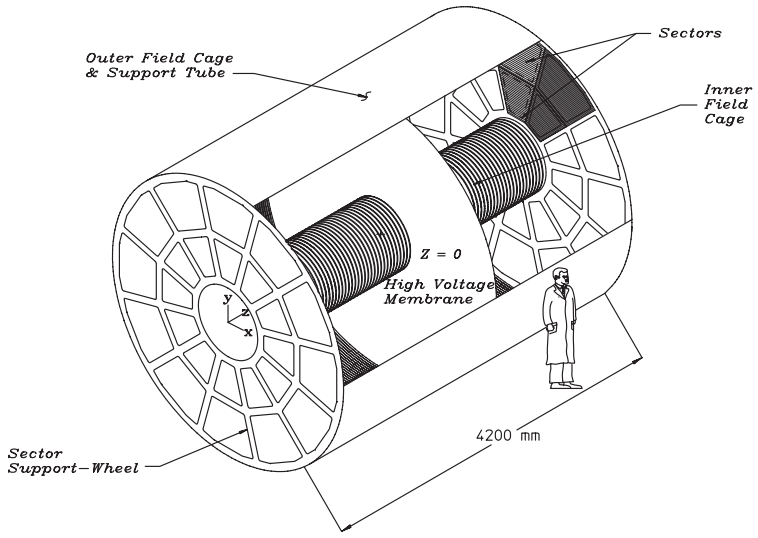

Figure 2.2.3: The STAR TPC surrounds a beam-beam interaction region at the RHIC. Collisions occur near the center of the TPC.

towards the anodes of the TPC with a velocity of $\langle v_e \rangle \sim 5.5$ cm/μs. The lateral diffusion of electrons inside the P10 gas and in the 0.5 T magnetic field is 230 μm/cm (σ_T = 3.3 mm), which sets the scale of the X,Y plane of the filament chamber readout system. Similarly, the longitudinal diffusion of the electron cluster after drifting the entire length of the TPC is σ_L = 5.2 mm. At the drift velocity of 5.5 cm/μs, the longitudinal diffusion width is equivalent to a drift time spread of approximately 230 ns in half-height, which sets the resolution of the longitudinal drift direction of the trace system.

The TPC reconstructs the trajectory of the initial particle by identifying ionized clusters along its path, determining the respective X, Y, and Z space coordinates. It can record particle trajectories, measure their momentum, and identify particles based on their ionization energy loss (dE/dx) within the TPC. The TPC covers the full region of azimuth ($0 < \phi < 2\pi$) and covers the pseudo-rapidity range of $|\eta| < 2$ for inner radius and $|\eta| < 1$ for outer radius.

In the STAR experiment, the Bethe-Bloch equation [4] is utilized to calculate the theoretical energy loss (expressed by Eq. (2.2.1)) that is experienced by a charged particle while passing through the STAR TPC.

$$-\frac{dE}{dx} = Kz^2\frac{Z}{A}\frac{1}{\beta^2}[ln\frac{E_{kin}^{max}}{I} - \beta^2 - \frac{\delta}{2}] \tag{2.2.1}$$

where $K = 4\pi N_A r_e^2 m_e c^2$ is a constant equal to 0.307075 MeV $mol^{-1}cm^2$, z is the charge

number of the incident particle, Z and A represent the atomic number of absorber and atomic mass of absorber, E_{kin}^{max} is the maximum transfer kinetic energy transferred from the incident particle to the stationary electron. I is the average excitation energy, δ is the density effect correction parameter. Fig. 2.2.4 shows the particle identification (PID) capabilities up to date with the TPC. In addition, the TOF PID capability is also shown on the plot which will be discussed in the next section [100].

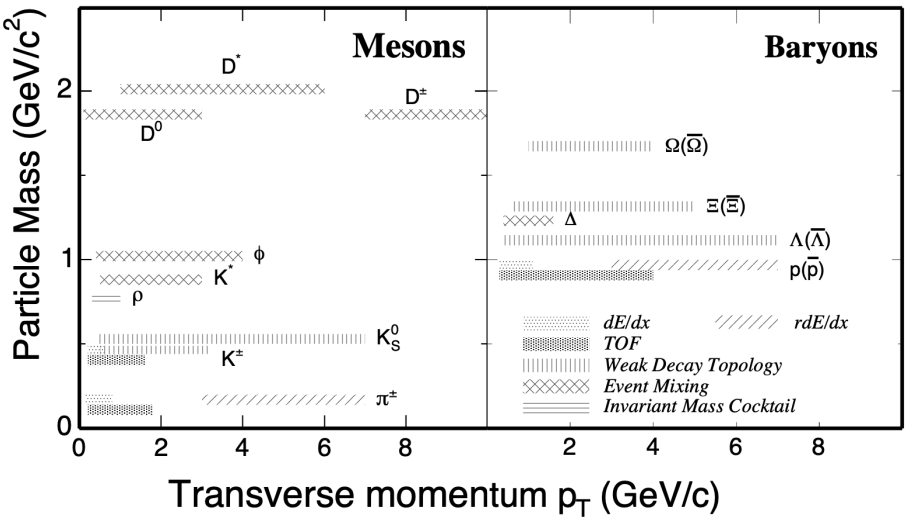

Figure 2.2.4: p_T range of particle identification capability with STAR detectors. Figure taken form [100].

2.2.2 Time of Flight

Comparing the p_T acceptance of dE/dx and TOF in Fig. 2.2.4, it is clear that TOF can give information about particles with higher p_T range.

The barrel Time of Flight (referred to as BTOF or TOF) detector was put into the STAR experiment in 2010 [101, 102]. This detector significantly extends the reach of the STAR scientific program, doubling the percentage of kaons and protons for which particle identification is possible to more than 95% of all those produced within the MRPC-TOF acceptance. Combined with the TPC, it can basically complete the identification of most particles in high-energy experiments. The TOF detector is based on the Multi-gap Resistive Plate Chamber (MRPC) technology and as Fig. 2.2.5 shows, it is mounted in the outer cylinder of the TPC installation.

[4]https://nsww.org/projects/bnl/star/sub-systems.php

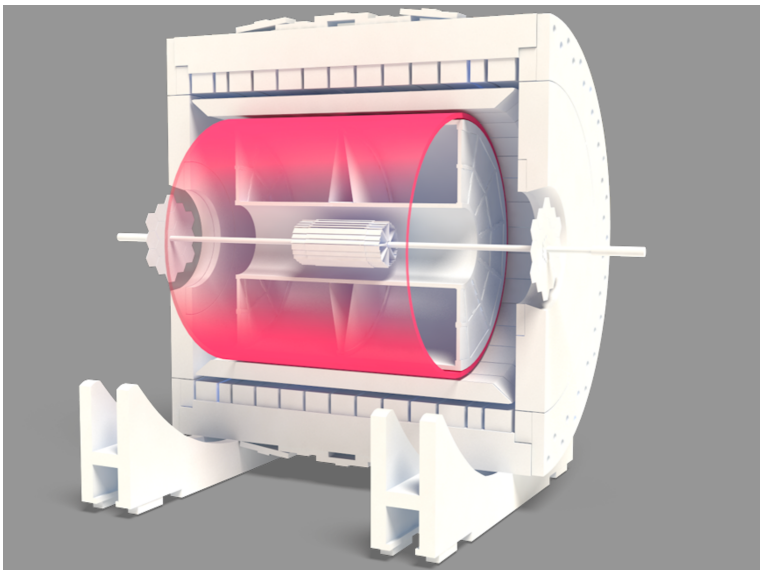

Figure 2.2.5: The Time of Flight detector is a sub-detector of the STAR detector system, shown as the pink cylinder in the figure. It is wrapped around the perimeter of the TPC. [4].

The TOF is composed of a total of 120 trays, with 60 on each east and west side. As shown in the Fig. 2.2.6, each tray contains 32 modules, covering a pseudo-rapidity (η) range from 0 to 1, and providing azimuthal angle coverage across 2π, the intrinsic time resolution is 80 ps.

An MRPC consists of a stack of resistive plates with a series of uniform gas gaps. Figure 2.2.7 shows two side views of an MRPC module appropriate for STAR, where the top panel shows the long edge view and the bottom panel shows the short edge view. Electrodes are applied to the outer surface of the outer plates. A strong electric field is generated in each sub-gap by applying a high voltage across these external electrodes. All the internal plates are electrically floating. A charged particle going through the chamber generates avalanches in the gas gaps. Because the glass plates are resistive, they are transparent to charge induction from avalanches in the gaps. Typical resistivity for the glass plates is on the order of 10^{13} Ω/cm. Thus the induced signal on the pads is the sum of possible avalanches from all gas gaps. The electrodes are made of resistive graphite tape and are also transparent to charge. Copper pickup pads are used to read out the signals. There are six read-out strips on each module in this design. A view of these pads for the present MRPCs is shown in the right of Fig. 2.2.6. The pickup pad layers are separated from the outer electrodes by 0.35 mm of Mylar. In multiple experiments, the use of TOF detectors has demonstrated excellent detection efficiency, exceeding 95%.

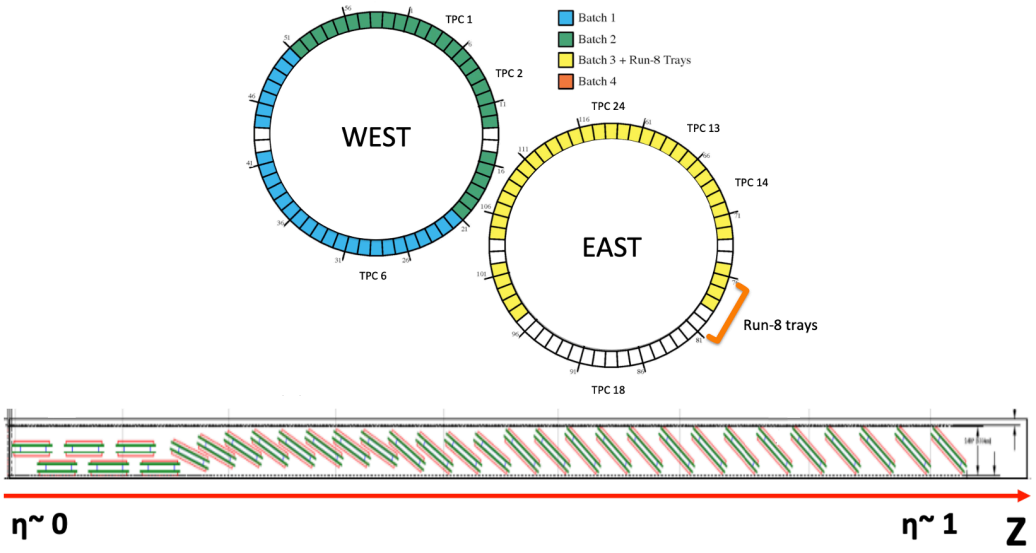

Figure 2.2.6: STAR Barrel TOF trays and tray geometry.

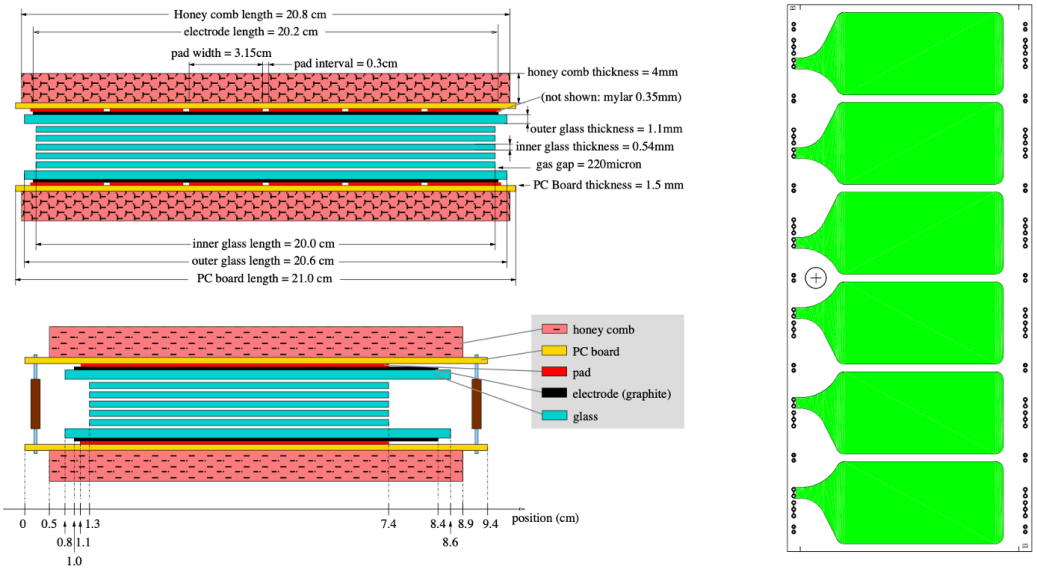

Figure 2.2.7: (left) Two side views of the structure of an MRPC module. (right) The circuit board with the copper read-out pads for the MRPC detectors [102].

Based on the traveled path length (L) and the momentum (p) of the particles measured by TPC detector, combined with the elapsed time (t) measured by TOF, the track flight velocity (β) and the particle mass (m) can be calculated by the equations:

$$\beta = \frac{L}{ct} \tag{2.2.2}$$

$$m^2 = p^2(\frac{1}{\beta} - 1) \tag{2.2.3}$$

2.3 STAR Fixed-Target Experiment

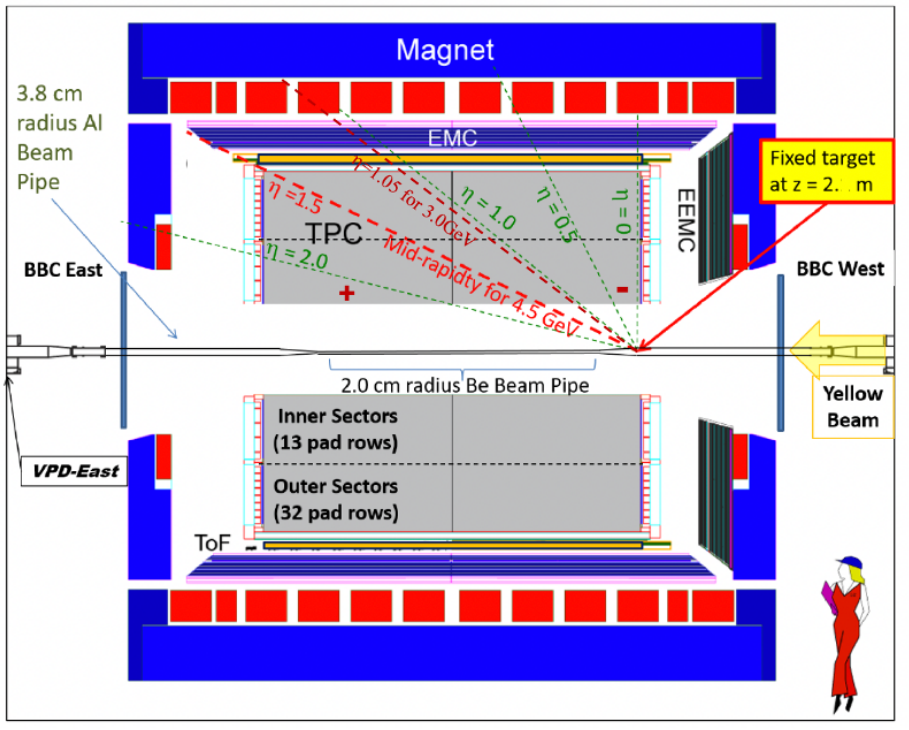

Figure 2.3.1: The setup of fixed-target program of the STAR experiment [103].

This section introduces the Fixed-Target (FXT) program of the STAR experiment [103]. The energy region explored in the STAR first Beam Energy Scan program (BES-I) from a center-of-mass energy of $\sqrt{s_{\rm NN}}$= 7.7 - 200 GeV. At the same time, the physics of the low energy region is extremely important. Unfortunately, it is impractical to use RHIC's "collider mode" to study collisions below 7.7 GeV. Derived from early investigations during the BES program in 2010 and 2011, which involved collisions between gold ions in the beam halo and

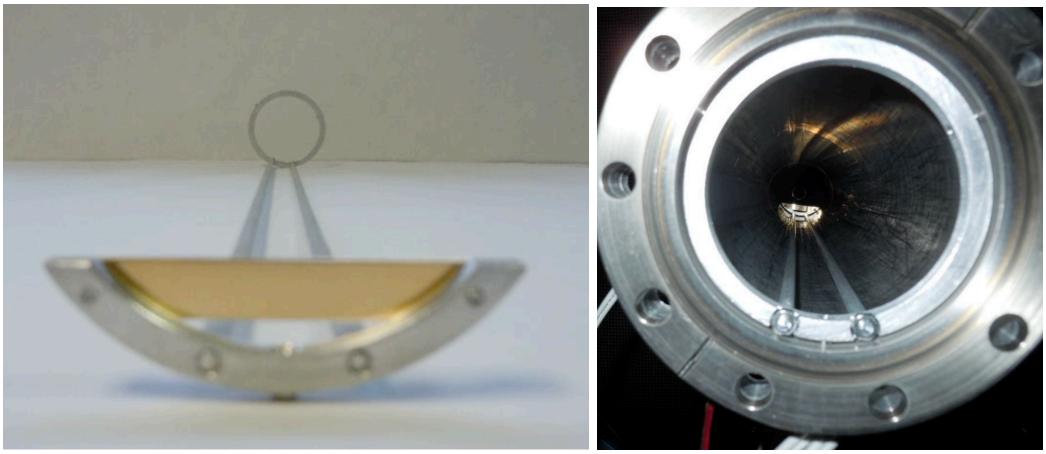

Figure 2.3.2: Left panel: The gold target which is a 0.25 mm-thick foil. Right panel: A view of the gold target installed inside the beam pipe [103].

aluminum nuclei in the beam tube, a fixed target mode employing an internal gold target enabled the study of center-of-mass energies between 3.0 and 7.7 GeV systems are possible.

In 2018, RHIC initiated the second phase of the Beam Energy Scan program (BES-II). Figure 2.3.1 illustrates the schematic of fixed-target setup in the STAR experiment, with the gold target was installed in the vacuum pipe at 200.7 cm to the west of the nominal interaction point and 2 cm down from the central beam-pipe axis of the STAR detector, which has a thickness of 1.93 g/cm^2 (250 μm) corresponding to a 1% interaction probability (see Fig. 2.3.2). An incident beam, comprising 12 bunches of 7×10^9 gold ions, circulated in the RHIC ring at 1 MHz with an energy (approximately 3.85 GeV per nucleon), entered from the right side of the plot and bombarded the target.

Chapter 3

Analysis Details

3.1 Dataset and Event Selection

3.1.1 Dataset

The STAR FXT program [27, 104] was proposed to achieve lower center-of-mass energies and higher baryon density regions. The dataset used in this analysis is obtained from the FXT program of Au+Au collisions at single beam energy is 3.85 GeV, corresponding the center of mass energy $\sqrt{s_{\rm NN}} = 3$ GeV ($y_{mid} = -1.045$) by the STAR experiment.

For FXT collisions, the lab frame and center-of-mass frame are not same, and we take the beam-going direction as the positive direction. Thus, according to the conventions, the rapidity in the center-of-mass can be expressed as:

$$y_{cm} = -\left(y_{lab} - y_{mid}\right), \tag{3.1.1}$$

In the subsequent analysis and text, y_{cm} is directly represented by the simplified y.

3.1.2 Event Selection

The minimum-bias event with Trigger ID == 620052 is selected. The official bad runs can be found in the link: https://drupal.star.bnl.gov/STAR/system/files/Kimelman_3GeV_run_by_run_QA_badRuns.pdf. In this analysis, we removed about 35 million events with the following 24 bad runs are: 19151029, 19151045, 19152001, 19152078, 19153023, 19153032, 19153065, 19154012, 19154013, 19154014, 19154015, 19154016, 19154017, 19154018, 19154019, 19154020, 19154021, 19154022, 19154023, 19154024, 19154026, 19154046, 19154051, 19154056.

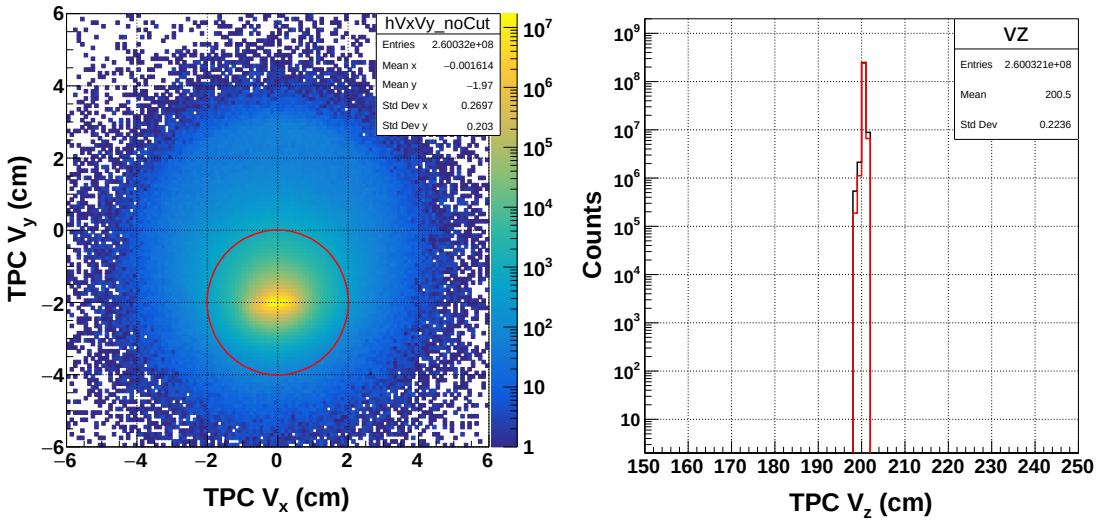

Figure 3.1.1: The V_x *vs.* V_y(left) distribution and V_z(right) distribution in Au+Au collisions at $\sqrt{s_{\rm NN}} = 3$ GeV. The red lines represent the cuts used in this analysis.

Figure 3.1.1 shows vertex distribution and the central vertex of V_x, V_y, V_z is 0, -2, 200 cm, respectively. Thus the event selections of vertex are $V_x^2 + (V_y + 2)^2 < 2^2$ and $198 < V_z < 202$. The experimental data was obtained by about 260 million minimum-biased events that were retained after applying offline event selection criteria with careful quality assurance. The selection of minimum-biased events was realized by simultaneously detecting multiple signals from the Beam-Beam Counter (BBC) [105] and Time of Flight (TOF) [106] detector systems.

3.1.3 Centrality Determination

Apply event cuts, the FXT multiplicity is defined as all primary tracks in single event. Then the collision centralities were determined by Glauber model fitting of the charged-particle multiplicity measured within the pseudo-rapidity range $-2 < \eta < 0$ (FXTMult). The details of official centrality defination done by Zachary Sweger can be found at the link: https://drupal.star.bnl.gov/STAR/system/files/3p0GeV_StandardNewest%20%284%29.pdf. In the analysis, four centrality bins (0-10%, 10-20%, 20-40%, and 40-80%) were used. The FXTMult ranges and the mean values of the number of participating nucleons $\langle N_{\rm Part} \rangle$ for the corresponding centrality bins are shown in Table 3.1.

Table 3.1: Centrality definition and the corresponding mean value of $\langle N_{\rm Part}\rangle$ along with the statistical and systematic uncertainties in Au+Au collisions at $\sqrt{s_{\rm NN}} = 3\,{\rm GeV}$.

Centrality	FXTMult	$\langle N_{\rm Part}\rangle$
$0-10\%$	$195-119$	$310.7 \pm 0.1 \pm 8.3$
$10-20\%$	$118-86$	$224.2 \pm 0.1 \pm 8.0$
$20-40\%$	$85-41$	$135.0 \pm 0.1 \pm 5.3$
$40-80\%$	$40-5$	$39.7 \pm 0.1 \pm 1.9$

3.2 Particle Signal Extraction

3.2.1 Track Quality Cuts

In the analysis, particle identification was done with the Time Projection Chamber (TPC) [99] and the Time of Flight (TOF) [106]. To ensure the track quality, it was required that at least 20 of the maximum 45 possible hits (nHitsFit) in the TPC were used to reconstruct the tracks. To avoid counting the reconstructed tracks of individual particles multiple times, more than 52% of the maximum possible fit points were required. In addition, the number of points (nHitsDedx) used to calculate the energy loss (dE/dx) value was also required to be greater than 10. The distance of the closest approach (DCA) from the reconstructed track to the primary vertex was required to be less than 3 cm for protons and 1 cm for light nuclei, in order to suppress contamination from spallation in the beam pipe. In the TOF measurement, an additional filter was implemented to include the local position of the hit in radial (Y-axis) and beam (Z-axis) directions: $|{\rm btofYLocal}| < 1.8\,{\rm cm}$ and $|{\rm btofZLocal}| < 2.8\,{\rm cm}$.

3.2.2 Particle Identification

Particle identification is done with two types of detectors in this analysis, at low momentum by ionization energy loss (dE/dx) information from the Time Projection Chamber (TPC) and high momentum by m^2 information from the Time of Flight (TOF). Figure 3.2.1 shows the dE/dx versus particle rigidity (p/q) distribution, particle m^2 versus particle rigidity (p/q) distribution, and particle velocity ($1/\beta$) versus rigidity (p/q) distribution, where p is particle momentum, q is particle charge.

As the top figure shows, it is clear from the dE/dx distributions that PID is possible at low momentum using the TPC. To identify the specified particles, the variables $n\sigma_p$ and Z were defined as:

$$n\sigma_p = \frac{1}{\sigma_R} \ln \frac{\langle dE/dx\rangle}{\langle dE/dx\rangle^p_{Bichsel}} \tag{3.2.1}$$

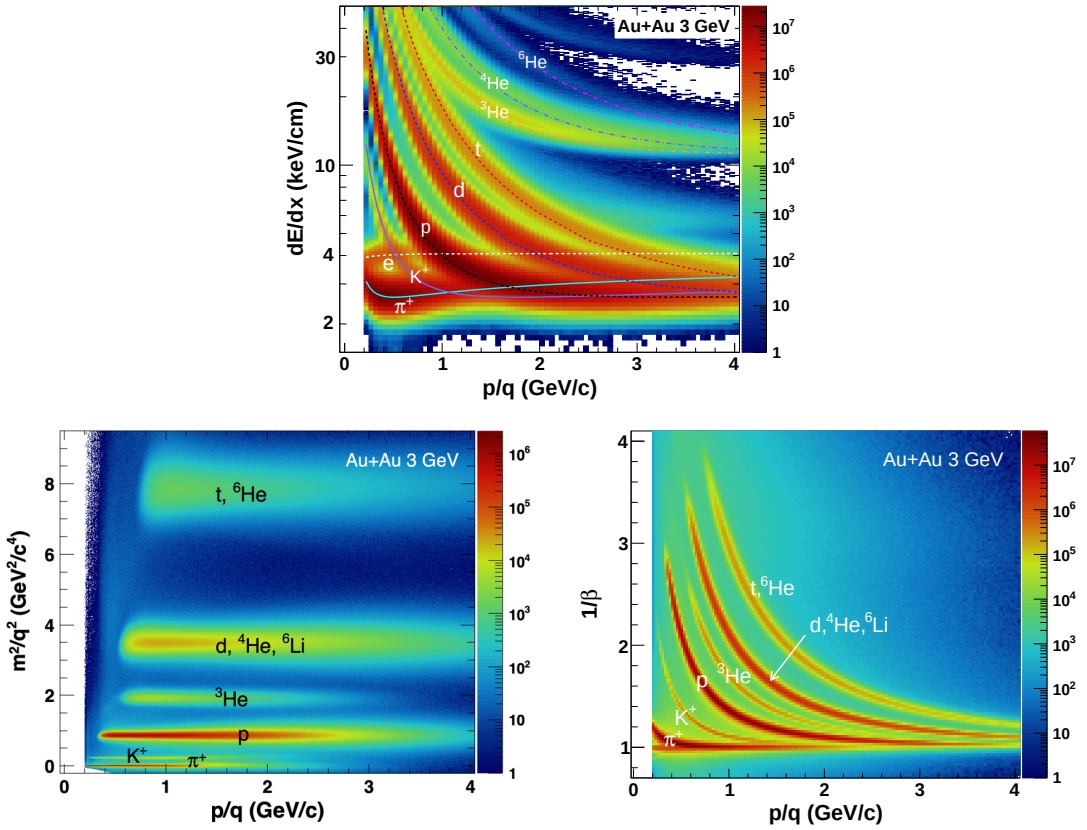

Figure 3.2.1: (top) The dE/dx of charged tracks versus rigidity in Au+Au collisions at $\sqrt{s_{\rm NN}} =$ 3 GeV. The dotted lines are Bichsel theoretical curves for the corresponding particles. (bottom left) The m^2/q^2 of particle versus rigidity distribution. (bottom right) Particle velocity $(1/\beta)$ versus rigidity distribution at same collision energy.

$$Z = \ln \frac{\langle dE/dx \rangle}{\langle dE/dx \rangle_{Bichsel}} \tag{3.2.2}$$

where the $\langle dE/dx \rangle_{Bichsel}$ is the theoretical value of the energy loss obtained from the Bichsel function [107], which was represented by a dashed line in the figure, and σ_R is the TPC $\ln\langle dE/dx \rangle$ resolution ($\sim 8\%$). Finally, the raw signal of protons was obtained by fitting a Gaussian function to the distribution of $n\sigma_p$ with cut $|n\sigma_p| < 3.0$, and the raw signal of light nuclei was obtained by fitting a Gaussian function to the Z-distribution with cut $|Z| < 0.3$.

At high momentum, the dE/dx distribution of different particles with a large overlap, in order to get accurate particle information, the raw signal was extracted by using the mass squared (m^2) distributions from the TOF detector in addition to the $n\sigma_p$ and/or Z information.

The m^2 was calculated as

$$m^2 = p^2\left(\frac{1}{\beta^2} - 1\right) \tag{3.2.3}$$

where p is the momentum of the particle, $\beta = L/ct$, and L, c, t are the track path length, speed of light, and time of flight, respectively. The bottom right of Fig. 3.2.1 shows the particle velocity $(1/\beta)$ versus rigidity (p/q) distribution with very clear bands for all particles. As the bottom left of the figure shows the particle m^2 versus rigidity (p/q). One can observe that there are very clear bands in the m^2 distribution of different particles.

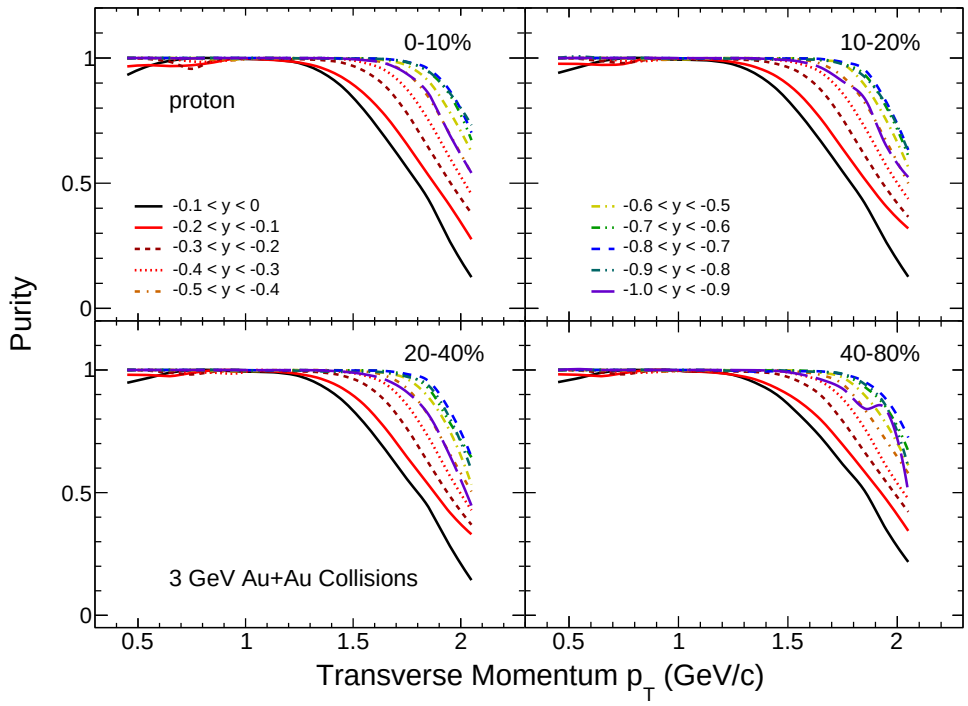

Figure 3.2.2: The purity of proton identified by TPC at $\sqrt{s_{\rm NN}} = 3$ GeV. Different colored lines represent different rapidity slices.

The particle identification is more complicated according to the relationship between TPC resolution and particle rapidity. In order to optimize particle identification, we calculated the purity of of protons, deuterons, and tritons identified by TPC, which was calculated by dividing the number of signals in the corresponding pT range (Gaussian fit) by the total number of signals and backgrounds (Gaussian + exponential fit). Figure 3.2.2 and Fig. 3.2.3 shows the purity of protons, deuterons, and tritons in 0-10%, 10-20%, 20-40%, and 40-80% Au+Au collisions at $\sqrt{s_{\rm NN}} = 3$ GeV. Different colored lines represent different rapidity ranges. It can be seen that purity has no obvious dependence on centrality. Figure 3.2.2 shows the purity of

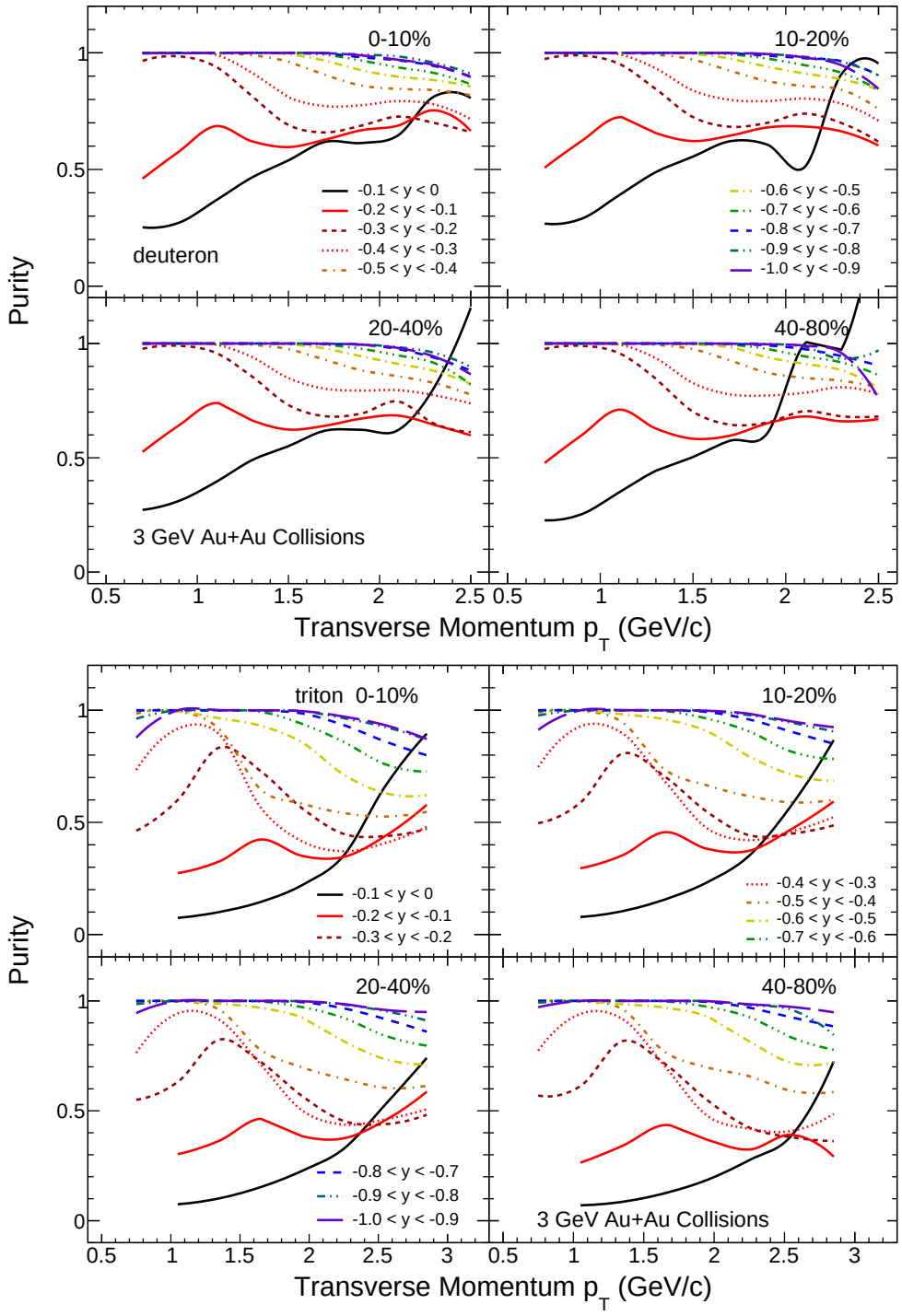

Figure 3.2.3: (top) The purity of deuteron identified by TPC at $\sqrt{s_{\rm NN}}$ = 3 GeV. Different colored lines represent different rapidity slices. (bottom) The purity of triton identified by TPC.

protons. It is obvious that the proton signal given by TPC is ideal in all rapidity windows, so we choose a uniform purity condition (greater than 80%) in all rapidity and centrality ranges, which corresponds to a transverse momentum cutoff is $p_T < 1.5\,\mathrm{GeV/c}$. Figure 3.2.3 shows the purity of deuterons and tritons respectively. Compared with protons, TPC has insufficient ability to identify light nuclei, especially the mid-rapidity range. In order to ensure the quality of particle signals, we choose filtering conditions with a purity greater than 50%. For the rapidity regions that the purity lower than 50%, TOF information is applied for particle identification. The detailed rapidity ranges and transverse momentum (p_T) cutoffs for particle identification using TPC and TOF are listed in the Tab. 3.2.

Table 3.2: The p_T range (in GeV/c) of PID by TPC or TPC+TOF for different particles.

Particle	TPC	TPC+TOF
proton	$p_T \leq 1.5$	$p_T > 1.5$
deuteron($-0.1 < y < 0$)	—	$p_T > 0.6$
deuteron($-1.0 < y < -0.1$)	$p_T \leq 2.6$	$p_T > 2.6$
triton($-0.2 < y < 0$)	—	$p_T > 0.6$
triton($-1.0 < y < -0.2$)	$p_T \leq 3.0$	$p_T > 3.0$
^{3}He	—	$p_T \geq 0.9$
^{4}He	—	$p_T \geq 0.9$

Figure 3.2.4 shows the atomic mass number normalized transverse momentum p_T/A versus center-of-mass rapidity distribution for each particle. The rapidity coverage for the FXT Au+Au collisions at $\sqrt{s_{\mathrm{NN}}} = 3$ GeV is from -1.0 to 0.2. For protons, deuterons, and tritons, the portion identified only via TPC is superimposed on the corresponding panel. Yellow boxes indicate the region for further analysis. The rapidity range measured for each particle in this analysis was -1.0 to 0, divided into 10 uniform rapidity windows with a width of 0.1.

3.2.3 Signal Extraction

To obtain the exact signal of the particles, we fit the signal distribution of the particles using a correspondence function. The final signal values are obtained by integrating the fitted functions. Figure 3.2.5 and Fig. 3.2.6 show the distribution of $n\sigma_p$ for protons, Z for light nuclei, and m^2 for all particles at different p_T bins. The most central collision (0-10%) and $-0.2 < y < -0.1$ rapidity window are as the examples.

At low p_T, as we mentioned above that the particle signal was extracted by TPC, we used a Gaussian function (shown by Eq. (3.2.4)) to fit the $n\sigma_p$ and Z signal distribution (the red lines) and another Gaussian functions to fit the background (the blue and pink lines), then the

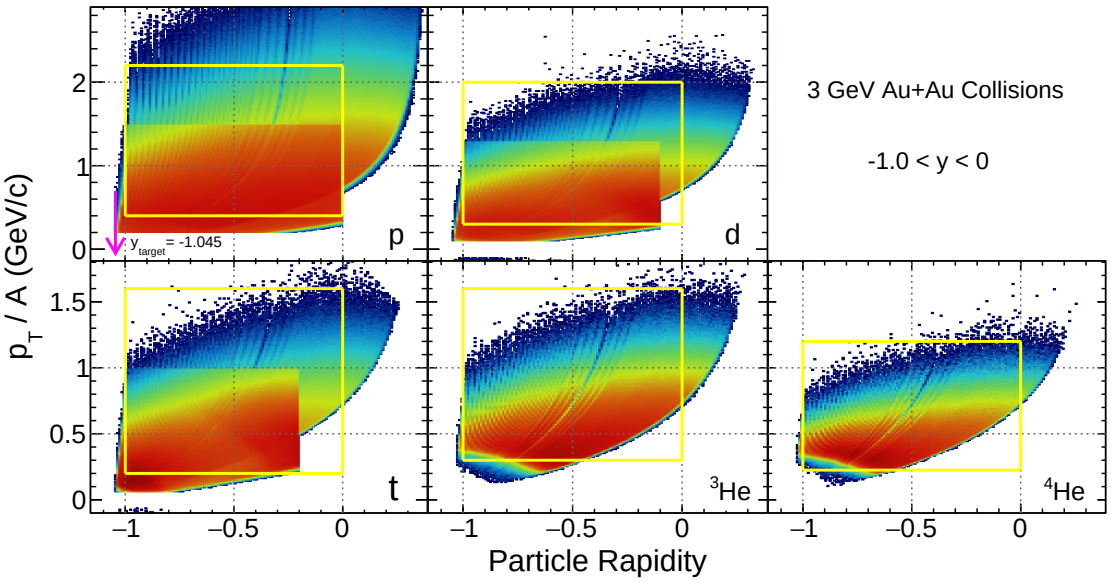

Figure 3.2.4: Atomic mass number normalized transverse momentum (p_T/A) versus rapidity distributions for identified protons, deuterons, tritons, ^{3}He, and ^{4}He. For protons, deuterons, and tritons, the portion identified only by TPC is superimposed. Yellow boxes indicate the region for further analysis.

Gaussian fits were integrated to find the raw yields of the particles.

$$f(x) = p_0 e^{-\frac{1}{2}\left(\frac{x-p_1}{p_2}\right)^2} \tag{3.2.4}$$

where $p_0 = \frac{1}{\sigma\sqrt{2\pi}}$, $p_2 = \sigma^2$, and σ denotes the standard deviation of the Gaussian function. p_1 is the mean value of the distribution.

At high p_T, the m^2 signal distribution (the red lines) can be fitted well by the student-t function as expressed with Eq. (3.2.5), and the background (the blue lines) of the m^2 distribution is fitted by a exponentional function, then the student-t fits were integrated to obtain the raw yields.

$$f(T \mid p_1) = \frac{\Gamma\left(\frac{p_1+1}{2}\right)}{\sqrt{p_1\pi}\Gamma\left(\frac{p_1}{2}\right)}\left(1+\frac{T^2}{p_1}\right)^{-\frac{p_1+1}{2}} \tag{3.2.5}$$

where p_1 is the degree of freedom of the distribution. $T = \frac{x-p_2}{p_3}$ denotes the cumulative probability value of the fit, i.e., the confidence level. $\Gamma()$ is the Gamma function and can be expressed as follows:

$$\Gamma(z) = \int_0^\infty t^{z-1}e^{-t}dt \tag{3.2.6}$$

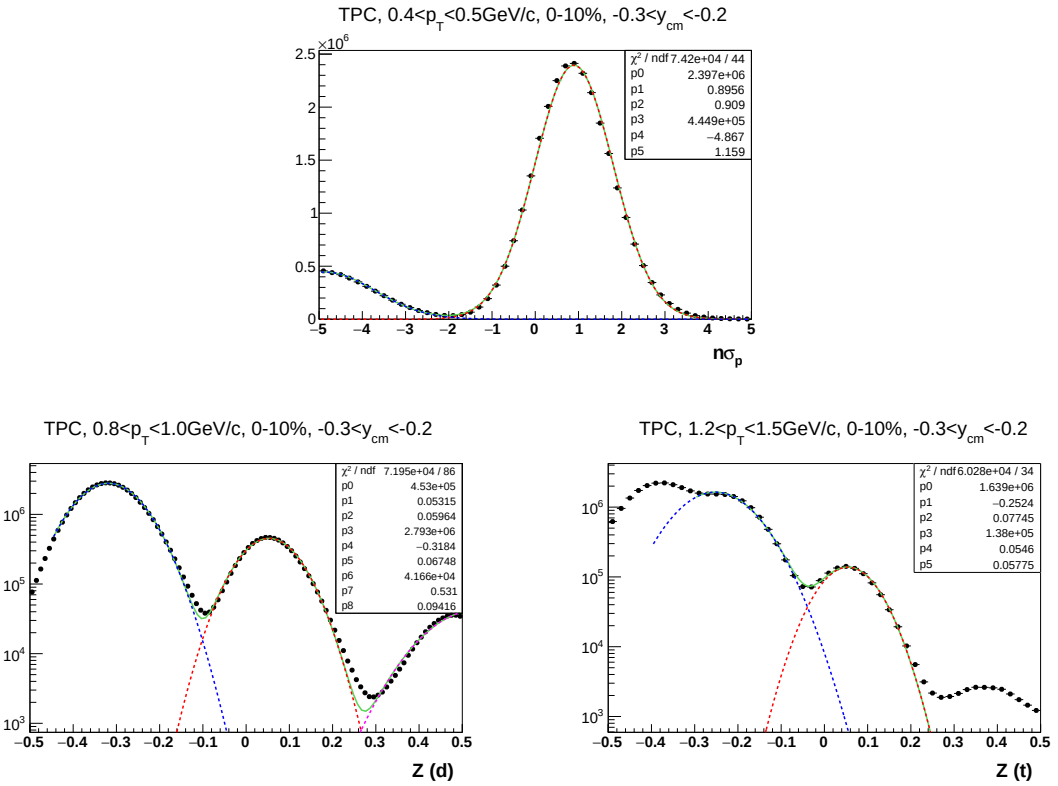

Figure 3.2.5: $n\sigma_p$ and Z distribution in the first p_T bin of particles at $-0.2 < y < -0.1$ rapidity range in 0-10% Au+Au collisions at $\sqrt{s_{\rm NN}} = 3$ GeV. The red lines indicate the signal fits by the Gaussian function. The blue and pink lines indicate the background fits also by the Gaussian function. The green lines represent the result of the simultaneous fitting of signal and background.

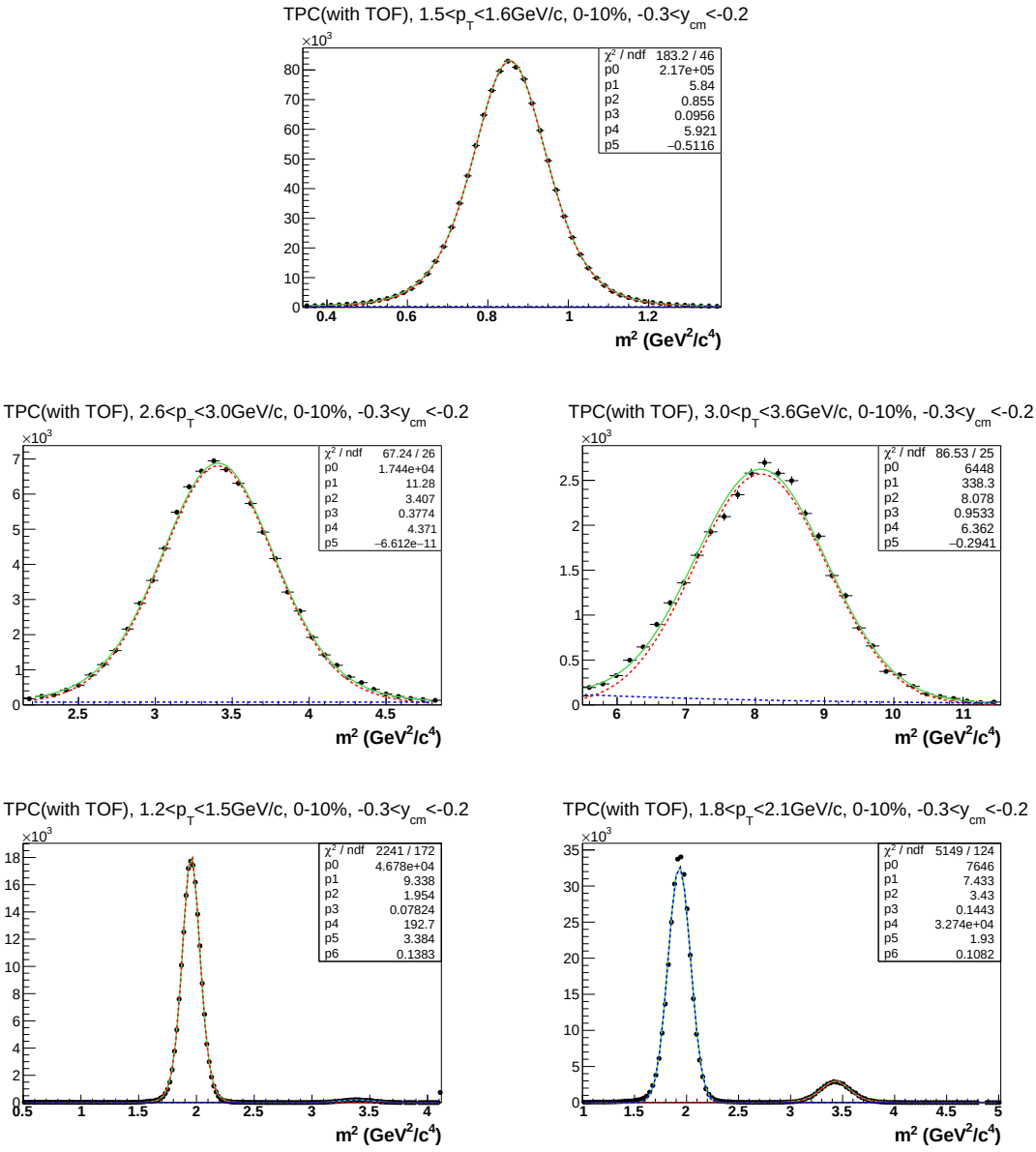

Figure 3.2.6: m^2 distribution in the first p_T bin of particles at $-0.2 < y < -0.1$ rapidity range in 0-10% Au+Au collisions at $\sqrt{s_{\rm NN}} = 3$ GeV. The red lines indicate the signal fits by the student-t function. The blue lines indicate the background fits by the exponential function. The green lines represent the result of the simultaneous fitting of signal and background.

where z is a plural number. In the real number domain, the definition of the Gamma function is restricted to the positive real numbers.

Appendix B shows more signal distributions at other rapidities and centralities. The signal distribution for all measured rapidity and centrality bins can be found in the STAR paper note about protons and light nuclei production [108].

3.3 Efficiency Correction

In order to obtain final particle spectra in each rapidity interval, efficiency correction needed to be done. In general, TPC tracking efficiency, TOF matching efficiency, energy loss correction, absorption correction, and beampipe correction are all required. While for the 3 GeV datasets, we corrected the raw spectrum with TPC tracking efficiency, TOF matching efficiency and energy loss correction. For the absorption correction, due to the lack of antiparticles at low energies, the correction parameter based on the ratio of antiparticles to particles at higher energies does not apply to this energy, so this correction is not taken into account.

3.3.1 TPC Tracking Efficiency

The TPC tracking efficiency and acceptance were determined by the so-called embedding technique. The technique is to embed sampled Monte Carlo (MC) tracks, within a given kinematic range, simulated using a GEANT model [109, 110] of the STAR detector and detector response simulators, into real events at the raw data level to determine the quality and quantity of the reconstructed embedded tracks. The acceptance and reconstruction efficiency is finally given by the ratio of reconstructed tracks to embedded MC tracks, as shown by Eq. (3.3.1):

$$\varepsilon_{\mathrm{TPC}} = \frac{N_{\mathrm{rec.}}(\text{Track quality cuts})}{N_{\mathrm{emb.}}} \tag{3.3.1}$$

where $N_{\mathrm{rec.}}$ and $N_{\mathrm{emb.}}$ are the number of reconstructed MC tracks satisfying the track quality cuts and the number of embedded MC tracks, respectively.

The embedding data we used are https://drupal.star.bnl.gov/STAR/starsimrequests/2020/jul/10/fxt-auau-30-gev-2018-pi-k-p for proton,https://drupal.star.bnl.gov/STAR/starsimrequests/2020/jul/10/fxt-auau-30-gev-2018-p-d-t-3he and https://drupal.star.bnl.gov/STAR/node/54208 for light nuclei. Figure 3.3.1 shows the p_T dependence of the TPC efficiency in most central (0-10%) Au+Au collisions $\sqrt{s_{\mathrm{NN}}} = 3$ GeV, there are only three rapidity windows ($-0.1 < y < 0$, $-0.5 < y < -0.4$, and $-1.0 < y < -0.9$) for deuterons as example. The final value of TPC tracking efficiency is obtained by fitting with Eq. (3.3.2), as

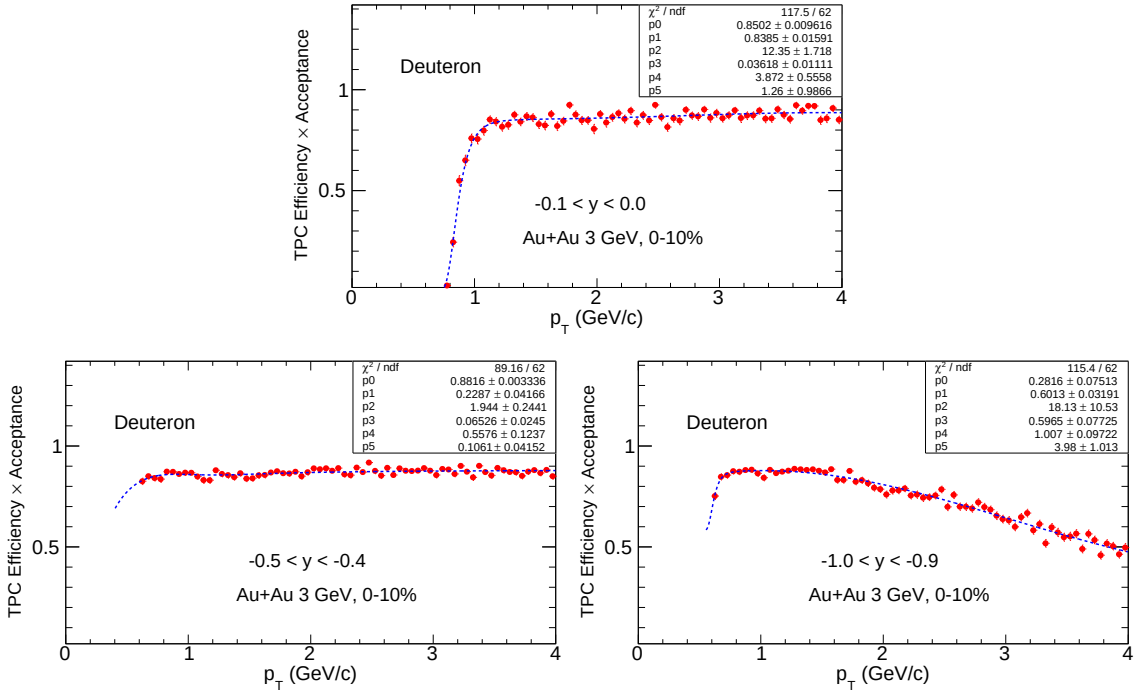

Figure 3.3.1: The TPC tracking efficiency for deuteron in 0-10% Au+Au collisions at $\sqrt{s_{\rm NN}} =$ 3 GeV. Here show the efficiency at rapidity windows with $-0.1 < y < 0$, $-0.5 < y < -0.4$, and $-1.0 < y < -0.9$, respectively. The dashed lines are fitted by the function shown in the text.

shown by the blue dotted line in the figure.

$$\varepsilon_{\rm TPC}\left(p_T\right) = p_0 \times e^{-\left(\frac{p_1}{p_T}\right)^{p_2}} + p_3 \times e^{-\frac{(p_T - p_4)^2}{2p_5}} \tag{3.3.2}$$

The TPC tracking efficiency at mid-rapidity ($-0.1 < y < 0$) for all particles (same result for the deuteron) without strong centrality dependence as shown in the Fig. 3.3.2. Figure 3.3.3 shows the TPC tracking efficiency for p, t,^{3}He, and ^{4}He in 0-10% centrality (same result for the deuteron), different colored markers represent the results at different rapidity windows. In contrast to the weak centrality dependence, a significant dependence on rapidity was observed for each particle. At low p_T, all efficiencies demonstrated an increasing trend with increasing p_T. Conversely, at high p_T, the efficiency at mid-rapidity stabilized to a constant value as p_T increased. However, in proximity to the target rapidity, the efficiencies exhibited a trend of decreasing with increasing p_T.

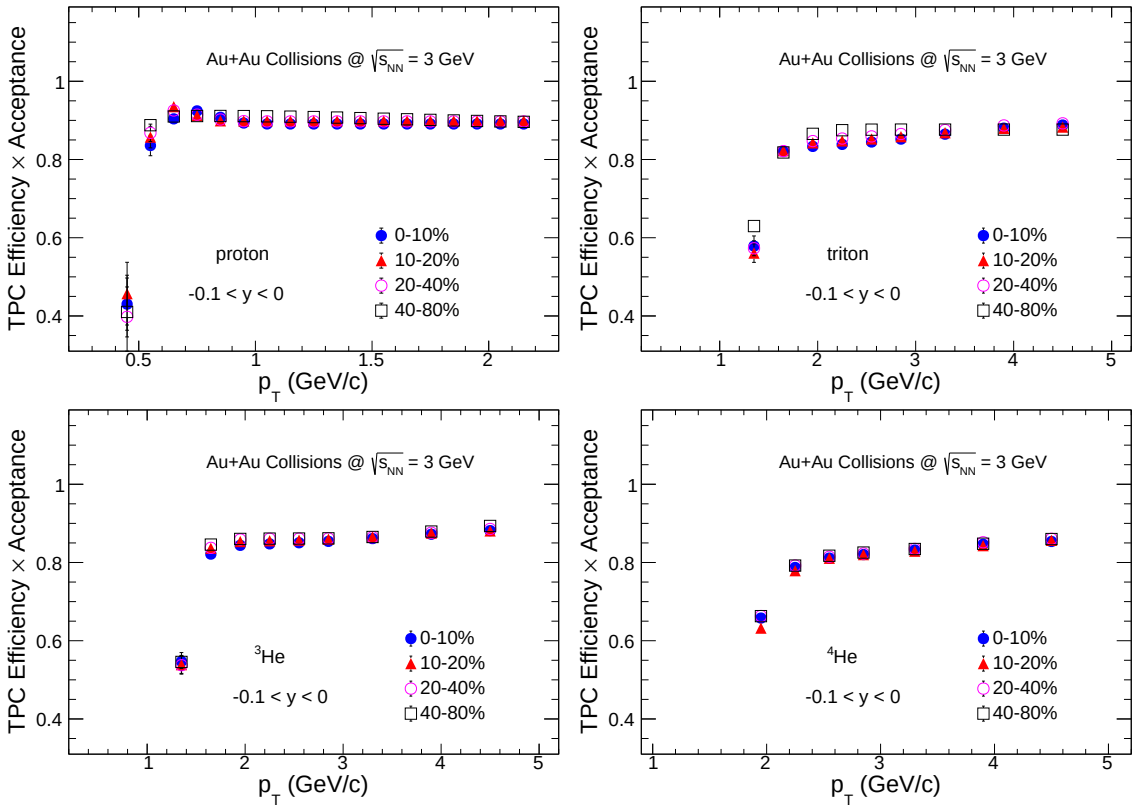

Figure 3.3.2: The TPC tracking efficiency for particles at mid-rapidity in Au+Au collisions at $\sqrt{s_{\rm NN}} = 3$ GeV. The vertical line indicates the function fit uncertainty.

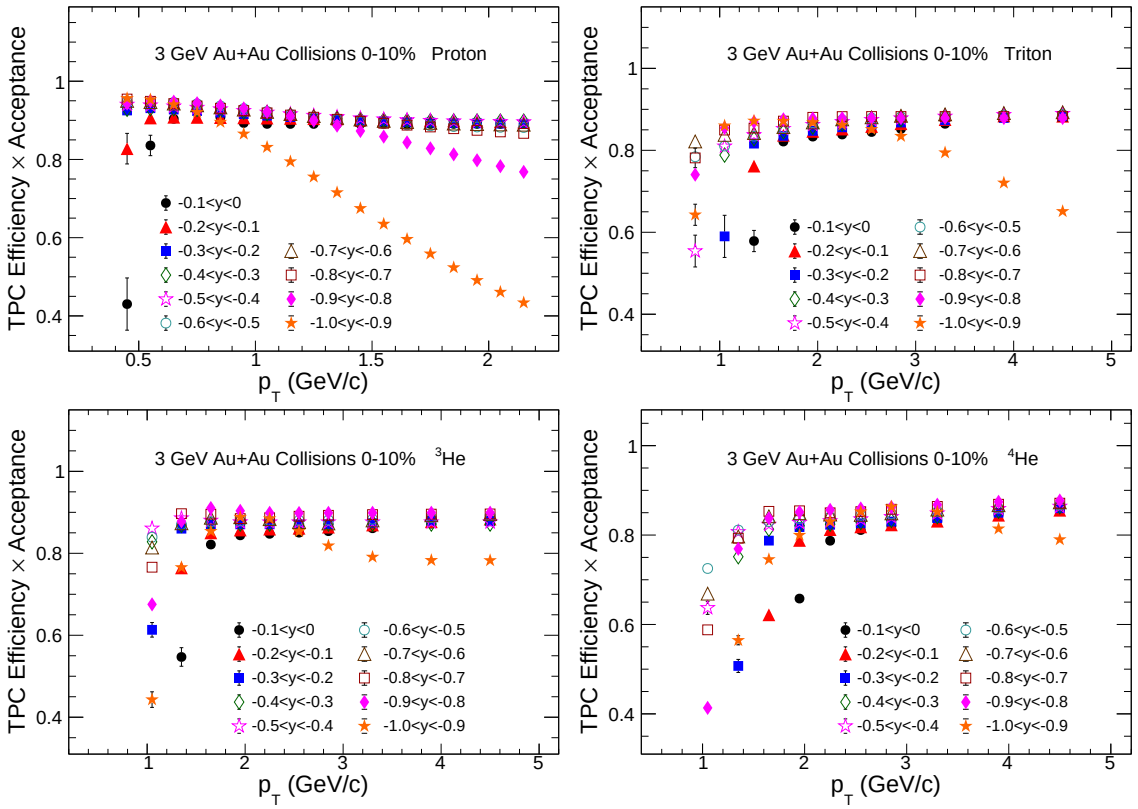

Figure 3.3.3: The TPC tracking efficiency for particles in 0-10% Au+Au collisions at $\sqrt{s_{\rm NN}}$ = 3 GeV. The vertical line indicates the function fit uncertainty.

3.3.2 TOF Matching Efficiency

For proton, deuteron, and triton, we can get the particle signal clearly at low p_T by TPC, while as p_T increases, particles cannot be distinguished by TPC, and it is necessary to obtain the particle information by TOF. For the ^{3}He and ^{4}He analysis, we use the TPC and TOF for all p_T space. Based on the cylindrical structure of the STAR detector, the TOF is located at the periphery of the TPC and has a different acceptance from the TPC. The primary algorithm for recording tracks on the TOF consists of matching points measured on the TOF to TPC (global) tracks. If multiple tracks in the TPC appear on a single read pad of the TOF at the same time, those tracks are not recorded as measured by the TOF. When a track corresponds to multiple hit points in the TOF, the closest hit point is selected. Therefore it is necessary to calculate the correction efficiency of the TOF. The TOF matching efficiency is defined as the ratio between the number of tracks matched with TOF and the number of tracks identified by

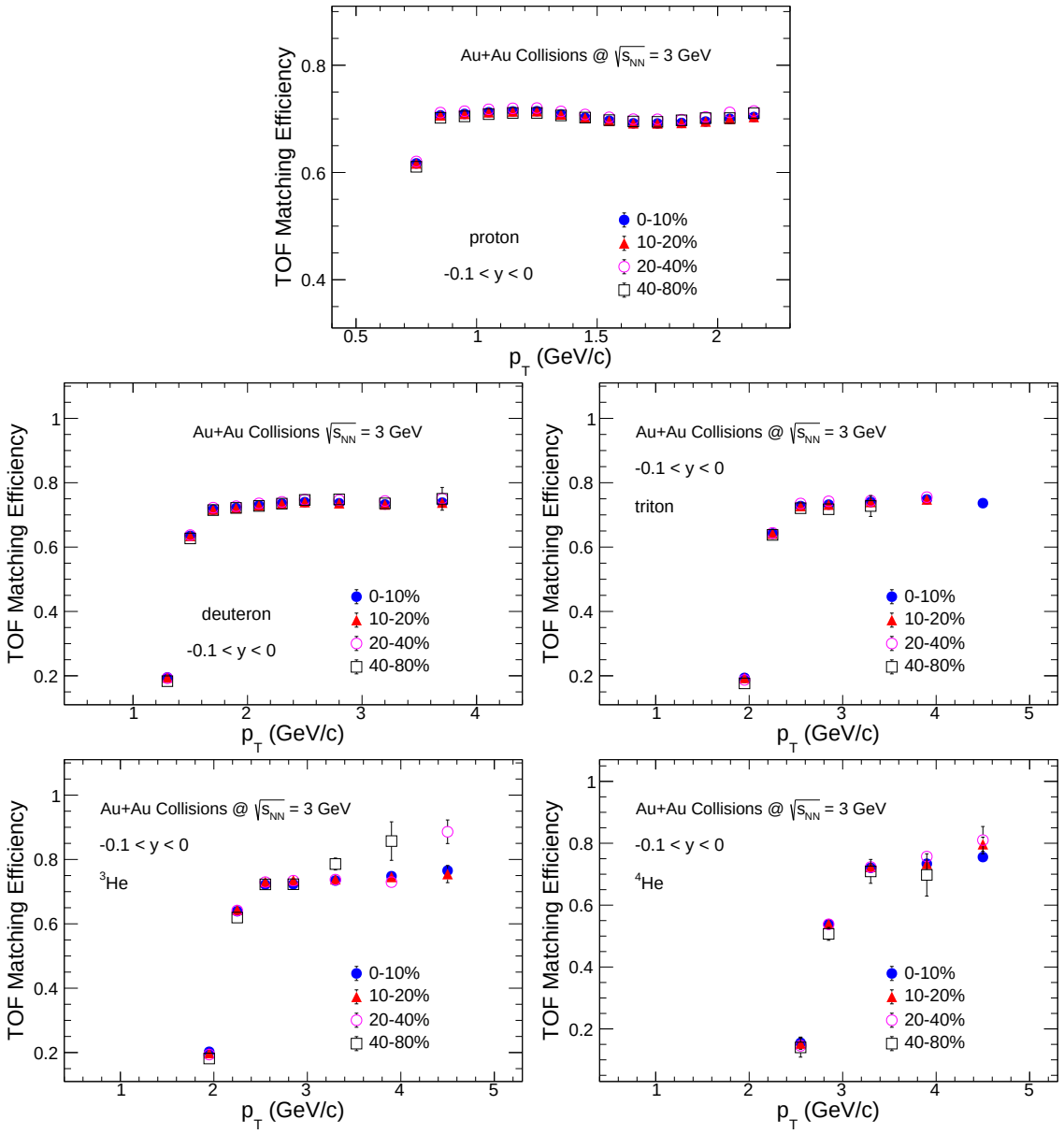

Figure 3.3.4: The TOF matching efficiency of particles at mid-rapidity in Au+Au collisions at $\sqrt{s_{\rm NN}} = 3$ GeV. The vertical line indicates the uncertainty of efficiency, which is calculated by changing the range of $|Z|$ in the identification of TPC particles.

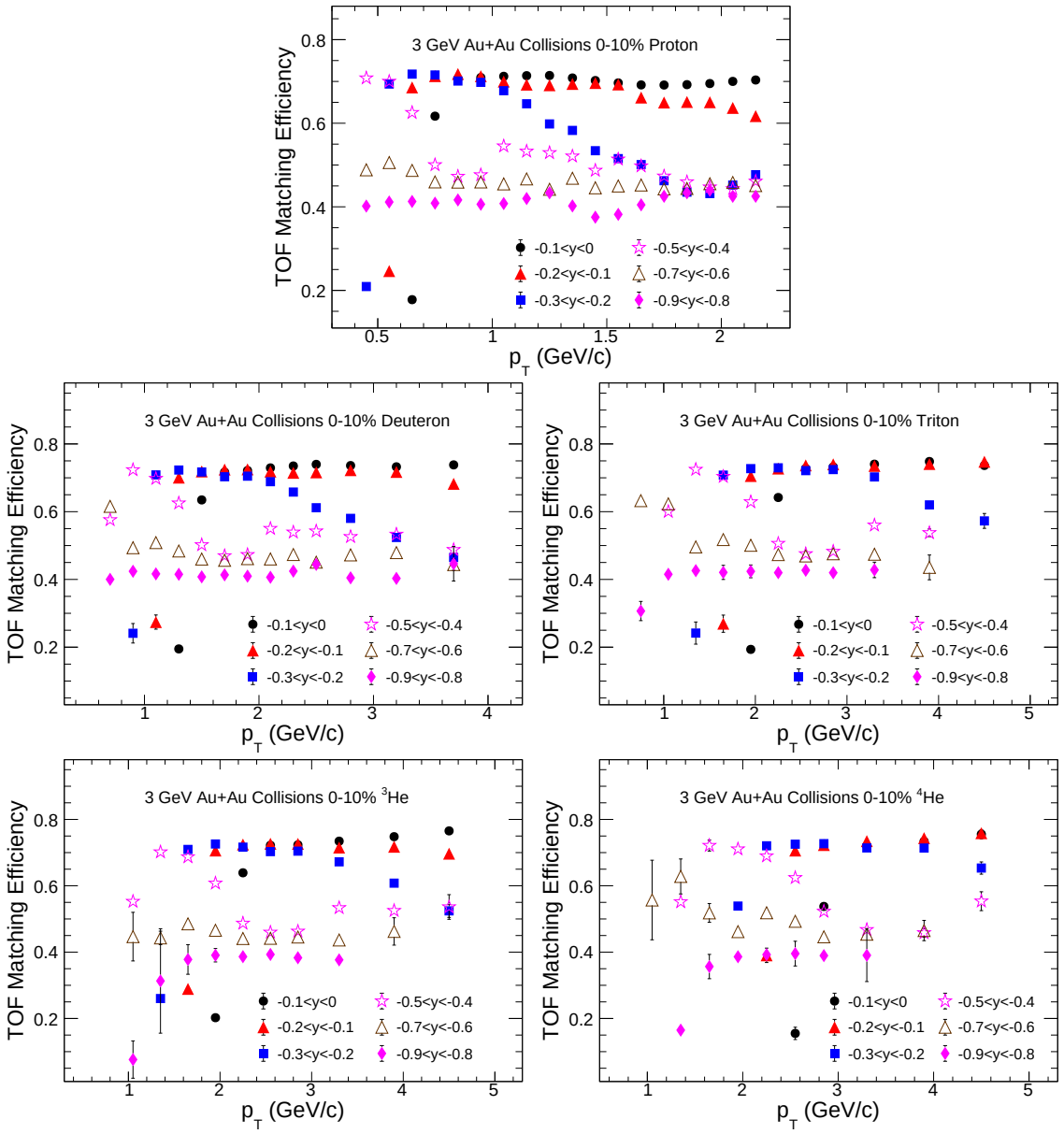

Figure 3.3.5: The TOF matching efficiency of particles in 0-10% Au+Au collisions at $\sqrt{s_{\rm NN}} =$ 3 GeV. The vertical line indicates the uncertainty of efficiency, which is calculated by changing the range of $|Z|$ in the identification of TPC particles.

TPC, as shown by the Eq. (3.3.3):

$$\varepsilon_{\mathrm{TOF}} = \frac{\text{the number of TOF matched tracks}}{\text{the number of TPC tracks}} \tag{3.3.3}$$

The TOF matching efficiency is realized by a data-driven technique and applied to point-by-point spectral correction. As mentioned above, by calculating the ratio of TOF to TPC, the p_T-dependent efficiency under the corresponding truncation condition is obtained. Figure 3.3.4 shows the TOF matching efficiency at mid-rapidity ($-0.1 < y < 0$) for particles, different colored markers represent different centrality collisions, the results have no obvious dependence on centrality.

Figure 3.3.5 illustrates the TOF matching efficiency for particles in 0-10% centrality collisions, different colored markers represent the results at various rapidity windows. This efficiency demonstrates a strong rapidity dependence, shows completely different p_T trends from mid-rapidity to target rapidity. At mid-rapidity, the efficiency for each particle increases with increasing p_T, and stabilizes to a maximum value at high p_T. At semi-middle rapidity, the efficiency at high p_T decreases with increasing p_T. At target rapidity, the overall efficiency trend mirrors that of mid-rapidity, but its maximum value aligns with the minimum value of the semi-middle rapidity.

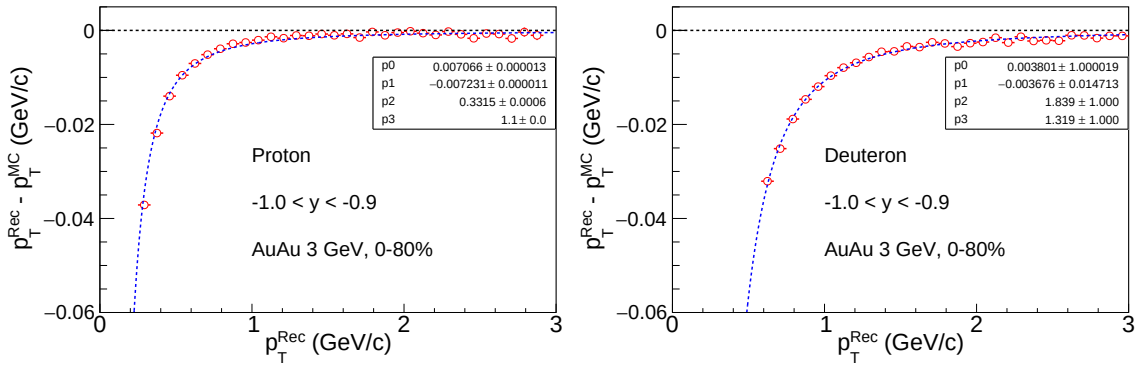

Figure 3.3.6: The energy loss distribution for proton and deuteron in Au+Au collisions at $\sqrt{s_{\mathrm{NN}}} = 3$ GeV.

3.3.3 Energy Loss Correction

Low-momentum particles experience a substantial energy loss while traversing the detector material. Thus, it is necessary to correct the energy loss of these particles, especially the heavier ones. The energy loss can be corrected with the embedding data by comparing the

p_T difference between the reconstructed (p_T^{Rec}) and embedded MC tracks (p_T^{MC}). The p_T-dependent correction factor was parametrized with Eq. (3.3.4).

$$p_T^{Rec.} - p_T^{MC} = p_0 + p_1 \left(1 + \frac{p_2}{(p_T^{rec.})^2}\right)^{p_3} \tag{3.3.4}$$

where p_0, p_1, p_2, and p_3 are the fit parameters. For each particle, a set of fit parameters was obtained to estimated the p_T-dependent energy loss effect. These parameters were utilized to correct the final particle p_T when accounting for these efficiencies.

Figure 3.3.6 shows the difference between reconstructed particle p_T^{Rec} and p_T^{MC} from embedding sample at target rapidity in 3 GeV Au+Au collisions. The distributions was parameterized (blue dashed line) by the function defined in Eq. (3.3.4). For proton and deuteron, we applied energy loss correction at $-1.0 < y < -0.6$ and $-1.0 < y < -0.3$ respectively after we check the value of p_T^{Rec} - p_T^{MC}.

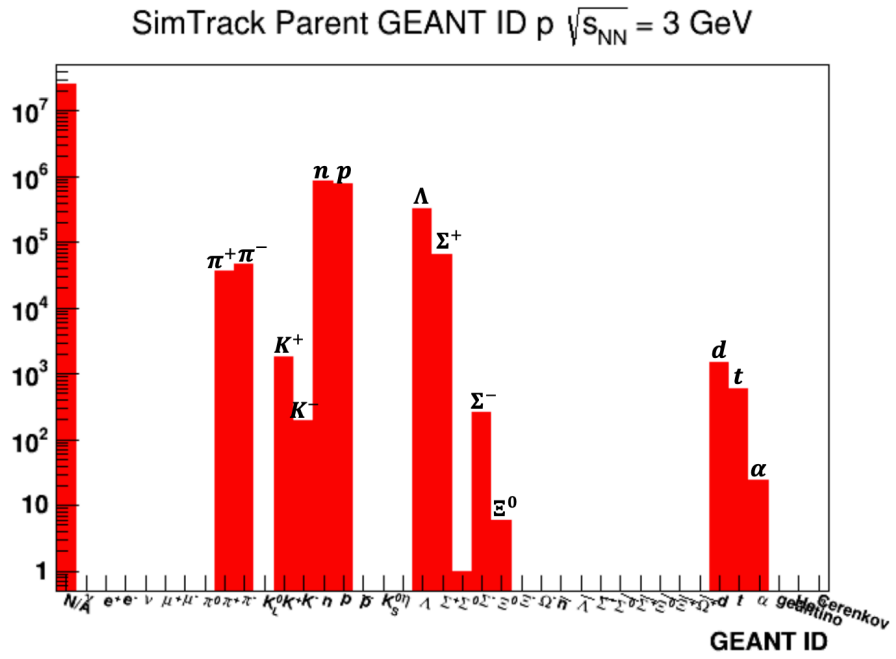

Figure 3.3.7: Simulated parent ID for protons reconstructed from UrQMD events run through a full GEANT simulation of the STAR detector.

3.3.4 Particle Background Correction

A potential source of background contamination in the spectra and yield analysis are knockout-particles produced through interactions of high-energy particles with detectors materials or the beam pipe. We completed a full GEANT simulation of the STAR detector with 1 million UrQMD Au+Au events at $\sqrt{s_{\rm NN}} = 3\,\text{GeV}$, the parent IDs of protons from this UrQMD sample can be seen in Fig. 3.3.7. In order to correct for knockout protons, in each centrality bin and for each pT and rapidity bin, a ratio is constructed where the numerator is the number of protons from knockout sources (pions, kaons, nucleons, and light nuclei) and the denominator is the number of protons from knockout sources and protons from the collision is constructed. We found that knockout-particles constitute less that 2% of the background contamination in the measured acceptance region. Therefore, no knockout correction was applied.

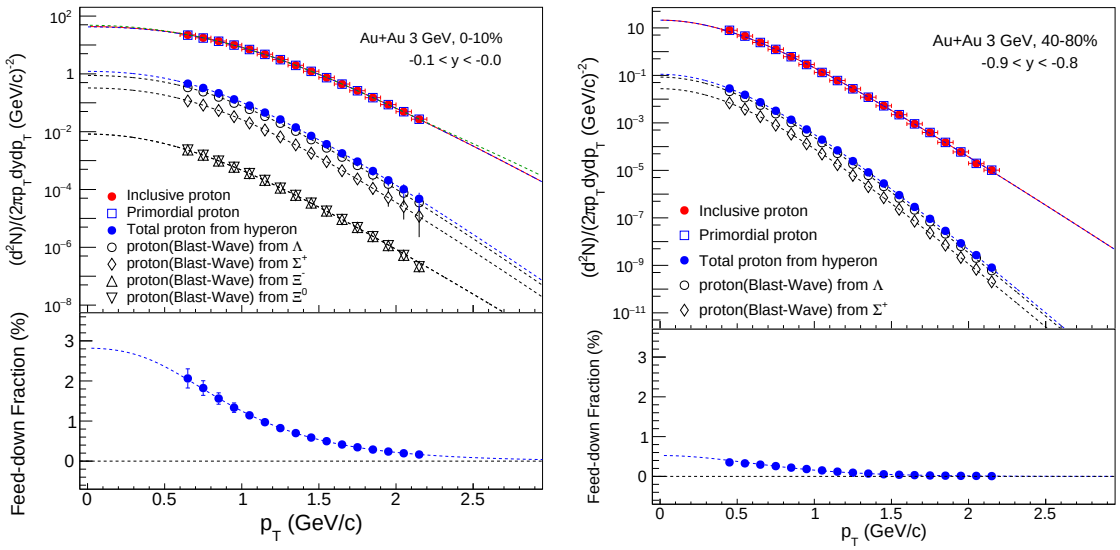

Figure 3.3.8: The p_T dependence of the inclusive, primordial, and week-decay feed-down fraction of proton yields in Au+Au collisions at $\sqrt{s_{\rm NN}} = 3$ GeV.

3.3.5 Weak-decay Feed-down Correction for Protons

In heavy-ion collisions, weak decays of strange baryons, such as Λ and Ξ and their anti-particles, will contribute to the final yields of the (anti-)protons [111–113]. To obtain the primordial yields of (anti-)protons, it is necessary to subtract the contributions from weak decay. As reported in Ref. [62], the STAR experiment has published the energy dependence of the weak decay fractions for (anti-)protons in Au+Au collisions at $\sqrt{s_{\rm NN}} = 7.7 - 200\,\text{GeV}$.

Similarly to the previous analysis, for 3 GeV the measured p_T spectra of Λ and Ξ^- [114] were used as inputs for the embedding to simulate the decay kinematics of hyperons and p_T spectra of the daughter protons. The main decay channels and branching ratios (BR) are shown below [4]:

$$\Lambda \longrightarrow p + \pi^-, \mathrm{BR} = 63.9\%$$

$$\Sigma^+ \longrightarrow p + \pi^0, \mathrm{BR} = 51.57\%$$

$$\Xi^- \longrightarrow \Lambda + \pi^-, \mathrm{BR} = 99.887\%$$

$$\Xi^0 \longrightarrow \Lambda + \pi^0, \mathrm{BR} = 99.524\%$$

The p_T spectra of Σ^+ were obtained by multiplying the Λ spectra by a factor of 0.224 (Σ^+/Λ = 0.224 was estimated from the thermal model). Based on the ART [115] calculation, we assumed the spectra of Ξ^0 and Ξ^- are the same and took 30% of the Ξ^0 yield into the estimate of uncertainty.

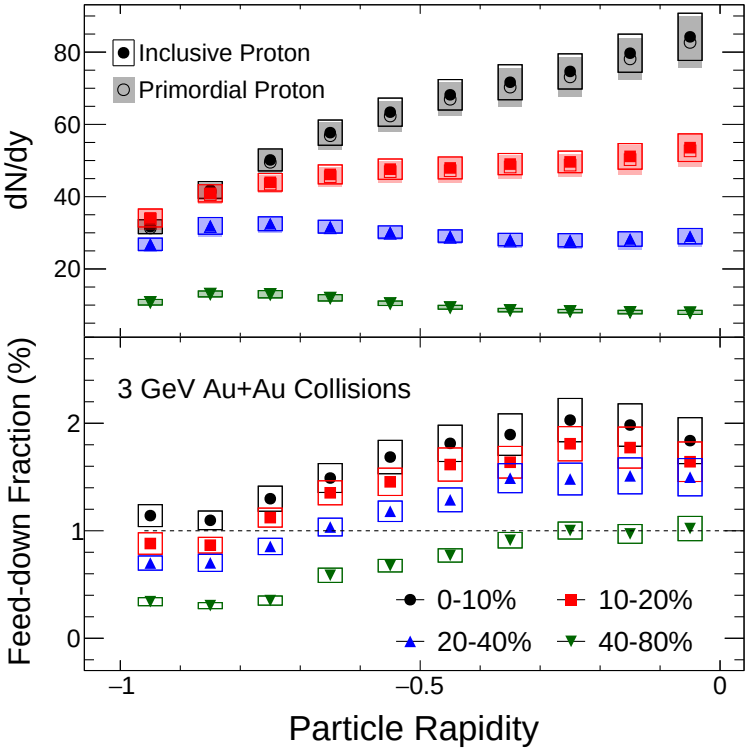

Figure 3.3.9: The rapidity dependence of the inclusive, primordial, and week-decay feed-down fraction of proton yields in Au+Au collisions at $\sqrt{s_{\mathrm{NN}}}$ = 3 GeV.

At this low energy collisions, the yield of the strange baryons is much lower than that of protons. As seen in Fig. 3.3.8, we show the most central collisions (0-10%) at mid-rapidity ($-0.1 < y < 0$) and the peripheral collisions (40-80%) at target rapidity ($-0.9 < y < -0.8$) feed-down informations. The top panel includes the p_T spectra of the inclusive protons, the protons from the weak-decay of strange baryons, and the primordial protons in Au+Au collisions at $\sqrt{s_{\rm NN}} = 3$ GeV. The bottom panel shows the p_T dependence of the fraction from feed-down contribution. Due to the lack of Ξ^- measurements at target rapidity, at $-0.9 < y < -0.8$, we only considered the weak-decay contribution from Λ and Σ^+. By the same method, we calculate the fractions in each centrality bin and rapidity window (See note [108]).

Finally, the obtained weak decay feed-down fractions of protons for each centrality and rapidity window were shown on Fig. 3.3.9, here the top panel shows the dN/dy of inclusive proton and primordial proton, and the bottom panel shows the rapidity dependence of feed-down fraction. The final calculations show that the maximum contribution for the yield of protons from the (Λ, Σ^+, Ξ^-, and Ξ^0) weak-decay feed-down is about 2%.

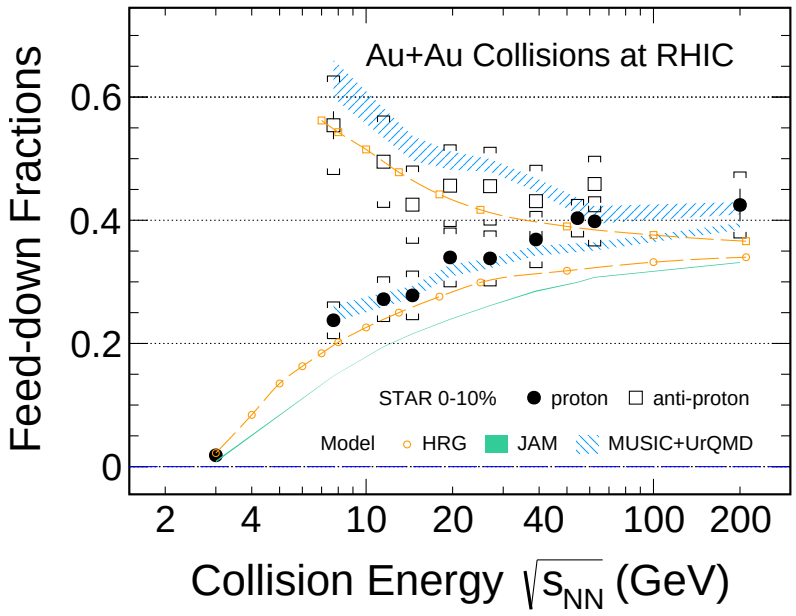

Figure 3.3.10: Energy dependence of the weak decay feed-down fraction of protons (filled circle) and anti-protons (open squares) in 0-10% Au+Au collisions at RHIC. Those results are based on the data driven approach. The calculations from HRG (orange marker), JAM (dark-green band) and MUSIC+UrQMD (dashed-blue area) models are plotted for comparison.

Figure 3.3.10 shows the energy dependence of the weak decay feed-down fraction for protons and anti-protons at mid-rapidity and in 0-10% central Au+Au collisions. The filled circles

and open squares are the results of protons and anti-protons, respectively. While the weak decayed proton fractions decrease as collision energy decreases, the fractions of anti-protons show an opposite increasing trend. At high energies, both fractions get close to each other and reach saturation around ∼40%. The weak decay fraction of (anti-)protons calculated from Hadron-resonance Gas (HRG) and MUSIC+UrQMD models show good agreement with the measured data while the JAM model underestimates the feed-down fractions with respect to our results.

3.4 Systematic Uncertainty

3.4.1 Systematic Uncertainty on p_T Spectra

There are two dominant sources of systematic uncertainties for the p_T spectra. The first one comes from the variation of the track quality cuts, such as nHitsFit, nHitsDedx, and DCA. At Sec. 3.2.1 we gave the default cuts, the systematic uncertainty is estimate by the following cuts (nHits: 20 to 15 and 25; ndE/dx: 10 to 8 and 12; DCA: 1.0 to 0.8 and 1.2 for light nuclei, 3.0 to 2.4 and 2.6 for proton). The total systematic uncertainty from the track quality cuts is obtained by the orthogonal combination with Eq. (3.4.1)

$$RMS = \sqrt{\frac{1}{N}\sum_{i=1}^{N}\left(\frac{X_i - Y}{Y}\right)^2} \tag{3.4.1}$$

The other one is from the uncertainty of the tracking efficiency obtained by the embedding simulation and 5% was quoted for all particles. Furthermore, we evaluated the variances of several particle identification (PID) cuts. With the excellent PID performance, the differences among the PID cuts are negligible and have a minimal impact on the final systematic error. Thus, these variances were not considered while calculating the systematic uncertainty. The final systematic uncertainty is obtained by the orthogonal combination of errors mentioned above. The details of the systematic uncertainty for all particles are shown in Table 3.3.

3.4.2 Systematic Uncertainty on dN/dy and $\langle p_T \rangle$

The p_T integral yield (dN/dy) for various particles was obtained by adding the yields in the measured p_T region and the unmeasured p_T range, which was extrapolated from the blast-wave function [116]. The specific form of the blast-wave model will be discussed in Sec. 4.1.

The main source of systematic uncertainty for dN/dy originated from the extrapolation of the unmeasured yield at low p_T region. As shown in mid-panel in Fig. 3.4.1. This uncertainty

Table 3.3: Systematic uncertainty of the particle p_T spectra at all rapidity and centrality ranges.

Sources	p	d	t	^{3}He	^{4}He
nHitsFit	3−5%	2−4%	3−5%	2−3%	1−5%
nHitsDedx	1−2%	1−2%	1−2%	1−2%	1−4%
DCA	3−6%	1−4%	3−5%	1−3%	1−5%
Cuts (total)	3−7%	2−5%	3−6%	2−4%	2−6%
Tracking eff.	5%	5%	5%	5%	5%

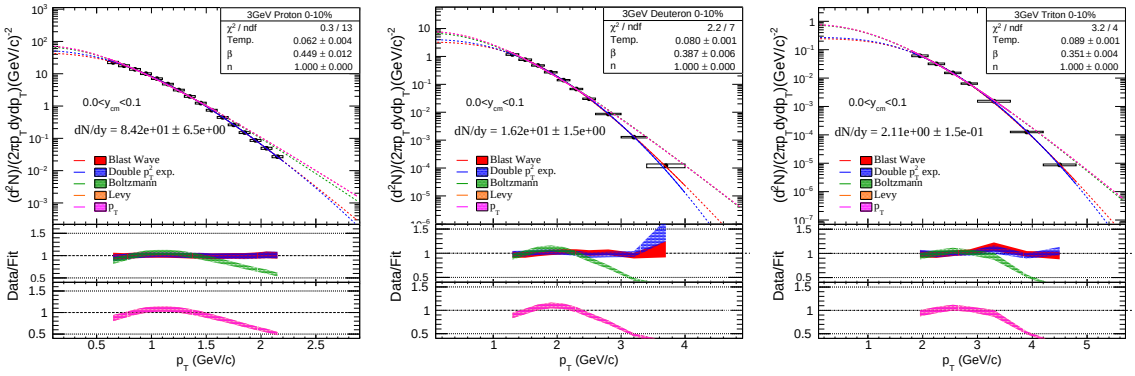

Figure 3.4.1: The p_T spectra of proton, deuteron, and triton at mid-rapidity ($-0.1 < y < 0$) in 0-10% Au+Au collisions at $\sqrt{s_{\rm NN}} = 3\,\text{GeV}$. Colored dashed lines are the results of fitting the function mentioned above.

was estimated by using double p_T^2 exponential function (as shown by Eq. (3.4.2)) to fit the p_T spectra and compare the corresponding extrapolated yields to the default ones obtained from the blast-wave model.

$$\frac{1}{2\pi p_T}\frac{d^2N}{dp_T dy} \propto p_0 \exp\left(\frac{-p_T^2}{p_1}\right) + p_2 \exp\left(\frac{-p_T^2}{p_3}\right), \tag{3.4.2}$$

The systematic uncertainties from the extrapolation at different centralities are about 3-6% for protons and increase for light nuclei with a maximum contribution to 18% for ^{4}He. The final systematic uncertainties were calculated by using quadrature summation of the uncertainties from extrapolation and tracking efficiency (5%). The total uncertainties were about 6-8% for protons, 6-12% for deuteron, 6-11% for triton, 7-11% for ^{3}He, and 6-20% for ^{4}He, respectively.

For the $\langle p_T \rangle$ of particles, the systematic uncertainties were estimated in the same way as for dN/dy (from extrapolation part) and the total systematic uncertainties on $\langle p_T \rangle$ are 1-3% for protons, 3-9% for deuterons, 5-13% for tritons, 3-12% for ^{3}He, and 3-12% for ^{4}He.

3.4.3 Systematic Uncertainty on Full Phase Space Yield

To fit the dN/dy distribution of particle, we obtained the yield for full phase space (4π yield). The dN/dy distributions were fitted by the three-Gaussians function and the modified generalized Gaussian function [117–119]. The determination of this fit function is based on the assumption that there are three emission sources for the observable particles: one at mid-rapidity and two located to the beam/target rapidity. The modified generalized Gaussian function can be expressed by Eq. (3.4.3).

$$Fitfunc. = p_0 \cdot \left(\frac{e^{-\frac{1}{2}\left(\frac{\log\left(1-\frac{k}{p}(x-x1)\right)}{k}\right)^2}}{\sqrt{2\pi}\cdot(p-k\cdot(x-x1))} + \frac{e^{-\frac{1}{2}\left(\frac{\log\left(1+\frac{k}{p}(x+x1)\right)}{k}\right)^2}}{\sqrt{2\pi}\cdot(p+k\cdot(x+x1))} \right) + p_4 \cdot e^{-0.5\cdot\left(\frac{x-p_5}{p_6}\right)^2} \tag{3.4.3}$$

where the parts in parentheses are the variant of the standard form of the generalized Gaussian distribution (GGD) function [118]: $p(x;\alpha,\beta) = \frac{\alpha}{2\beta\Gamma(1/\alpha)} e^{-(|x|/\beta)^\alpha}, \alpha,\beta > 0$. The distribution is symmetric around $x = 0$ and typically has a sharp peak at $x = 0$. k, p, and $x1$

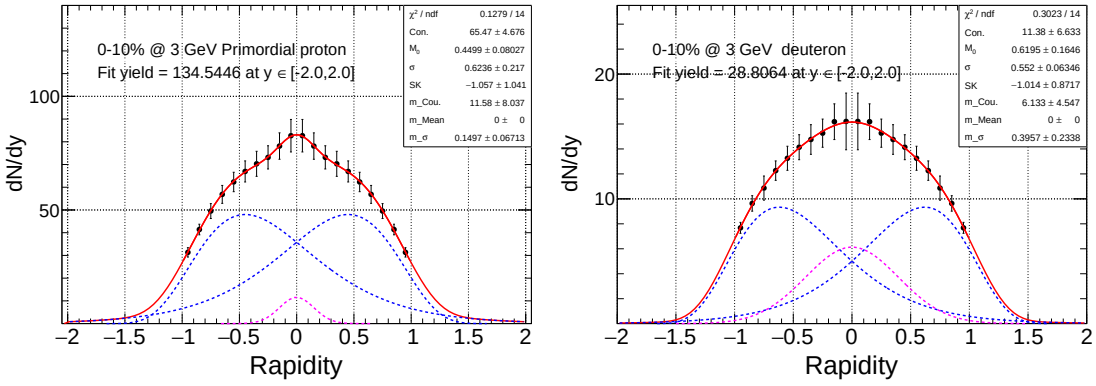

Figure 3.4.2: The rapidity distribution for proton and deuteron in 0-10% Au+Au collisions. Red line is fitted by the modified generalized Gaussian function. Dashed lines are the result of fitting each of the three parts of Eq. (3.4.3).

in the formula are given in the following forms:

$$A = p_3^2 + \sqrt{p_3^4 + 4p_3^2} + 2 \tag{3.4.4}$$

$$k = \sqrt{\log\left[\left(\frac{A}{2}\right)^{\frac{1}{3}} + \left(\frac{2}{A}\right)^{\frac{1}{3}} - 1\right]} \tag{3.4.5}$$

$$p = p_2 \cdot k \cdot \frac{e^{-\frac{1}{2}k^2}}{\sqrt{e^{k^2} - 1}} \tag{3.4.6}$$

$$x1 = \frac{p_1 \cdot k \cdot e^{k^2} + p\left(1 - e^{k^2}\right)}{k \cdot e^{k^2}} \tag{3.4.7}$$

with the above functions, the sharp peak will be at $\pm p_1$. p_2 is standard deviation, p_3 represents skewness. The part outside the parentheses is a Gaussian function with expected value $p_5 = 0$, which is determined from the mid-rapidity emission source. Figure 3.4.2 and Fig. 3.4.3 illustrate the fitting results of the two fitting functions, both of which can well describe the fastness distribution of the particles.

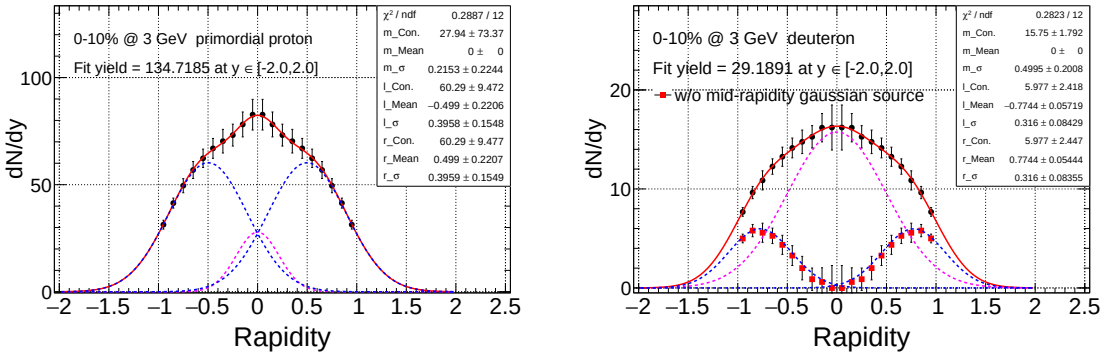

Figure 3.4.3: The rapidity distribution for proton and deuteron in 0-10% Au+Au collisions. Red line is fitted by the three-Gaussians function. Dashed lines are the result of fitting each of the three parts.

The 4π yield was obtained by summing the true value of the measured region with the fitted value of the unmeasured region. The average of the two fits outside the target rapidity region ($1.0 < |y| < 2.0$) is used as the yield value of the extrapolation region.

The systematic uncertainty of the 4π yield, in the measured rapidity region ($-1.0 < y < 0$), is the sum of the measured dN/dy systematic errors. For the unmeasured region, the discrepancy between the two fits described above was considered the systematic uncertainty. Finally, the systematic uncertainties of the 4π yields are 6-11% for protons, 7-20% for deuterons, 11-28% for tritons, 13-25% for ^{3}He, and 14-28% for ^{4}He. Table 4.1 lists the values, statistical, and systematic uncertainties for each particle and all centrality bins.

3.4.4 Systematic Uncertainty on Compound Yield Ratio

For the systematic uncertainties of compound yield ratios, the default yield ratios were obtained by fitting the spectra with the blast-wave model. Different functions, such as the double p_T exponential function (Eq. (3.4.2)), Boltzmann function (Eq. (3.4.8)), Levy function (Eq. (3.4.9)), and m_T exponential function (Eq. (3.4.10)) were also applied to calculate the yield ratio.

Boltzmann:

$$\frac{1}{2\pi m_T}\frac{d^2N}{dm_T dy} \propto p_0 m_{\mathrm{T}} \exp\left(\frac{-m_{\mathrm{T}}}{p_1}\right) \tag{3.4.8}$$

Levy:

$$\frac{1}{2\pi m_T}\frac{d^2N}{dm_T dy} \propto p_0 \left(1+\frac{m_{\mathrm{T}}-m_0}{p_1 p_2}\right)^{-p_1} \tag{3.4.9}$$

m_T exponential:

$$\frac{1}{2\pi m_T}\frac{d^2N}{dm_T dy} \propto p_0 \exp\left(\frac{-m_{\mathrm{T}}}{p_1}\right) \tag{3.4.10}$$

Figure 3.4.1 shows the fitting informations for proton, deuteron, and triton as an example. For each fit, calculate the corresponding particle yield and yield ratio. The differences between those results and the default value were the main source of systematic uncertainty. The total systematic uncertainty for the ratio ($N_p \times N_t/N_d^2$) was about 2-15% for different rapidity and centrality bins. The systematic uncertainty increased to 25% when we considered ^{3}He, and ^{4}He in the yield ratio.

Chapter 4

Results and Discussions

4.1 Transverse Momentum Spectra

Figure 4.1.1 - Fig. 4.1.5 show the transverse momentum spectra (p_T) for primordial proton, deuteron, triton, ^{3}He and ^{4}He in 0-10%, 10-20%, 20-40%, and 40-80% Au+Au collisions at $\sqrt{s_{\rm NN}} = 3$ GeV. The results are shown in various rapidity windows with bin width of 0.1. For illustration purpose, the data points are scaled by a factor from 1 at mid-rapidity to 10^{-9} at target rapidity. As shown in phase space figure, the particle spectra can be measured at lower p_T for target rapidity and mid-rapidity. The dotted lines represent the blast-wave model fit, which can be expressed by Eq. (4.1.1)

$$\frac{1}{2\pi p_T}\frac{d^2N}{dp_T dy} \propto \int_0^R r dr m_T I_0\left(\frac{p_T \sinh\rho(r)}{T_{kin}}\right) K_1\left(\frac{m_T \cosh\rho(r)}{T_{kin}}\right), \tag{4.1.1}$$

where m_T is the transverse mass of particle, I_0 and K_1 are the modified Bessel functions, T_{kin} is the kinetic freeze-out temperature, and $\rho(r) = \tanh^{-1}\beta_T$ is the velocity profile, respectively. The transverse radial flow velocity β_T in the region $0 \leq r \leq R$ can be expressed as $\beta_T = \beta_S(r/R)^n$, where β_S is the surface velocity, r/R is relative radial extent of the thermal source, and the exponent n reflects the form of the flow velocity profile (fixed $n = 1$ in this analysis). $\langle\beta_T\rangle$ can be obtained from $\langle\beta_T\rangle = \frac{2}{2+n}\beta_S$. The temperature T_{kin} as a free parameter can be extracted directly from the fit.

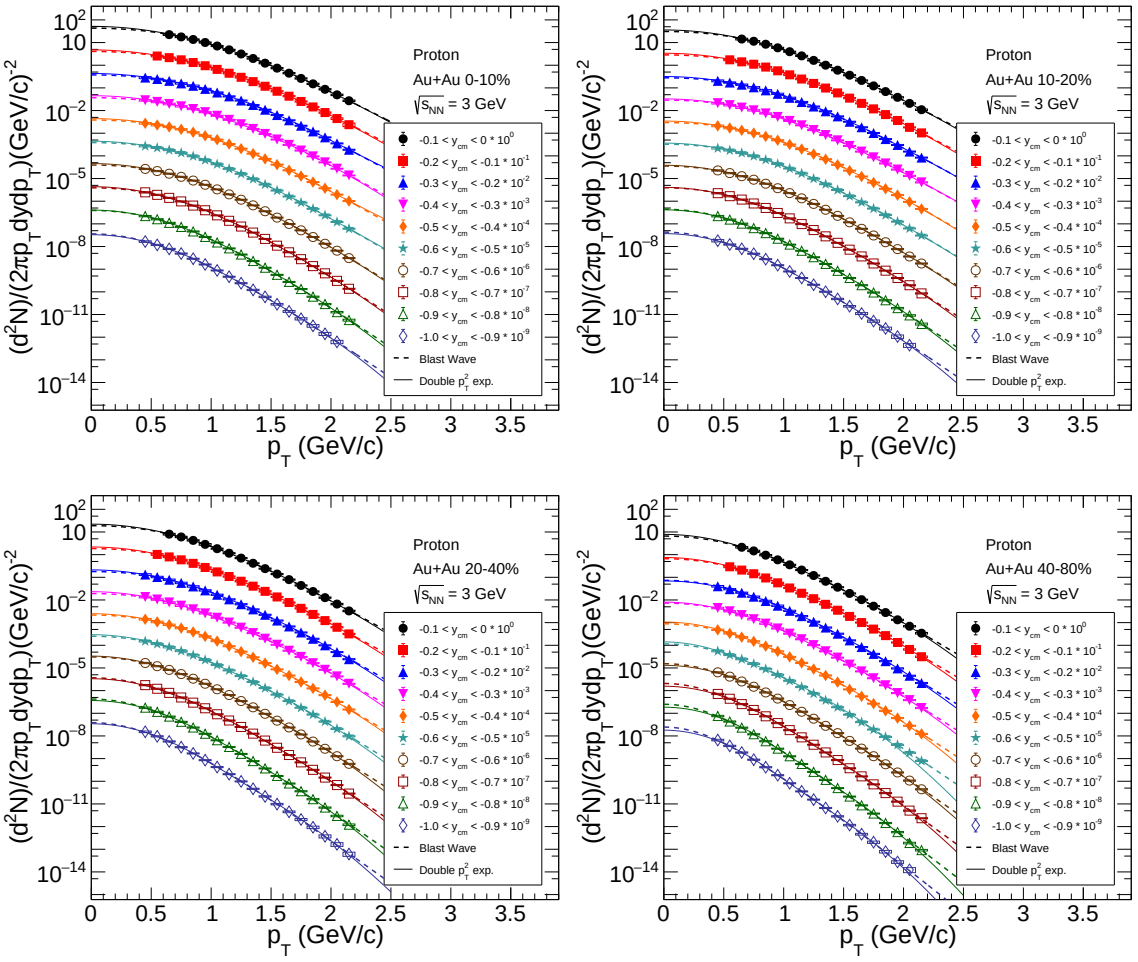

Figure 4.1.1: Transverse momentum spectra (p_T) of protons from different rapidity ranges and centrality bins in Au+Au collisions at $\sqrt{s_{\rm NN}}$ = 3 GeV. For illustration purpose, those spectra are scaled by a factor from 1 at mid-rapidity to 10^{-9} at target rapidity. Systematic uncertainties are represented by boxes. The dotted lines are blast-wave model fits.

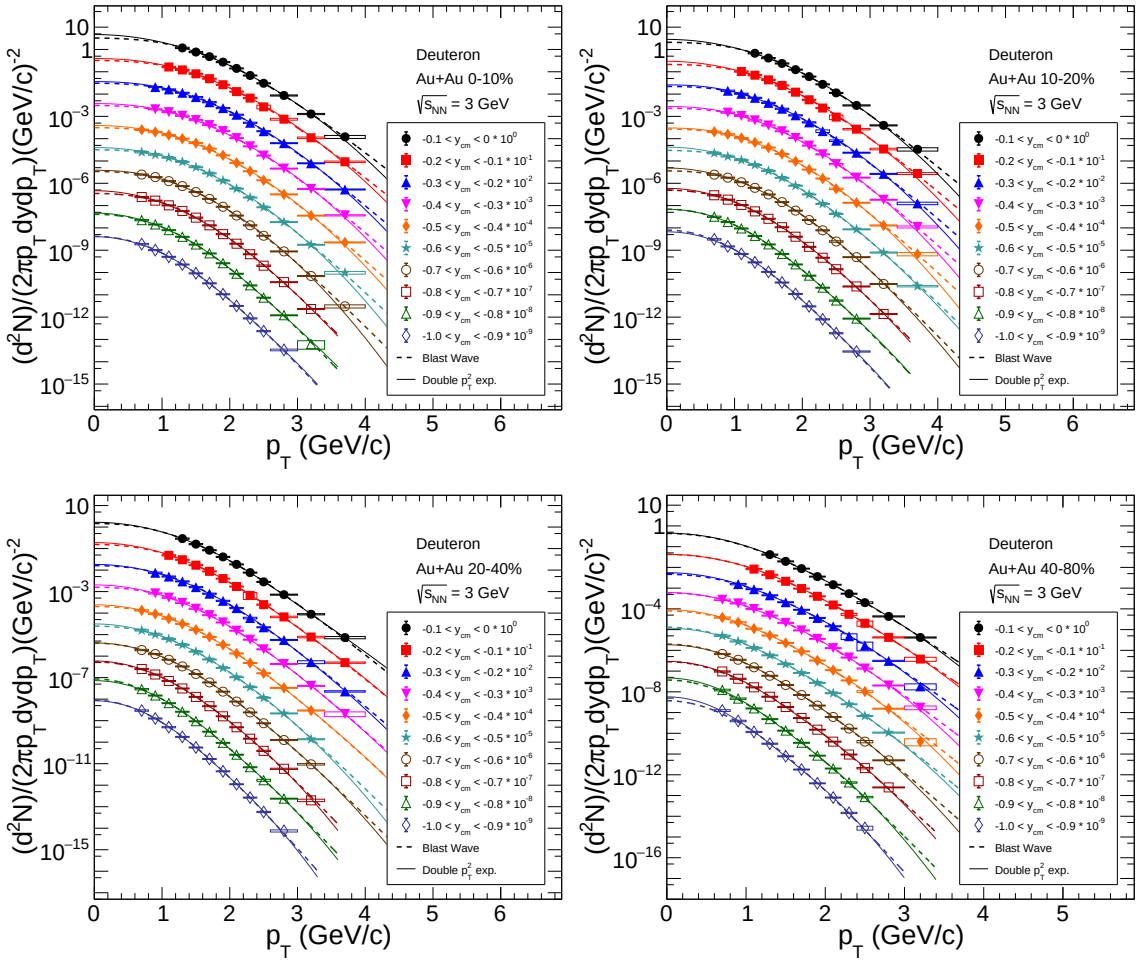

Figure 4.1.2: Transverse momentum spectra (p_T) of deuterons from different rapidity ranges and centrality bins in Au+Au collisions at $\sqrt{s_{\rm NN}} = 3$ GeV.

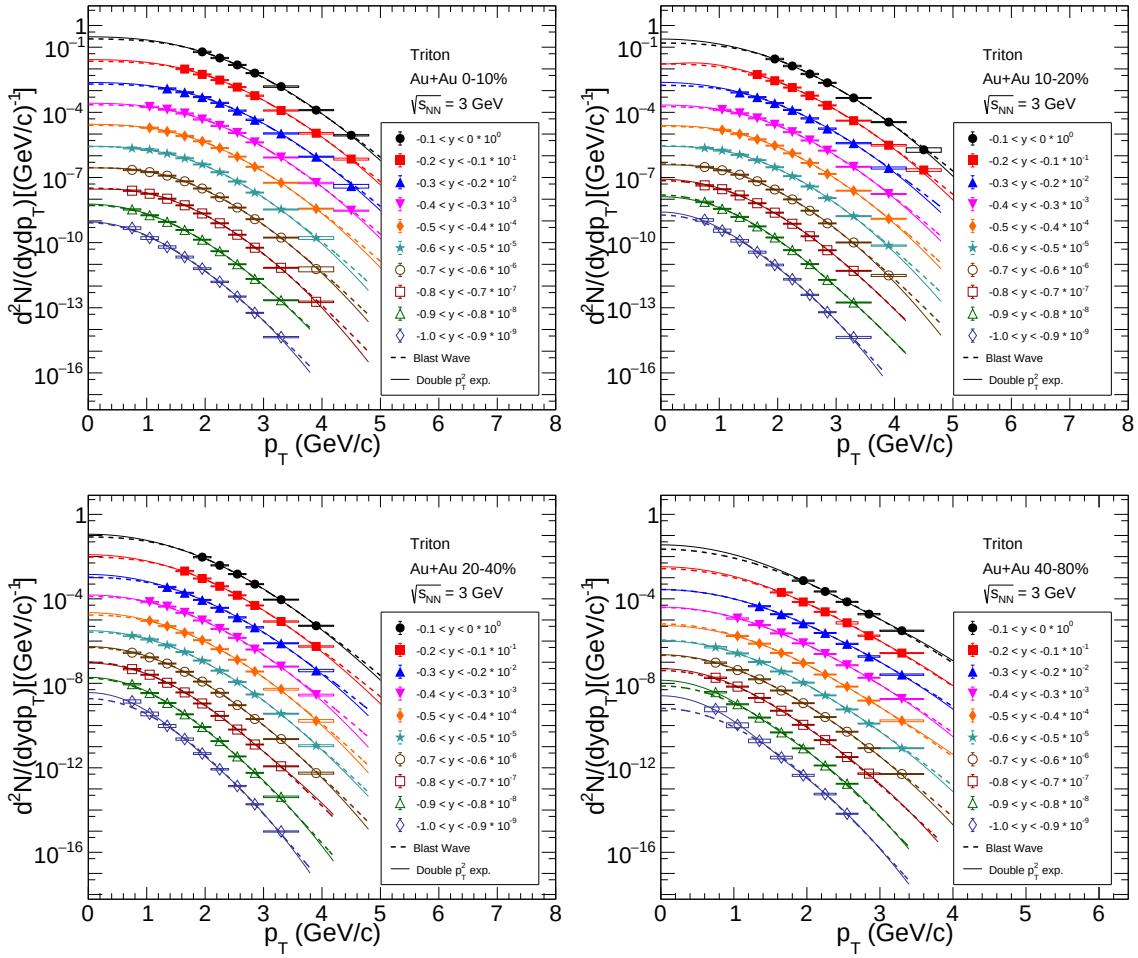

Figure 4.1.3: Transverse momentum spectra (p_T) of tritons from different rapidity ranges and centrality bins in Au+Au collisions at $\sqrt{s_{\rm NN}} = 3$ GeV.

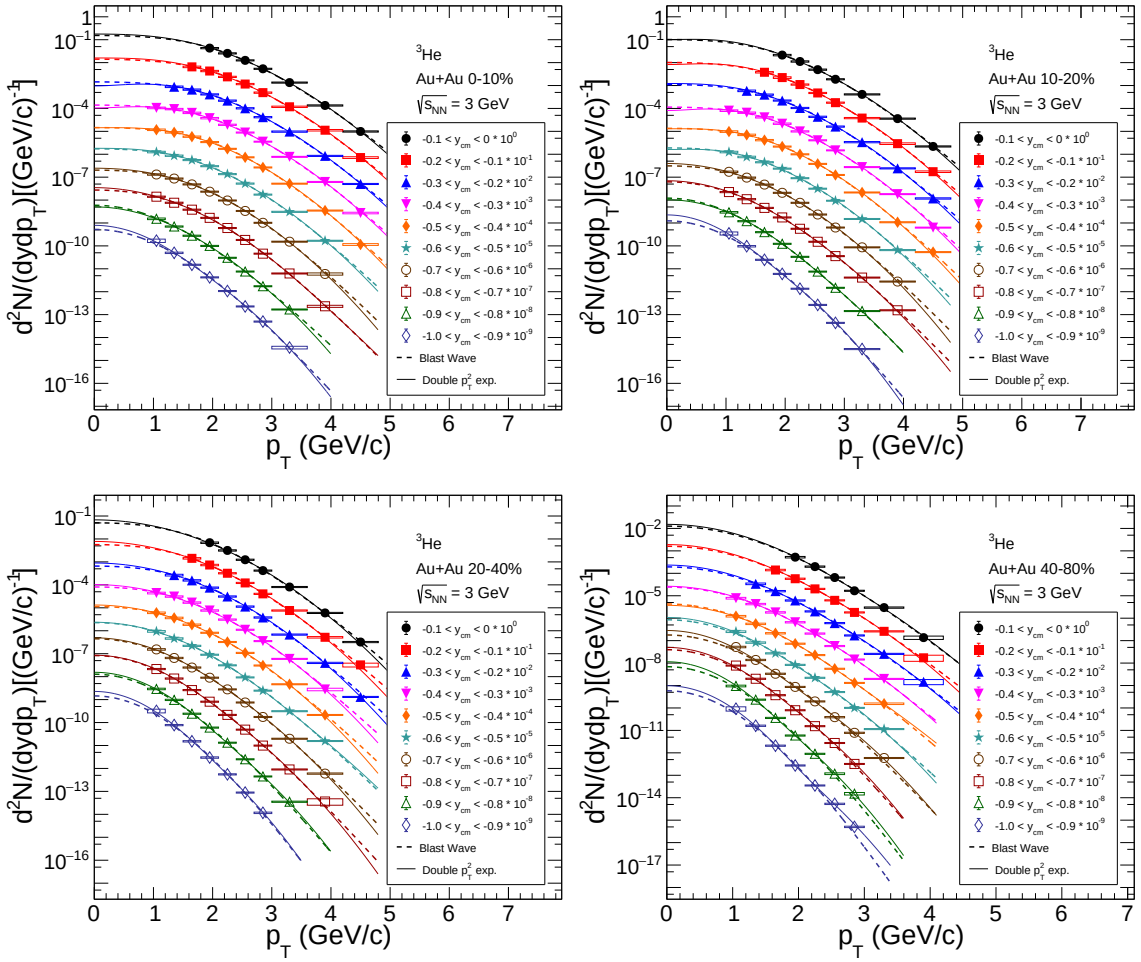

Figure 4.1.4: Transverse momentum spectra (p_T) of ^{3}He from different rapidity ranges and centrality bins in Au+Au collisions at $\sqrt{s_{\rm NN}} = 3$ GeV.

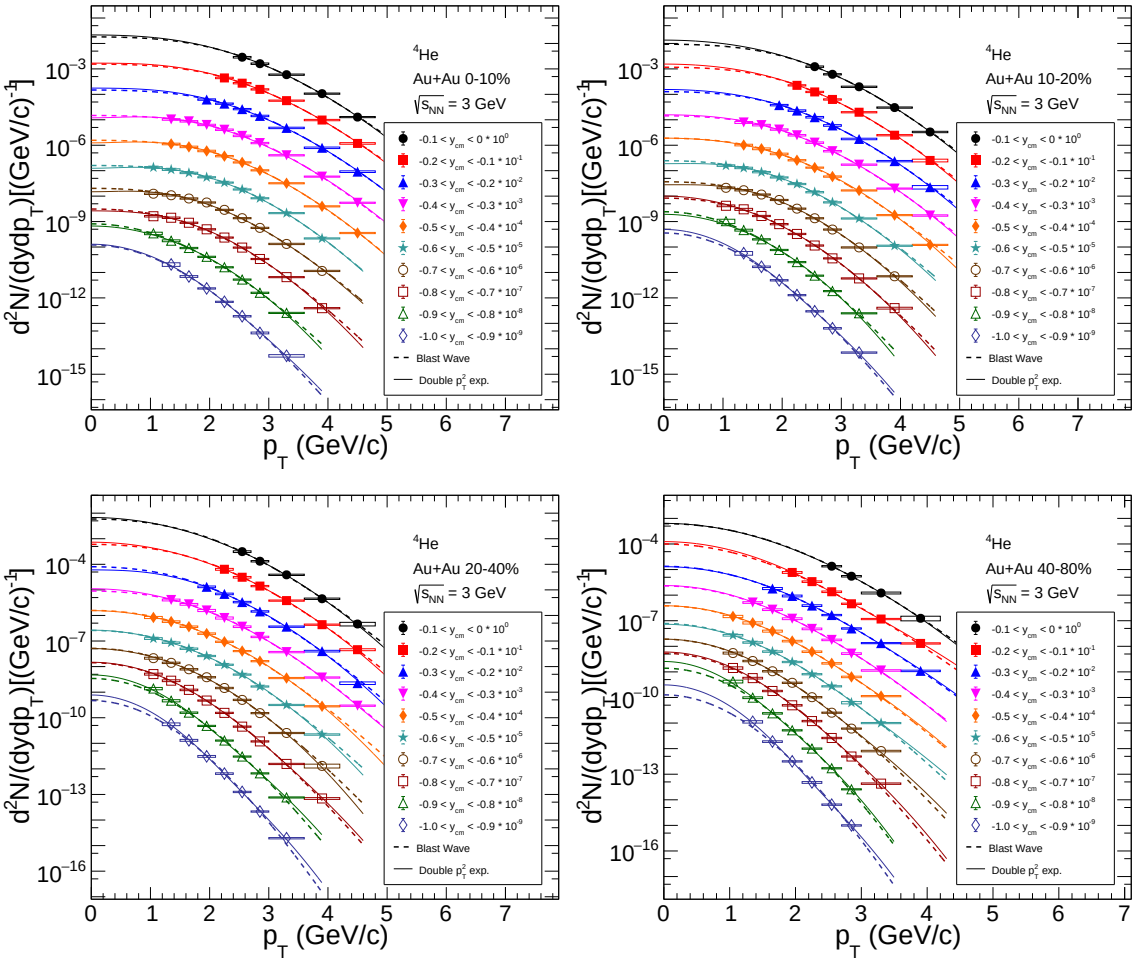

Figure 4.1.5: Transverse momentum spectra (p_T) of ^{4}He from different rapidity ranges and centrality bins in Au+Au collisions at $\sqrt{s_{\rm NN}} = 3$ GeV.

4.2 Averaged Transverse Momentum ($\langle p_T \rangle$)

The averaged transverse momentum $\langle p_T \rangle$ was calculated from the measured p_T range and extrapolated to the unmeasured region with individual blast-wave model fits. The rapidity dependence of $\langle p_T \rangle$ for $p, d, t,^3$He, and ^{4}He in 0-10%, 10-20%, 20-40%, and 40-80% Au+Au collisions at $\sqrt{s_{\rm NN}} = 3$ GeV is shown in Fig. 4.2.1. The $\langle p_T \rangle$ of each particle shows a trend of monotonically decreasing from mid-rapidity to target rapidity and from central to peripheral collisions.

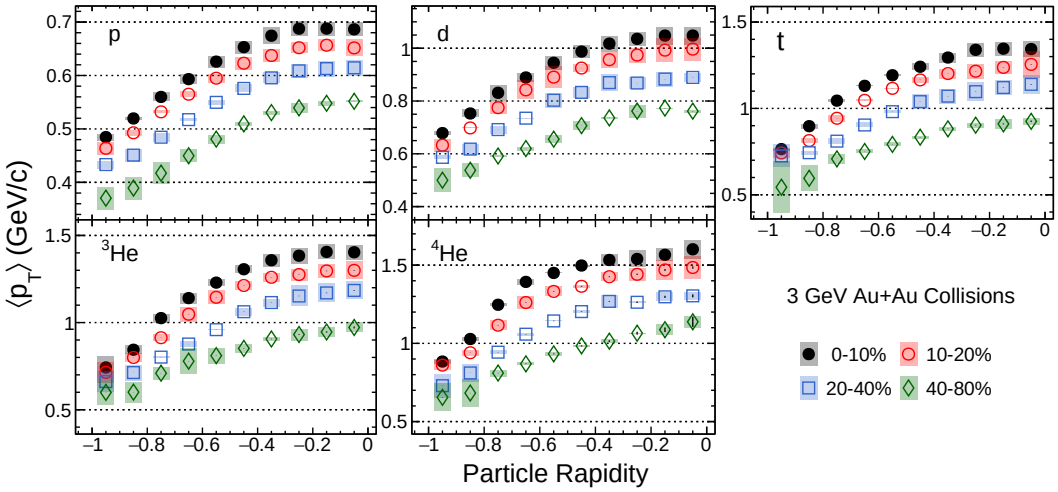

Figure 4.2.1: Collision centrality and particle rapidity dependence of averaged transverse momentum $\langle p_T \rangle$ of protons and light nuclei from Au+Au collisions at $\sqrt{s_{\rm NN}} = 3$ GeV. The boxes indicate systematic uncertainties.

4.3 dN/dy and Full Phase Space Yields of Particle

Figure 4.2.2 shows the rapidity dependence of the p_T integrated yield (dN/dy) for primordial protons and light nuclei in 0-10%, 10-20%, 20-40%, and 40-80% central Au+Au collisions at $\sqrt{s_{\rm NN}} = 3$ GeV. In each panel, different markers represent the distributions for different particles. Due to the interplay between baryon stopping and spectators' contribution, the dN/dy of protons and deuterons decrease from middle to target rapidity in the 0-10% most central collisions, while in peripheral collisions, the values of dN/dy are peaked near the target rapidity. For tritons, ^{3}He, and ^{4}He, the peak structures at target rapidity are increasingly prominent as we move from central to peripheral collisions, due primarily to the fragmentation of the spectators [120]. Calculations of proton and light nuclei dN/dy distributions using the

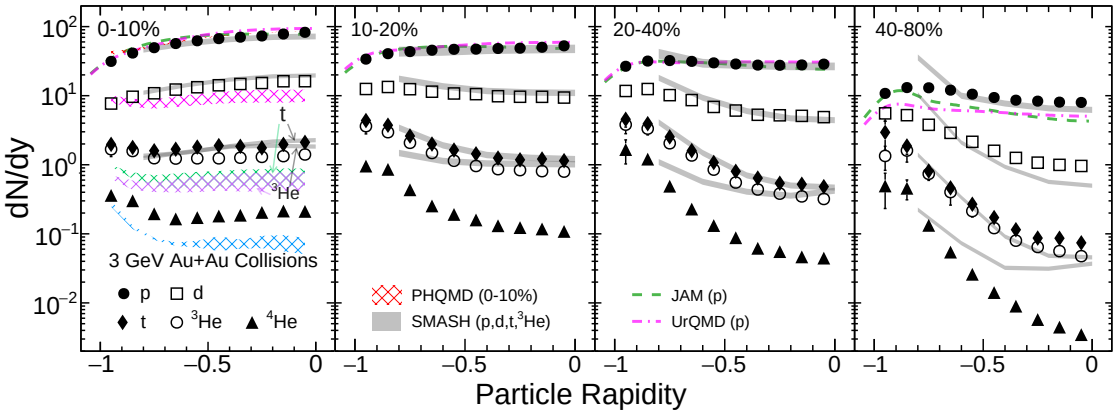

Figure 4.2.2: Collision centrality dependence of primordial protons and light nuclei dN/dy from Au+Au collisions at $\sqrt{s_{\rm NN}}$ = 3 GeV. The vertical lines represent the orthogonal sum of statistical and systematic errors. The gray bands and colored dotted lines are results from the hadronic transport model (SMASH of p, d, t, and ^{3}He, JAM and UrQMD of p) calculations for all centralities. The colored grid bands are results from PHQMD calculations of p, d, t, ^{3}He, and ^{4}He for the top 0-10% collisions.

hadronic transport models (JAM, PHQMD, SMASH, and UrQMD) were compared with the experimental data. The rapidity distributions of protons dN/dy in 0-10%, 10-20%, and 20-40% centrality bins can be well described by the models. For SMASH model calculations of light nuclei (d, t, and ^{3}He), the Wigner function [88, 121] was used to compute their formation probability. It was found that the rapidity distributions of d and t were well described by the SMASH model in central and mid-central collisions. On the other hand, in the PHQMD model calculations, clusters were dynamically formed using attractive interactions and identified with an advanced Minimum Spanning Tree (aMST) in coordinate space [122, 123]. The only parameter, the MST radius, is set to $r = 4\ fm$. As one can see in Fig. 4.2.3 (colored grid bands), in central collisions, although the PHQMD model result of proton rapidity distribution is consistent with data, the yields of d, t, ^{3}He, and ^{4}He were all underpredicted at the mid-rapidity.

As we mentioned on Section 3.4.3, to obtain the 4π yield, the dN/dy distributions were fitted by the three-Gaussians function and the modified generalized Gaussian function shows by Eq. (3.4.3). The 4π yield was obtained by summing the true value of the measured region with the fitted value of the unmeasured region. As shown by the red and blue lines in Fig. 4.2.3, they represent the fitting results of the generalized Gaussian and three-Gaussians functions. The average of the two fits outside the target rapidity region ($1.0 < |y| < 2.0$) is used as the yield value of the extrapolation region. Table 4.1 lists the values, statistical, and systematic

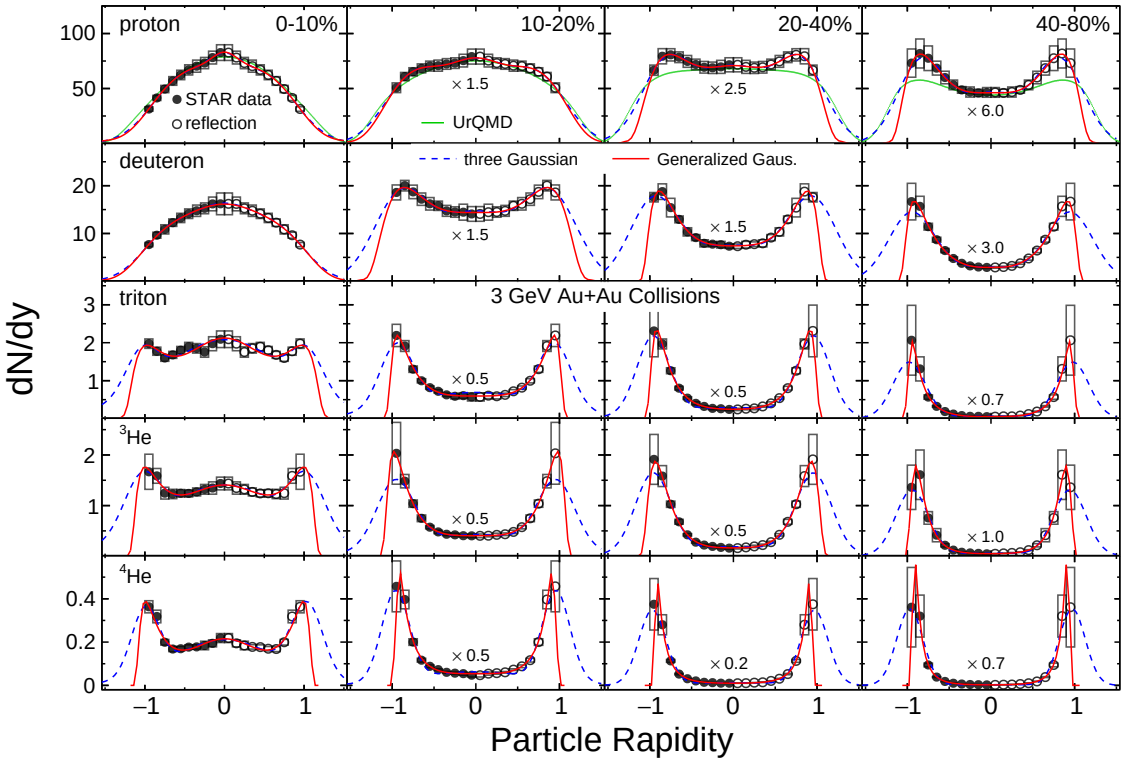

Figure 4.2.3: Particle rapidity dependence of protons and light nuclei dN/dy from Au+Au collisions at $\sqrt{s_{\rm NN}}$ = 3 GeV. For illustrative purposes, the maximum values of non-central collisions are scaled to the most central collision of the same particle. The blue and red lines represent the distribution fit by the three Gaussian and the generalized Gaussian functions. The green line represents the proton distribution from the UrQMD model, with values scaled by the scale factor between the model and the experiment at mid-rapidity.

uncertainties for each particle and all centrality bins.

Table 4.1: 4π yield for primordial protons and light nuclei. The errors represent statistical and systematic (from measurements and fitting) uncertainties, respectively.

Centrality	$0-10\%$	$10-20\%$	$20-40\%$	$40-80\%$
proton	$134.78 \pm 0.10 \pm 8.64$	$105.47 \pm 0.09 \pm 6.50$	$66.82 \pm 0.05 \pm 5.43$	$23.38 \pm 0.03 \pm 2.65$
deuteron	$29.03 \pm 0.05 \pm 2.10$	$27.34 \pm 0.05 \pm 2.56$	$19.33 \pm 0.03 \pm 3.50$	$6.66 \pm 0.01 \pm 1.36$
triton	$4.70 \pm 0.02 \pm 0.47$	$5.15 \pm 0.02 \pm 0.90$	$4.32 \pm 0.01 \pm 0.97$	$1.86 \pm 0.01 \pm 0.48$
^{3}He	$3.55 \pm 0.02 \pm 0.48$	$4.28 \pm 0.02 \pm 0.62$	$3.57 \pm 0.01 \pm 0.71$	$1.20 \pm 0.01 \pm 0.26$
^{4}He	$0.56 \pm 0.01 \pm 0.08$	$0.84 \pm 0.01 \pm 0.17$	$1.06 \pm 0.01 \pm 0.26$	$0.33 \pm 0.01 \pm 0.08$

4.4 Particle Mass Dependence of dN/dy and $\langle p_T \rangle$

Figure 4.4.1 shows the mid-rapidity dN/dy, the dN/dy ratio of target rapidity ($-1.0 < y \leq -0.9$) to mid-rapidity ($-0.1 < y \leq 0$), and $\langle p_T \rangle$ as a function of particle mass for four centralities. The dN/dy values for different particles are scaled by their corresponding spin degeneracy factor $(2\mathrm{J}+1)$ [43, 91], which is explained by the fact that the yield is found to be proportional to the spin coefficient in a statistical approach to light nuclei formation. Fitting this distribution with an exponential function form: p_0/P^{A-1}, where P is the penalty factor and determined by the Boltzmann factor $e^{(m_N-\mu_B)/T}$ [124–127]. The penalty factor is about 6.1 $\pm$ 0.5 and 10.5 $\pm$ 0.8 for the most central and peripheral Au+Au collisions at $\sqrt{s_{\mathrm{NN}}} =$ 3 GeV, respectively. The uncertainty of the penalty factor is obtained from the difference in the fit of different particle combinations. Figure 4.4.2 illustrates the results of these fits. The black dashed line represents the result of fitting all particles simultaneously, as the mean value of the penalty factor. The blue long dashed line and the red dotted line are fitting with $(p, d,^3\mathrm{He},^4\mathrm{He})$ and (p, d, t) and are used as sources of uncertainty.

Figure 4.4.1 (b) shows that the $\langle p_T \rangle$ increases linearly with increasing mass of the particle and exhibits centrality dependence. This reflects that the collective expansion in the radial direction is stronger in central collisions than in peripheral collisions. Figure 4.4.1 (c) shows the ratio of the dN/dy values measured at target rapidity to mid-rapidity as a function of particle mass. The ratio reveals the relative contributions of nuclear fragmentation to the yields of light nuclei at different collision centralities and particle mass. The ratio increases exponentially with increasing particle mass, with this upward trend being more pronounced in peripheral collisions compared to central collisions. It indicates that, as the light nuclei become heavier, the proportion of contributions originating from the nuclear fragments increases.

The energy dependence of dN/dy and $\langle p_T \rangle$ versus particle mass in 0-10% Au+Au collisions

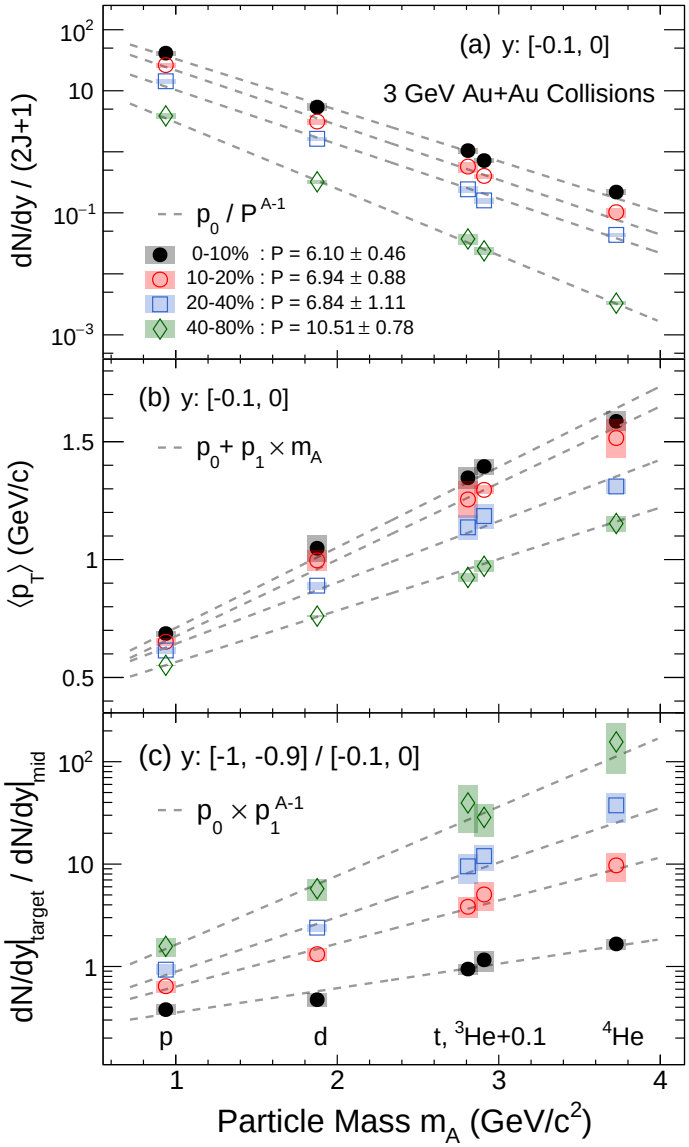

Figure 4.4.1: (a) Mid-rapidity particle yields dN/dy, (b) mean transverse momentum $\langle p_T \rangle$, and (c) ratio of the dN/dy measured at target rapidity ($-1.0 < y < -0.9$) to mid-rapidity ($-0.1 < y < 0$) as a function of collision centrality and particle mass m_A (A is mass number) from Au+Au collisions at $\sqrt{s_{\rm NN}} = 3$ GeV. For clarity, the mass of ^{3}He is shifted by 0.1 GeV/c^2. The boxes represent the quadratic sum of the measured statistical uncertainties and the extrapolation uncertainties. Dashed lines are fitting results of an exponential function to (a) the yields and (c) the yields ratio, and first-order polynomial (b) mean $\langle p_T \rangle$, respectively.

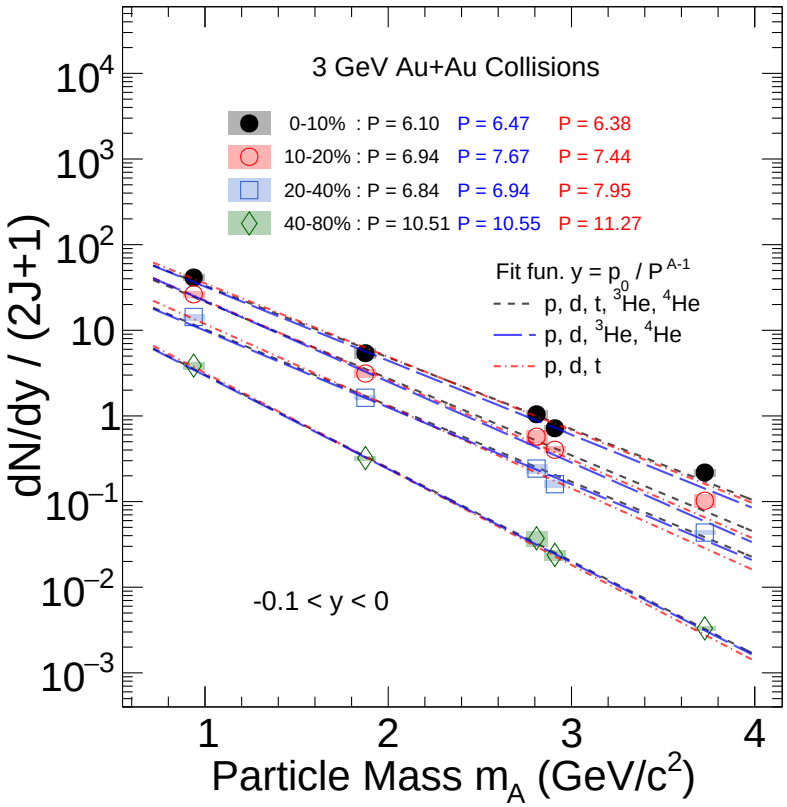

Figure 4.4.2: Mid-rapidity particle yields dN/dy as a function of collision centrality and particle mass m_A from Au+Au collisions at $\sqrt{s_{\rm NN}} = 3$ GeV. Lines of different colors and styles represent the results of different fits and are used to calculate the uncertainty of the penalty factor.

at mid-rapidity are shown in Fig. 4.4.3, for the $\sqrt{s_{\rm NN}}$ = 7.7 – 200 GeV collisions, the yields of p, d, and t are taken from Refs. [59, 62, 128, 129]. The left panel shows that the penalty factor P increases with increasing collision energy, indicate that the higher the energy is, the more difficult is it to form light nuclei. The right panel illustrates the linear distribution of $\langle p_T \rangle$ with particle mass ($m_{\rm A}$) or nucleon number (A) observed at all collision energy.

4.5 Particle Ratios

In relativistic heavy ion collisions, the increase in system entropy can be seen as a consequence associated with high energy, high density, and the formation of a quark-gluon plasma [29, 84]. One possible explanation for how light nuclei can survive under the high temperatures of chemical freeze-out is that the system expansion after the chemical freeze–out is supposed

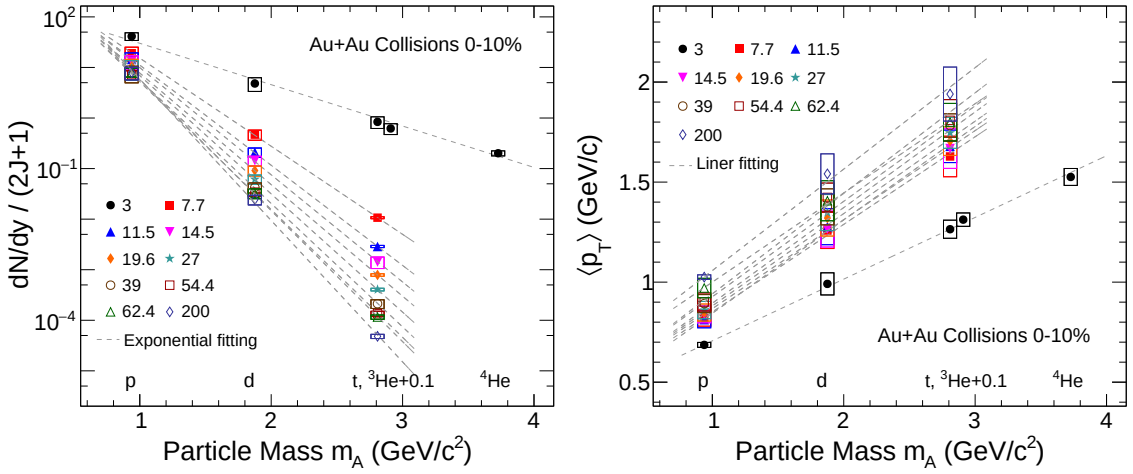

Figure 4.4.3: (left) Mid-rapidity particle yields dN/dy as a function of collision energy and particle mass m_A (A is mass number) from Au+Au collisions. Dashed lines are fitting results of an exponential function. (right) Mean transverse momentum $\langle p_T \rangle$ as a function of collision energy and particle mass m_A. Dashed lines are fitting results of a first-order polynomial function. For clarity, the mass of ^{3}He is shifted by 0.1 GeV/c^2. The vertical lines represent the statistical uncertainties and the boxes represent the systematical uncertainties.

to conserve the entropy density, and this preservation could be a steering mechanism for the nuclei production. Therefore, the ratio of light nuclei to protons can be used as an indicator to reflect the entropy change of the system.

Figure 4.4.4 shows the rapidity and centrality dependence of the light nuclei to proton ratios, include d/p, t/p, ^{3}He$/p$, and ^{4}He$/p$ in Au+Au collisions at $\sqrt{s_{\rm NN}} = 3$ GeV. Based on the conclusions from the previous analysis of spectator contributions, it is found that these particle ratios monotonically decrease from target to mid-rapidity and show stronger rapidity dependence in peripheral collisions than in central collisions. As a comparison, we used the SMASH + Coalescence (gray bands) model to calculate the particle ratios (d/p and t/p), those give the same rapidity and centrality dependence with STAR experimental data. However, the ratio of ^{3}He$/p$ exhibits weaker rapidity dependence than the experiment data. In addition, using the parameters $T = 85$ MeV, $\mu_B = 728$ MeV [130], we estimated the mid-rapidity particle yield ratios in 0-10% central collisions from the thermal model without excited nuclei contributions [130, 131]. Ref. [131] states that feeddown corrections are necessary at lower energies. They calculated that at low collision energy, $\sqrt{s_{\rm NN}} \lesssim 10$ GeV, the feed contribution to the d yield can reach up to 30%, while the contribution to t, ^{3}He, and ^{4}He is even greater, up to 70% of the final yield.

The energy dependence of d/p and t/p ratios can be seen in the Fig. 4.5.1. Both the d/p

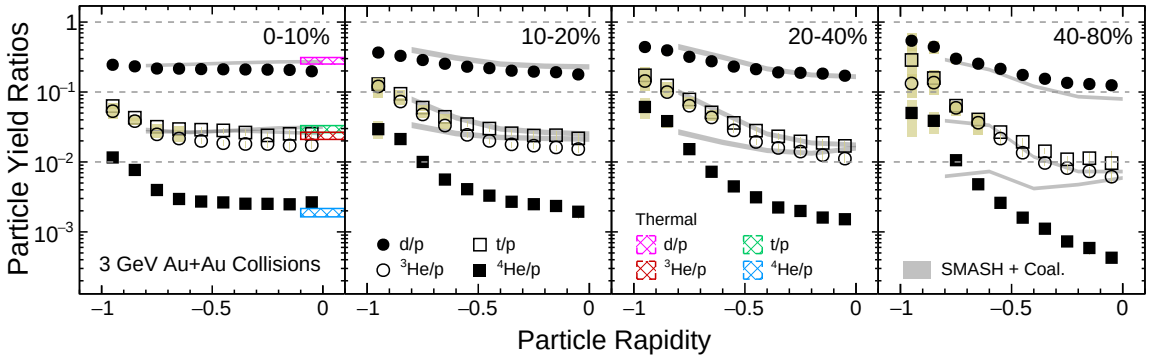

Figure 4.4.4: Rapidity dependence of d/p, t/p, ^{3}He$/p$, and ^{4}He$/p$ for 0-10%, 10-20%, 20-40%, and 40-80% centrality bins in Au+Au collisions at $\sqrt{s_{\rm NN}} = 3$ GeV. The boxes indicate the systematic uncertainties. Color solid lines represent SMASH + Coalescence model results. Color dash lines show thermal model results in most central bin at mid-rapidity.

and t/p at 3 GeV follow the energy dependence trend observed by the STAR BES-I [59, 62], FOPI [34, 37], and AGS [41, 44] experiments, and the values of d/p and t/p are close to each other at very low energies. These ratios obtained from the SMASH model are also on the energy trend. Moreover, as shown in the curves, the trends of d/p and t/p can be described qualitatively by the thermal model [85].

4.6 Coalescence Parameter

In the coalescence picture [132, 133], light nuclei are formed via the coalescence of their constituents (protons and neutrons), thus the relation between the momentum spectra of light nuclei, protons, and neutrons is as follows:

$$E_A \frac{d^3N_A}{d^3p_A} = B_A \left(E_p \frac{d^3N_p}{d^3p_p}\right)^Z \left(E_n \frac{d^3N_n}{d^3p_n}\right)^{A-Z} \approx (1.3)^{A-Z} B_A \left(E_p \frac{d^3N_p}{d^3p_p}\right)^A \Bigg|_{p_p=p_n=\frac{p_A}{A}} \tag{4.6.1}$$

where is assumed the same p_T, rapidity, and centrality dependence between protons and neutrons. The neutron spectrum is derived by scaling the proton spectrum with a factor of $n/p = 1.3 \pm 0.1$. This scaling factor is estimated from the $t/^3$He ratio [52] measured at 3 GeV, and this ratio is consistent with 1.28 calculated by the thermal model. The coalescence parameter $B_A \propto (1/V_{\rm eff})^{(\rm A-1)}$, which is to reflect the kinetic freeze-out property, give the information of coalescence probability of light nuclei with the mass number A. $V_{\rm eff}$ is the

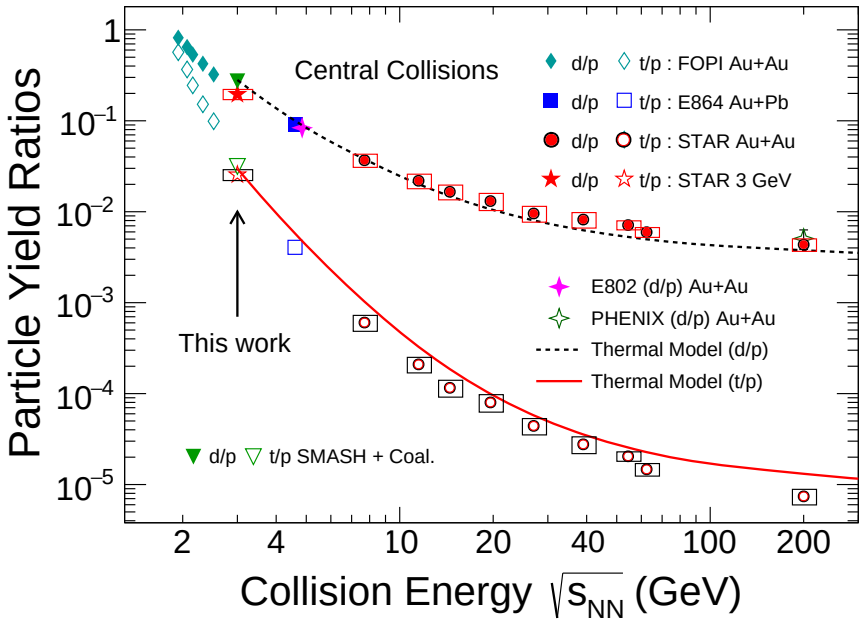

Figure 4.5.1: Energy dependence of d/p and t/p yield ratios. The vertical lines indicate the statistical uncertainties. The boxes indicate the systematic uncertainties. The curves represent the thermal model results.

effective volume of the nucleon emission source.

Figure 4.6.1 shows the rapidity dependence of the coalescence parameters B_2 for deuterons, $\sqrt{B_3}$ for tritons and ^{3}He at $p_T/A = 0.65$ GeV/c in different centrality bins. B_2 and $\sqrt{B_3}$ are consistent, the observed rapidity dependence of them is weak to negligible. And both B_2 and $\sqrt{B_3}$ increase from central to peripheral collisions and, as mentioned before, these behaviors can be interpreted as the effective source volume getting smaller from central to peripheral collisions.

Figure 4.6.2 describes the scaled transverse momentum dependence of the coalescence parameters for $B_2(d)$, $B_3(t)$, and $B_3(^3\mathrm{He})$ at mid-rapidity in 0-10%, 10-20%, 20-40%, and 40-80% centrality bins. Within the uncertainties, $\sqrt[A-1]{B_A}$ of d(A=2), t(A=3), and ^{3}He(A=3) are consistent, and their values increase with increasing p_T. This increasing trend can be explained by the presence of collective flow [134], and the length of homogeneity becomes smaller at higher transverse momentum [79].

The energy dependence of coalescence parameter in central heavy-ion collisions is shown in Fig. 4.6.3. The experimental data include the measurements from the EOS [127], NA44 [49], AGS [40, 44], PHENIX [55] and STAR BES-I [54, 62] experiments. The mid-rapidity $B_2(d)$, $B_3(t)$, and $B_3(^3\mathrm{He})$ with transverse momentum $p_T/A = 0.65\,\mathrm{GeV/c}$ at $\sqrt{s_{\mathrm{NN}}} = 3\,\mathrm{GeV}$ follows

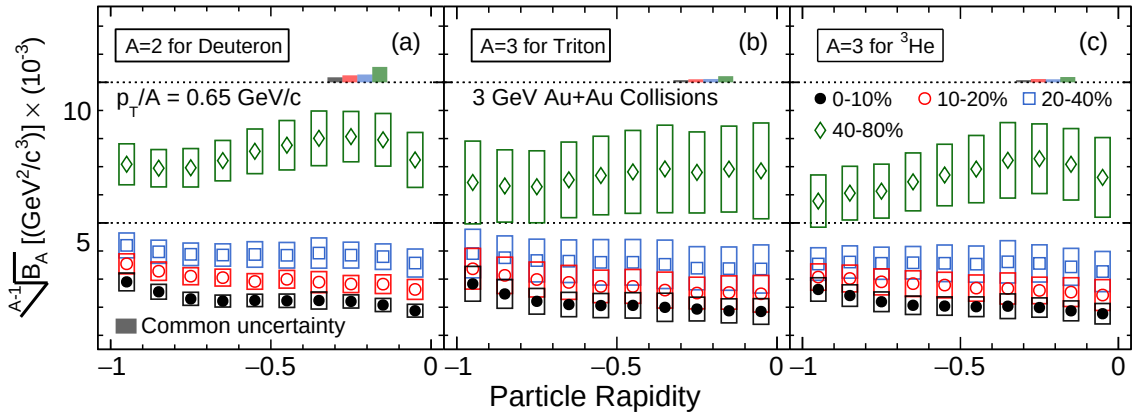

Figure 4.6.1: Rapidity dependence of the coalescence parameter for $B_2(d)$, $B_3(t)$, and $B_3(^3\mathrm{He})$ at $p_T/A = 0.65$ GeV/c for different centrality bins in Au+Au collisions at $\sqrt{s_{\mathrm{NN}}} = 3$ GeV. The boxes represent the systematic uncertainties. The color bands represent the common uncertainties in rapidity dependence.

the world trend, and there is a clear upward trend towards low energy, which implies that the overall effective volume of the nucleon emitting source (V_{eff}) decreases with decreasing collision energies.

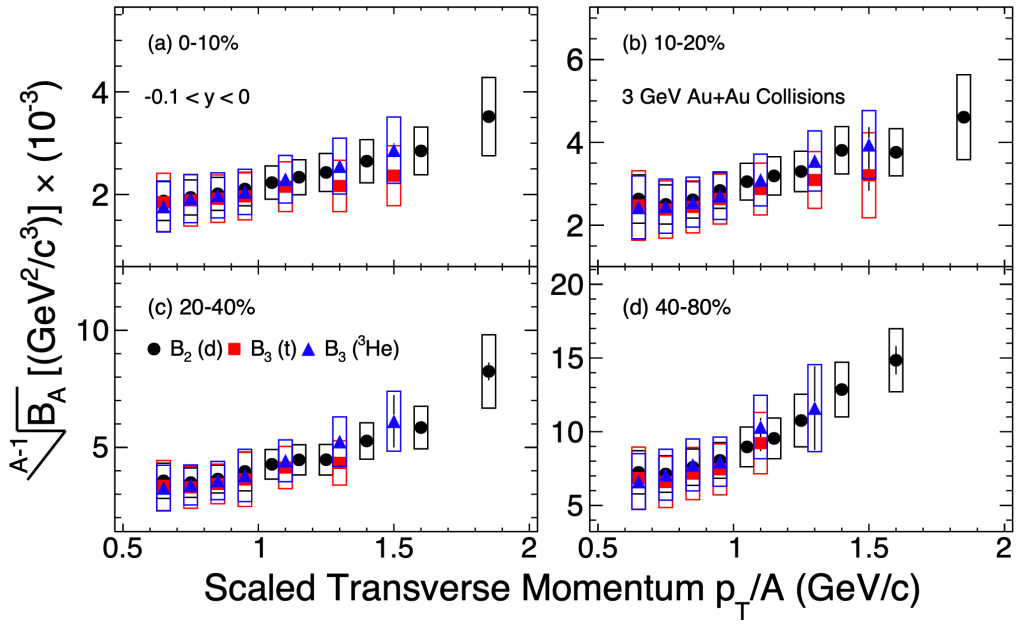

Figure 4.6.2: Coalescence parameters $B_2(d)$, $\sqrt{B_3}(t)$ and $\sqrt{B_3}(^3\mathrm{He})$ as a function of p_T/A for different centrality bins in Au+Au collisions at $\sqrt{s_{\mathrm{NN}}} = 3$ GeV. The boxes represent the systematic uncertainties.

4.7 The Compound Yield Ratio of Light Nuclei

As mentioned in Sec. 1.5, light nuclei are formed in a restricted volume of phase space, their yields are expected to be sensitive to baryon density fluctuations and can be used to probe the QCD critical point and/or the signatures of the first-order phase transition in heavy-ion collisions. Recent research has shown that the charge multiplicity dependence of the yield ratio $N_p \times N_t/N_d^2$ increases in peripheral collisions due to the effects of finite nuclei sizes [30, 79, 135].

In addition, based on the Eq. (1.5.6), the exponential factor can be canceled out by the ratio of the corresponding particles, as the Ref. [34, 90] explained. Thus the $N_p \times N_t/N_d^2$ ratio can be expressed as:

$$\frac{N_p \times N_t}{N_d^2} \simeq 0.29 \frac{\left\langle e^{-3V(r)/T} \right\rangle}{\left\langle e^{-V(r)/T} \right\rangle^2} \tag{4.7.1}$$

where 0.29 is corresponding statistical weight, factor 3 represent there are three nucleon pairs in triton, $V(r)$ is inter-nucleon potential, T is temperature.

For the data set at $\sqrt{s_{\mathrm{NN}}} = 3$ GeV Au+Au collisions, which the production of light nuclei is abundant, offers the possibility to explain the energy dependence of the low energy region

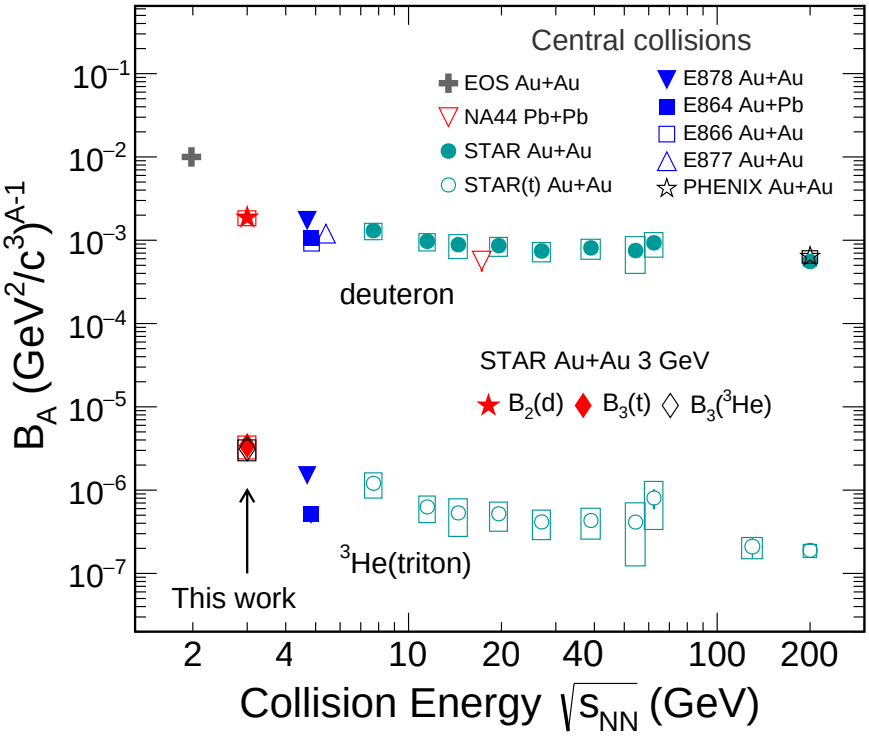

Figure 4.6.3: Energy dependence of the coalescence parameters for $B_2(d)$, $B_3(t,^3\mathrm{He})$ in central collisions. The vertical lines indicate the statistical uncertainties. The boxes indicate systematic uncertainties. For comparison, the results from EOS [127], NA44 (0-10%) [49], AGS (0-10%) [40, 44], PHENIX (0-20%) [55] and STAR BES-I (0-10%) [54, 62] are also shown.

and gives the opportunity to study the higher order yield ratios. Consider ^{3}He and ^{4}He into the calculation of the yield ratio, which can increase the powers of V/T,

$$\frac{N_{^4\mathrm{He}} \times N_p}{N_{^3\mathrm{He}} \times N_d} \simeq 0.18 \frac{\left\langle e^{-6V(r)/T} \right\rangle}{\left\langle e^{-3V(r)/T} \right\rangle \left\langle e^{-V(r)/T} \right\rangle} \tag{4.7.2}$$

where 0.18 is corresponding statistical weight, factor 3 and 6 are the number of nucleon pairs in ^{3}He and ^{4}He.

Figures 4.7.1 shows the rapidity dependence of the yield ratios for $N_p \times N_t/N_d^2, N_{^4\mathrm{He}} \times N_p/\left(N_{^3\mathrm{He}} \times N_d\right)$, and $N_{^4\mathrm{He}} \times N_t \times N_p^2/\left(N_{^3\mathrm{He}} \times N_d^3\right)$ in 0-10%, 10-20%, 20-40% and 40-80%, respectively. There is no obvious centrality dependence for each yield ratio. At mid-rapidity $(-0.5 < y < 0)$ range, there is no obvious rapidity dependence for each ratio, while at target rapidity $(-1.0 < y < -0.5)$ range, the ratio increases from $y = -0.5$ to $y = -1.0$.

Figure 4.7.2 shows the centrality dependence of $N_p \times N_t/N_d^2$, $N_{^4\mathrm{He}} \times N_p/N_{^3\mathrm{He}} \times N_d$, and

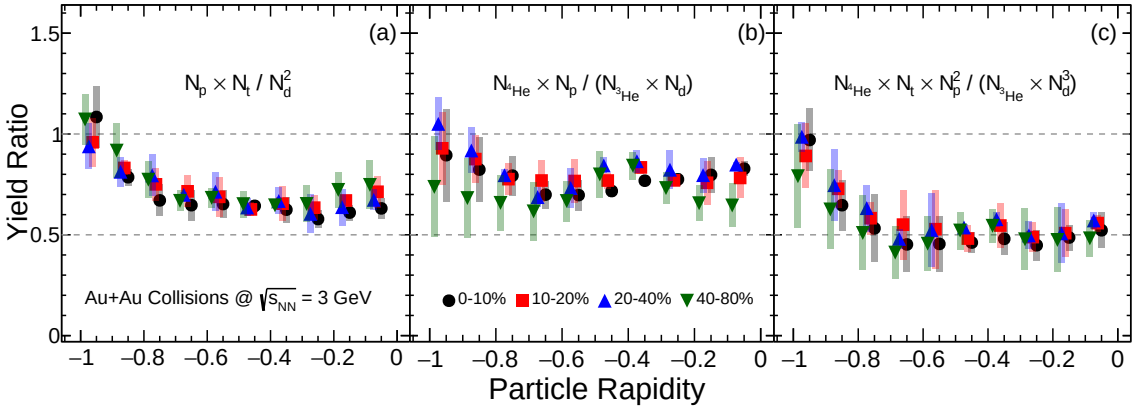

Figure 4.7.1: Rapidity dependence of the yield ratio for $N_p \times N_t/N_d^2, N_{^4\mathrm{He}} \times N_p/(N_{^3\mathrm{He}} \times N_d)$ and $N_{^4\mathrm{He}} \times N_t \times N_p^2/(N_{^3\mathrm{He}} \times N_d^3)$ in different centrality bins in Au+Au collisions at $\sqrt{s_{\mathrm{NN}}} =$ 3 GeV. The bands represent the systematic uncertainties.

$N_{^4\mathrm{He}} \times N_d/(N_{^3\mathrm{He}} \times N_t)$. In each panel, the black solid and open circles denote the results from mid-rapidity ($-0.5 < y < 0$) and target rapidity ($-1 < y < -0.5$), respectively. The experimental results presented in panels (a), (b), and (c) give almost flat centrality dependence. Calculations from various models were applied to compare with the data. In panel (a), the results from SMASH and UrQMD model [136] show monotonically increasing trends from central to peripheral collisions. The result from the thermal model calculation, which include the decay from the excited nuclei to light nuclei (red band), is consistent with the experimental result in central collisions. In recent AMPT calculations [136], implementing a first-order phase transition, which consider the equation of state with critical temperature of $T_c = 154$ GeV (blue band), give a consistent description of the centrality dependence, and the values are consistent with mid-rapidity within the uncertainty. Panel (b) depicts that the $N_{^4\mathrm{He}} \times N_p/(N_{^3\mathrm{He}} \times N_d)$ shows no centrality dependence, and the AMPT model also reproduces this centrality behavior. In the most central collisions, the results of the thermal model are lower than the experimental data whether or not the contribution of excited state decays was considered. In addition, the above two ratios are consistent with the calculations from PHQMD model within the larger uncertainty. In contrast to panel (b), the $N_{^4\mathrm{He}} \times N_d/(N_{^3\mathrm{He}} \times N_t)$ displayed in panel (c) demonstrates that the value from the thermal model is lower than the experimental result in central collisions, while the ratio calculated by the PHQMD model is as high as 1.87 $\pm$0.24, and that only the AMPT model can describe this centrality dependence.

The energy dependence of $N_p \times N_t/N_d^2$ in central heavy-ion collisions at mid-rapidity

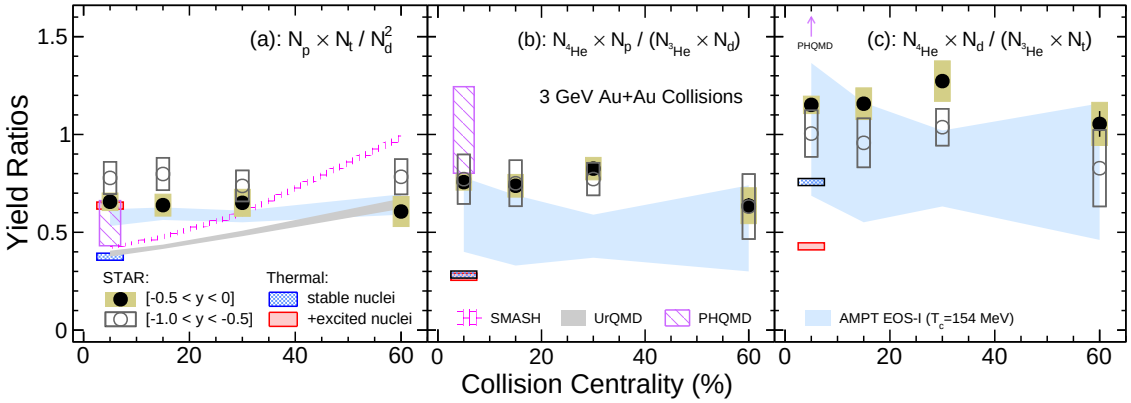

Figure 4.7.2: Centrality and rapidity dependence of the yield ratios $N_p \times N_t/N_d^2$, $N_{^4\mathrm{He}} \times N_p/(N_{^3\mathrm{He}} \times N_d)$, and $N_{^4\mathrm{He}} \times N_d/(N_{^3\mathrm{He}} \times N_t)$ in Au+Au collisions at $\sqrt{s_{\mathrm{NN}}} = 3$ GeV. Solid and open markers indicate ratios from mid-rapidity ($-0.5 < y < 0$) and target rapidity ($-1 < y < -0.5$), respectively. Statistical uncertainties are smaller than the size of the markers and systematic uncertainties are shown by boxes. Results from hadronic transport models UrQMD, SMASH, and AMPT EoS-I are shown by colored bands. For the top 0-10% central collision, results from thermal and PHQMD models are also shown.

($-0.5 < y < 0$) was presented in Fig. 4.7.3. The colored-bands and gray grid represent the calculations obtained from the hadronic transport model AMPT [136] and the hybrid model MUSIC+UrQMD [135], respectively. The black dashed line corresponds to the coalescence baseline obtained by fitting the charged-particle multiplicity dependence of the yield ratio from STAR BES-I data [62] with the coalescence-inspired function given by:

$$\frac{N_p \times N_t}{N_d^2} = p_0 \times \left(\frac{1 + \frac{2r_d^2}{3R^2}}{1 + \frac{r_t^2}{2R^2}}\right)^3 \tag{4.7.3}$$

where $r_d = 1.96$ and $r_t = 1.59$ are the root-mean-square matter radius of deuteron and triton [138], respectively. $R = p_1 \times (dN_{\mathrm{ch}}/d\eta)^{1/3}$ is the radius of Guassian spherical source size.

As mentioned earlier, this yield ratio is proposed as a sensitive observable to probe the nucleon density fluctuation near the QCD critical point and/or first order phase transition. The STAR experiment observed enhancements of the yield ratio relative to the coalescence baseline in 0-10% central Au+Au collisions at $\sqrt{s_{\mathrm{NN}}} = 19.6$ and 27 GeV [62], with a significance of 2.3σ and 3.4σ, respectively. At lower energies, the experimental results from the E864 [44], STAR and FOPI [37] experiments align with the world trend of the energy dependence and monotonically increase with decreasing energies. The thermal model, whether considering

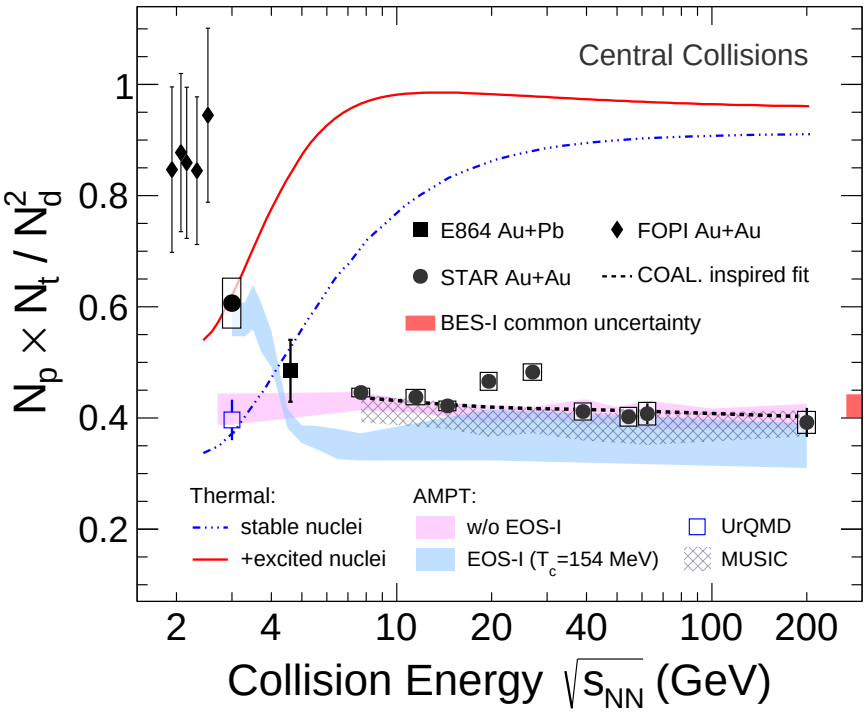

Figure 4.7.3: Energy dependence of the ratio $N_p \times N_t/N_d^2$ in most central 0-10% Au + Au collisions. Vertical lines and boxes represent statistical and systematic uncertainties. The experimental results come from the STAR (0-10%), E864 (0-10%), and FOPI (impact parameter $b_0 < 0.15$). The red band at the right side of the plot indicates the common uncertainty (∼4.2%) in the BES-I result. Colored bands denote the ratios from MUSIC and AMPT (w/o and w/ EOS-I) hybrid model calculations. The ratio from UrQMD model is shown by an open square. Dashed black lines are the coalescence baselines obtained from the coalescence-inspired fit [137]. Solid red and dotted blue lines represent thermal model results [131].

contributions from excited nuclear state decays or not, shows a monotonically increasing trend with increasing collision energies, eventually reaching a saturation at energies around a few tens of GeV. It was observed that the yield ratio at $\sqrt{s_{\rm NN}}$ = 3 GeV can be well described by the thermal model when incorporating the decays of excited nuclear states. Coalescence-based calculations of central Au+Au collisions at $\sqrt{s_{\rm NN}}$ = 3 GeV from UrQMD and AMPT models without considering the excited nuclear states decays show smaller values than the 3 GeV data. Furthermore, this yield ratio can be also reproduced by the AMPT model when employing a first-order phase transition. Those detailed comparisons between experimental data and various models calculations demonstrate that the production of light nuclei at mid-rapidity in Au+Au collisions at RHIC energies ($\sqrt{s_{\rm NN}}$ = 7.7 - 200 GeV) can be effectively explained by nucleon coalescence models. Additionally, it has been observed that the thermal model fails to describe the overall trend of the energy dependence of the yield ratios and the yields of light nuclei receive significant contributions from the decays of excited nuclear states at lower energies.

Chapter 5

Blast-Wave Model Fits

5.1 Blast-Wave Model

The Blast-Wave Model is a theoretical framework used to describe the collective motion of particles produced in high-energy heavy-ion collisions, especially in the context of relativistic heavy-ion physics. The model assumes that in the early stages of the collision the system can be described by hydrodynamics, in particular relativistic hydrodynamics. The blast wave is then used to model the evolution of the system from the initial state to the final freeze-out configuration, and thus to understand the properties of the hot and dense matter produced in the collision. Analogous to the blast wave produced by an explosion, the blast-wave model approximates the source of expanding particles as a fluid undergoing rapid explosive expansion. During the freeze-out stage of the collision process, the particles produced in the system cease to interact strongly and escape the system. The transverse momentum distributions of the different particles reflect the bulk properties of the matter at kinetic freeze-out, after elastic collisions have ceased [139]. and during the kinetic freeze-out stage, the particles enter an elastic collision phase in which their momentum information is not changed.

Let us briefly introduce the calculation details of traditional blast-wave model. Based on the principle of boost invariance, in order to achieve azimuthal symmetry, the transverse velocity field is first defined as

$$u'^{\nu}(\tilde{t}, r, z = 0) = (\cosh\rho, \vec{e}_T \sinh\rho, 0) \tag{5.1.1}$$

where using the boost angle (velocity profile) $\rho(r) = \tanh^{-1}\beta_T$. And boosting it in longitudinal

direction with boost angle η to obtain the entire velocity field [116, 140] expressed as

$$u^{\mu}(\rho,\eta) = (\cosh\rho\cosh\eta, \vec{e}_T \sinh\rho, \cosh\rho\sinh\eta) \tag{5.1.2}$$

where due to the Lorentz transformations in different directions is not commutative, u^{μ} is asymmetric with respect to boost angles ρ and η.

Based on the above definition, the invariant momentum spectrum can be given by

$$E\frac{d^3n}{d^3p} = \int_{\sigma} f(x,p)p^{\lambda}d\sigma_{\lambda} \approx \frac{g}{(2\pi)^3}\int e^{-(u^{\nu}p_{\nu}-\mu)/T}p^{\lambda}d\sigma_{\lambda} \tag{5.1.3}$$

where $f(x,p)$ is a Lorentz invariant distribution function and we assume that it is the Boltzmann distribution. Thus the $u^{\nu}p_{\nu}$ can be expressed by the momentum of the particle as

$$u^{\nu}p_{\nu} = m_T\cosh(y-\eta)\cosh\rho - p_T\sinh\rho\cos(\Phi-\phi) \tag{5.1.4}$$

Considering the azimuthal symmetry, we can integrate over $d\phi$ using the modified Bessel function $I_0(z) = (2\pi)^{-1}\int_0^{2\pi} e^{z\cos\phi}d\phi$. And assuming longitudinal invariance (Bjorken Flow), another modified Bessel function K_1 is an integral over dy, denoted as $K_1(z) = \int_0^{\infty}\cosh y e^{-z\cosh y}dy$.

Finally, the transverse momentum spectrum is represented as illustrated in Eq. (4.1.1). The parameters of the blast-wave model include the temperature and velocity profiles of the expanding system. It can be obtained by fitting the transverse momentum spectrum of the particle. This model has been applied to data from experiments at various particle colliders, such as the RHIC [128, 129] and the LHC [68, 141].

5.2 Kinetic Freeze-out Parameters

As we mentioned in Sec. 3.4.2, The kinetic freeze-out parameters such as kinetic freeze-out temperature T_{kin} and average radial flow velocity $\langle\beta_T\rangle$, are obtained by fitting the spectra with blast-wave model function. In the initial analysis, consistent with previous analyses, the blast-wave model is assumed to be the underlying boost-invariant longitudinal dynamics.

Based on the measured particles at 3 GeV, we fit the p_T spectra for the particles individually as shown in Fig. 5.2.1, there are spectra fit for $\pi^{\pm}$, $K^{\pm}$, K^0_s, p, d, t, ^{3}He, and ^{4}He. Only mid-rapidity ($-0.1 < y < 0$) and most central (0-10%) Au + Au collisions measured spectra are included. Blue solid lines represent the fitting range for each particles. As shown by the dotted line, the blast-wave model describes the spectra of all particles well.

The kinetic freeze-out temperature T_{kin} and velocity $\langle\beta_T\rangle$ obtained by those fits are shown

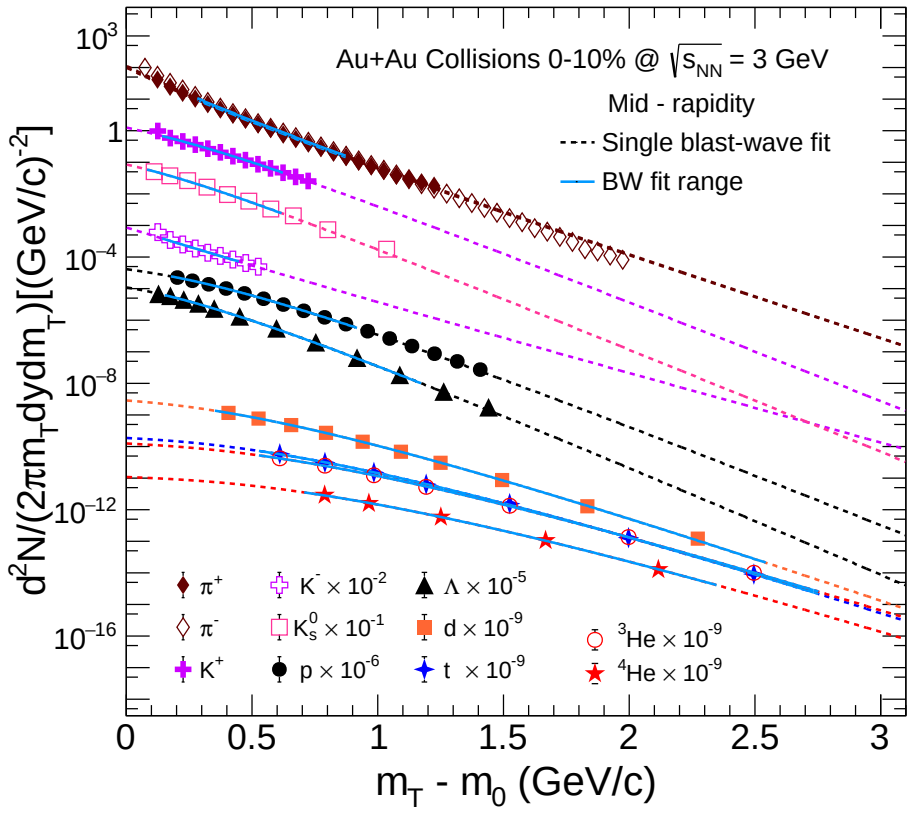

Figure 5.2.1: Blast-wave model fits of p_T spectra for $\pi^{\pm}$, $K^{\pm}$, K^0_s, p, d, t, ^{3}He, and ^{4}He individually at mid-rapidity ($-0.1 < y < 0$) in 0-10% central Au + Au collisions at $\sqrt{s_{NN}} =$ 3 GeV, different particle spectra are scaled by different factors. Colored dotted lines are fitting results by the blast-wave model. Blue solid lines represent the fitting range for each particle. Uncertainties on experimental data represent statistical and systematic uncertainties added in quadrature. The uncertainties are smaller than the symbol size.

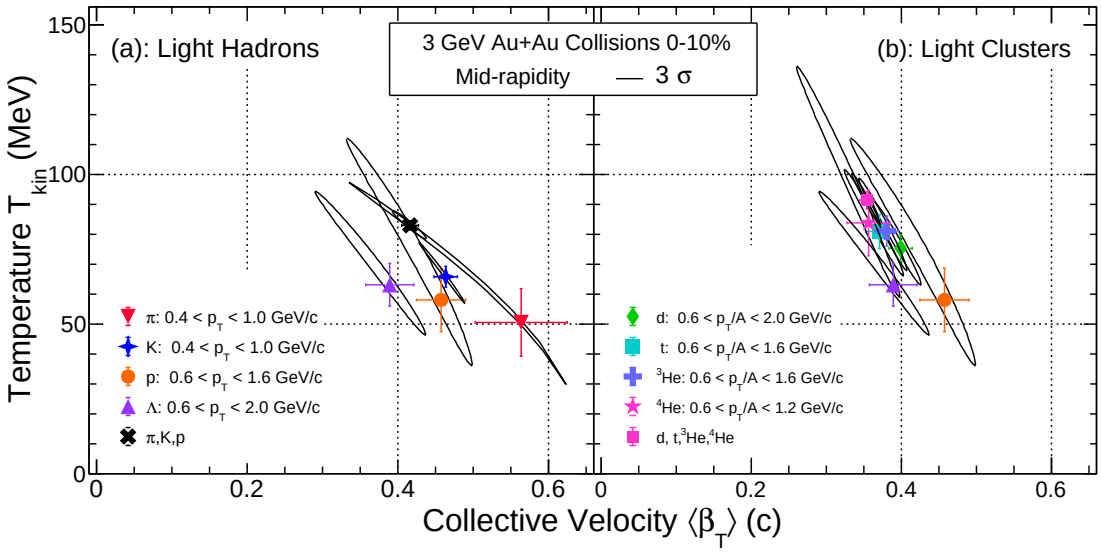

Figure 5.2.2: $T_{\rm kin}$ *vs.* $\langle\beta_T\rangle$ dependence of light hadrons (a) and light clusters (b) at mid-rapidity in 0-10% Au+Au collisions at $\sqrt{s_{\rm NN}} = 3\,{\rm GeV}$. (a) Parameters for $\pi^{\pm}$, $\rm K^{\pm}$ and $\rm K^0_s$, p, Λ, black marker represent the simultaneously fit parameter. (b) Parameters for p, Λ, d, t, ^{3}He, ^{4}He, pink square represent the light nuclei (d, t, ^{3}He, and ^{4}He) simultaneously fit result. Gray contour plots represent 3σ results. The vertical lines indicate 1σ fit uncertainties.

in Fig. 5.2.2, figure (a) shows the parameters obtained by fitting the light hadrons, considering the 3σ uncertainty as black contour shown, the particles $\pi^{\pm}$, $\rm K^{\pm}$, $\rm K^0_s$, and p can be fitted simultaneously, the black marker represents the simultaneous fit result. Figure (b) shows the parameters obtained by fitting the light nuclei, observed that their contours are close to each other. Based on the same consideration, a common set of parameters can be extracted by fitting light nuclei simultaneously, which is shown as a pink square in figure (b).

Figure 5.2.3 shows the p_T spectra of the above simultaneous blast-wave model fits, different colored markers represent different particles, and the dotted line of the corresponding color is fit for that particle. The T_{kin} of light hadrons (83.00 $\pm$1.56) is lower than light clusters (94.65 $\pm$2.05), while the $\langle\beta_T\rangle$ of light hadrons (0.42 $\pm$0.01) is higher than light clusters (0.35 $\pm$0.01). Here the uncertainties are only the 1σ of fit uncertainty. For the final uncertainty, we also consider the following source: The measured pions contain large contributions from resonance decays, those are not included in the default blast-wave model, so the effect on the extracted kinetic freeze-out parameters due to different p_T ranges used for fitting is estimated. The blast-wave parameters for different particle are different due to the mass difference, thus the systematic uncertainties are also assessed by excluding the $\rm K^{\pm}$ spectra or the p spectrum from the blast-wave fit in left figure, excluding the ^{4}He spectrum, the ^{3}He spectrum, the t, d, or p

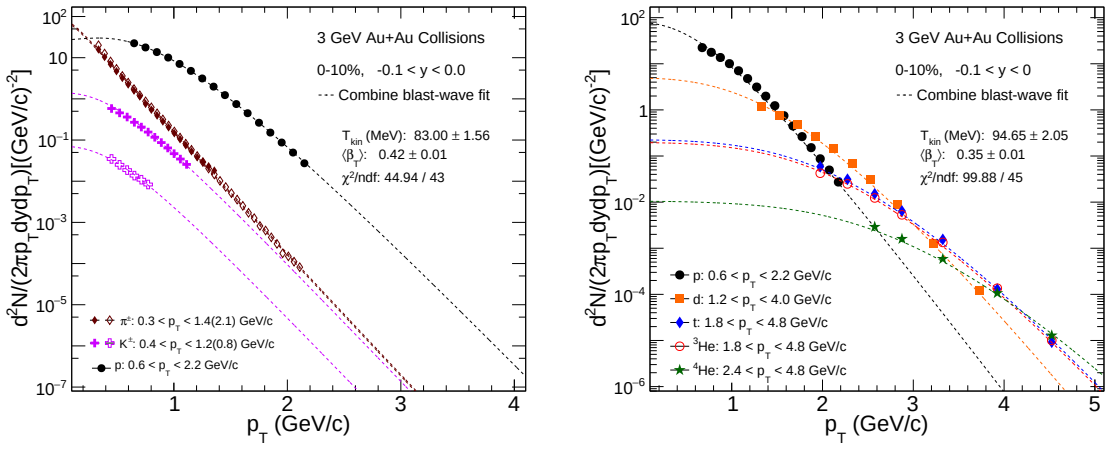

Figure 5.2.3: Blast-wave model fits of p_T spectra for (left) $\pi^{\pm}$, $K^{\pm}$, and p simultaneously, (right) p, d, t, ^{3}He, and ^{4}He simultaneously at mid-rapidity ($-0.1 < y < 0$) in 0-10% central Au + Au collisions at $\sqrt{s_{\rm NN}} = 3$ GeV. Uncertainties on experimental data represent statistical and systematic uncertainties added in quadrature. The uncertainties are smaller than the symbol size.

spectra from the blast-wave fit in right figure. The default fit for our simultaneously fit is done with fixing the velocity profile exponent n to unity. Considered the different form of the profile, the free n is used to estimite the parameter uncertainties. The final uncertainty presented in the Fig. 5.2.4 is quadrature sum of the above mentioned uncertainty sources.

Figure 5.2.4 shows $T_{\rm kin}$ *vs.* $\langle\beta_T\rangle$ dependence of protons and light nuclei. (a) plot shows the energy dependence in mid-rapidity from central to peripheral Au+Au collisions, where we fit the π, K and p spectra simultaneously at 3 GeV (black open triangle marker) and compared to the published results (gray markers) at 7.7, 19.6, and 200 GeV [128, 129], it is clearly observed that the freeze-out parameters ($T_{\rm kin}$, $\langle\beta_T\rangle$) at 3 GeV show a different trend compared to that of higher energy collisions, indicating a different equation of state (EoS). Even when we fit proton and deuteron individually as the red and blue markers show, the freeze-out parameter ($T_{\rm kin}$) of deuteron is systematically higher than that of the proton. From SMASH model (the color contour plots show proton and deuteron results in 0-10%), the similar trend is observed. Thus the hot and dense medium created in the 3 GeV collisions seems different from that of high energy collisions. Focus on 3 GeV, as (b) and (c) plots shown, where we fit the light nuclei (d, t, ^{3}He, and ^{4}He) simultaneously to get a common $T_{\rm kin}$ and $\langle\beta_T\rangle$. (b) shows mid-rapidity ($-0.1 < y < 0$) results in each centrality bins. The $T_{\rm kin}$ increases from central to peripheral collisions suggest the lifetime of fireball becomes shorter from central to peripheral

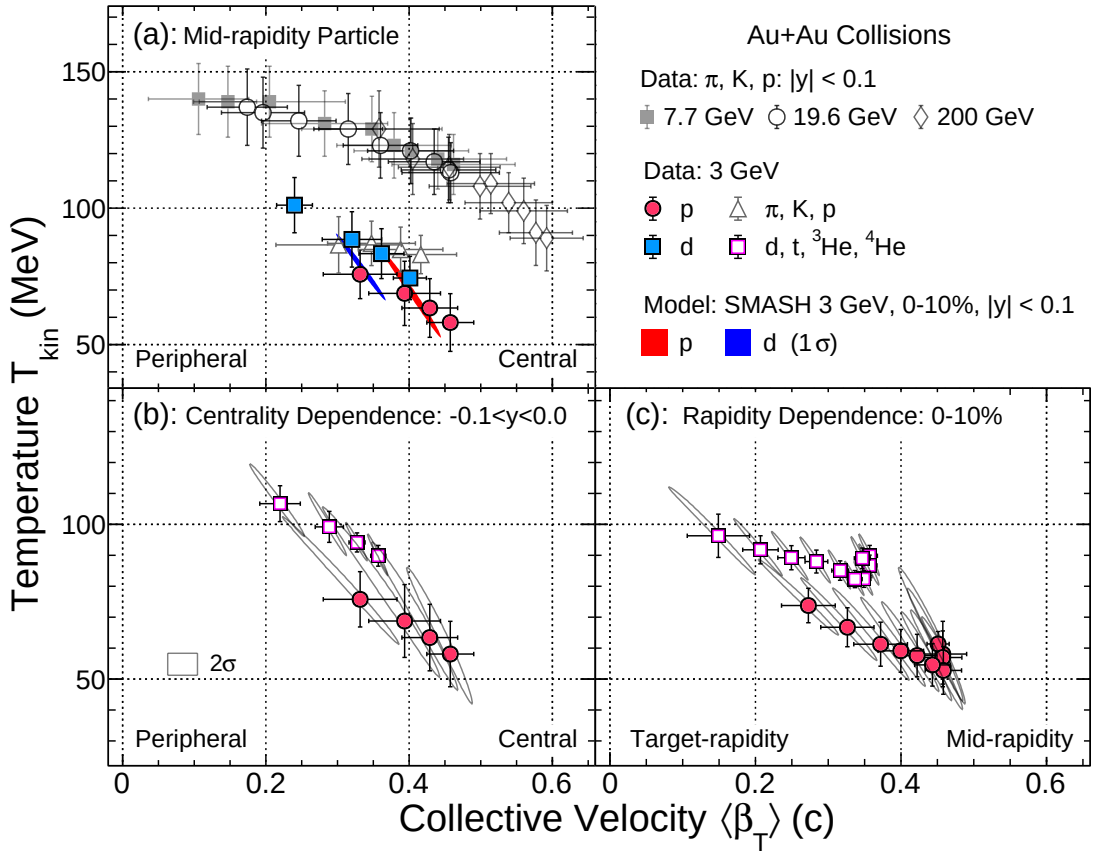

Figure 5.2.4: $T_{\rm kin}$ *vs.* $\langle\beta_T\rangle$ dependence of protons and light nuclei. (a) Energy dependence in mid-rapidity in Au+Au collisions from central to peripheral collisions. Black and gray markers are the result of fitting π, K, p spectra simultaneously. Red and blue markers represent individual fitting results for proton and deuteron, respectively. Color contours represent SMASH results at 3 GeV. (b) Centrality dependence in mid-rapidity ($-0.1 < y < 0$) at $\sqrt{s_{\rm NN}} = 3$ GeV. Square boxes indicate the results of fitting the light nuclei ($d, t,^3$ He, and ^{4}He) simultaneously, gray contour plots represent 2σ results. (c) Rapidity dependence at 0-10% centrality bin. The vertical lines indicate 1σ fit uncertainties.

collision. The $\langle\beta_T\rangle$ decrease from central to peripheral collisions suggest more rapid expansion in central collisions. (c) shows the rapidity dependence results at most central (0-10%) Au+Au collisions. The parameters have no obvious rapidity dependence in mid-rapidity regions, but the $T_{\rm kin}$ increases and the $\langle\beta_T\rangle$ decreases at target rapidity. The above differences tell us that there are different physical properties that need to be discussed.

5.3 Non-Boost-Invariant Blast-Wave Model

The main underlying assumption of the traditional blast-wave model mentioned above is the boost-invariant longitudinal dynamics, which assumes that the particles in the system produced by collisions are thermalize locally, and the system expands collectively with a common radial velocity field, experiencing an instantaneous collective freeze-out. At RHIC and LHC energies, stronger longitudinal flow may lead to a cylindrical geometry, hence this is a reasonable assumption. However, at lower collision energies, given the anisotropy of the transverse flow profile and the shape of the source in coordinate space, the longitudinal boost invariance does not hold. It is necessary to relax the boost invariance assumption, as proposed in Ref. [116, 142, 143], a non-boost-invariant extension of the blast-wave model that breaks the cylindrical symmetry by modifying the system boundary.

Providing a realistic parametrization of the freeze-out surface of the expanding fireball under experimental conditions, the model has been shown to provide accurate fits to the p_T and rapidity spectra of various hadrons produced in different collision scenarios. This includes Au+Au collisions at E_{lab} = 11.6 A GeV, as measured by E802, E877, and E891 Collaborations [144–146], as well as 2 A - 8 A GeV measured by E895 collaboration [147, 148] at AGS. The model also demonstrates a good fit for collisions at E_{lab} = 30.67 A and 69.56 A GeV ($\sqrt{s_{\rm NN}}$ = 7.7 and 11.5 GeV), as measured by the STAR collaboration [128] at RHIC, and for Pb+Pb collisions at E_{lab} = 20 A - 158 A GeV, as measured by NA49 collaboration [149–151] at SPS.

In this analysis, to account for the non-boost-invariance, the first modification is incorporate the rapidity distribution in longitudinal direction into the traditional blast-wave model. Based on the discussion of the full-space rapidity distribution of particles in Sec. 4.3, we implement the Gaussian distribution and the generalized Gaussian distribution into the blast-wave function, which is shown in the following

$$\frac{1}{2\pi m_T}\frac{d^2N}{dm_T dy} \propto \int_{-r}^{Y} G(y)dy \times \int_0^R rdrI_0\left(\frac{p_T\sinh(\rho)}{T}\right) \times \exp\left(\frac{-m_T\cosh(y)\cosh(\rho)}{T}\right) \tag{5.3.1}$$

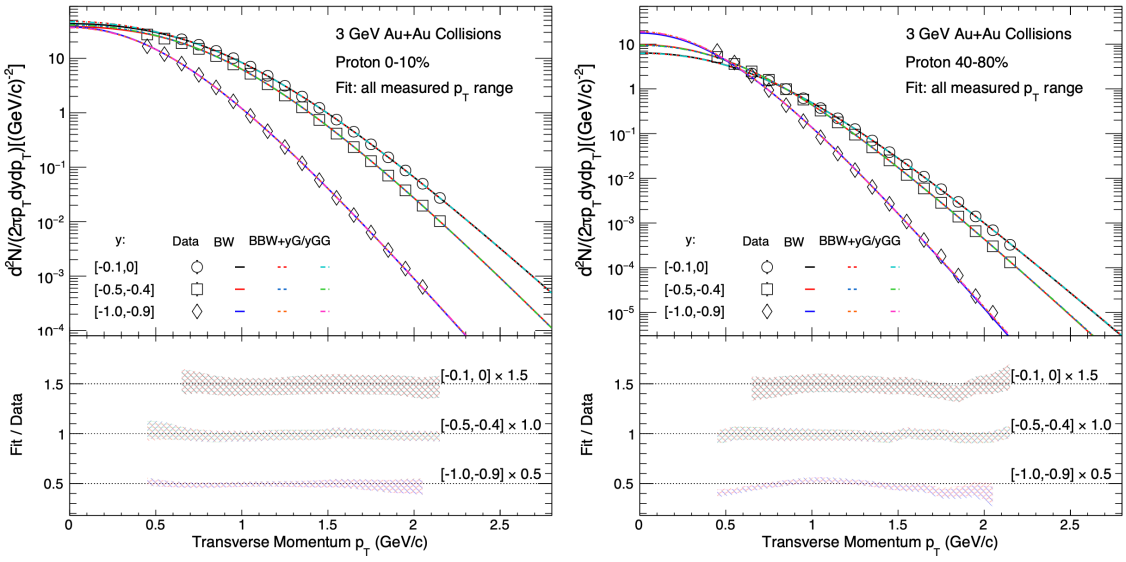

Figure 5.3.1: Transverse momentum spectra (p_T) of protons at 0-10% and 40-80% collisions. Colored dotted line shows the result of the modified blast-wave model. "BW" in the legend represents tranditional blast-wave model. "BBW+yG" represents Gaussian-blast-wave model, and "BBW+yGG" represents generalized Gaussian-blast-wave model.

and

$$\frac{1}{2\pi m_T}\frac{d^2N}{dm_T dy} \propto \int_{-r}^{Y} GG(y)dy \times \int_0^R rdrI_0\left(\frac{p_T \sinh(\rho)}{T}\right) \times \exp\left(\frac{-m_T \cosh(y)\cosh(\rho)}{T}\right) \tag{5.3.2}$$

where $G(y)$ and $GG(y)$ (as expressed by Eq. (3.4.3)) denote the Gaussian and generalized Gaussian distributions, respectively.

Figure 5.3.1 shows the traditional and modified blast-wave model results of the proton spectra, the colored solid line respects the fitting result of the traditional boost-invariant blast-wave model, the dotted line is fitted by the modified blast-wave model. Figure 5.3.2 shows the parameters (T_{kin} and $\langle\beta_T\rangle$) distribution, $\langle\beta_T\rangle$ for each fit is slightly smaller than the default results, and T_{kin} is almost identical. The parameters of the two rapidity distributions are the same.

To realize the non-boost-invariant blast-wave model, another consideration is: for an expanding fireball in local thermal equilibrium, the single-particle spectrum, in terms of transverse

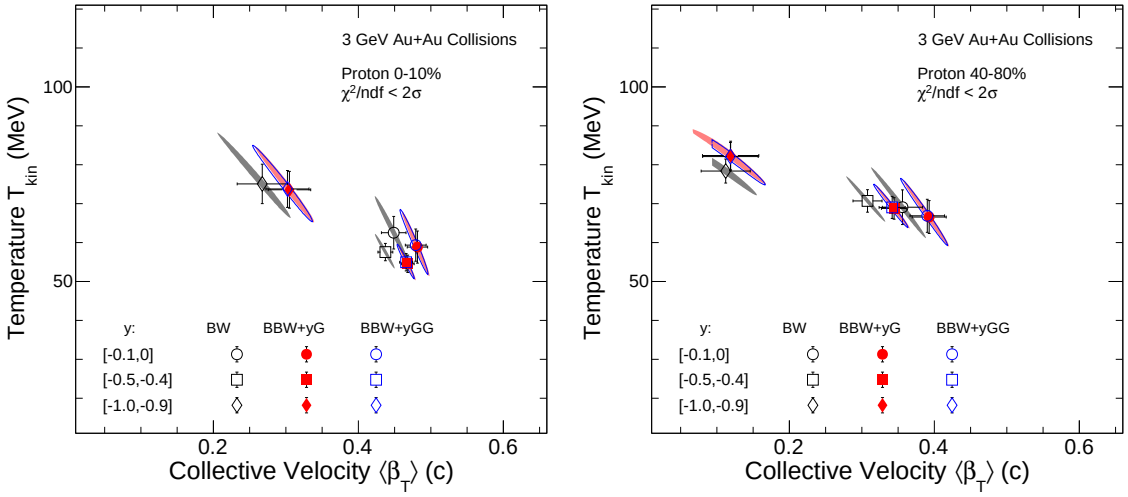

Figure 5.3.2: $T_{\rm kin}$ *vs.* $\langle\beta_T\rangle$ of protons at 0-10% and 40-80% collisions. The black open marker and gray contour show the mean value and 2σ contour of traditional boost-invariant blast-wave model, the red solid marker and blue open marker show the results for the modified blast-wave model.

mass m_T $\left(\equiv\sqrt{p_T^2+m^2}\right)$ and rapidity y, is defined as

$$\frac{dN}{m_T dm_T dy} \propto m_{\rm T}\int_{-\eta_{\rm max}}^{\eta_{\rm max}} d\eta\cosh(y-\eta) \times\int_0^{R(\eta)} rdrI_0\left(\frac{p_T\sinh(\rho)}{T}\right)\times\exp\left(\frac{-m_T\cosh(y-\eta)\cosh(\rho)}{T}\right) \tag{5.3.3}$$

where $\eta\equiv\tanh^{-1}(z/t)$ is the boost angle, denotes the space-time rapidity. Following the approach analyzed above, we use the same setup in order to break the longitudinal boost-invariance, and in the transverse direction boundary, considering the fireball with two choices, the first one is an elliptic shape of $R(\eta)$ given by

$$R(\eta)=R_0\sqrt{1-\frac{\eta^2}{\eta_{\rm max}^2}}, \tag{5.3.4}$$

where R_0 is the transverse size of the fireball at $\eta=0$. For a given $R_0=10$ and $\eta_{\rm max}=1.5$, the shape is shown in Fig. 5.3.3 left panel. The second one is Gaussian shape given by

$$R(\eta)=R_0\frac{1}{\sigma\sqrt{2\pi}}e^{-\frac{(\eta-\mu)^2}{2\sigma^2}} \tag{5.3.5}$$

where μ is the center value and σ is the width of the Gaussian distribution. For a given $R_0 = 10$, $\mu = 0$, and $\sigma = 1.045$, the shape is shown in Fig. 5.3.3 right panel.

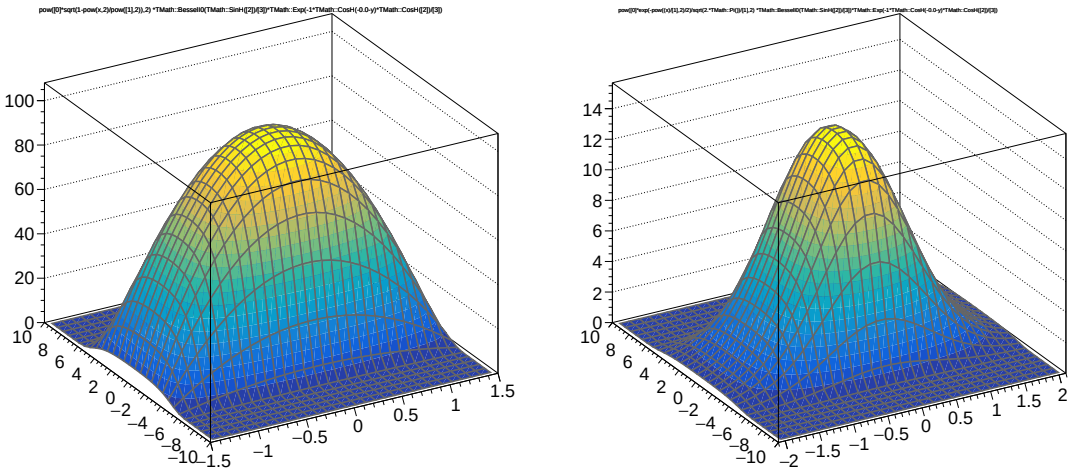

Figure 5.3.3: (left) Elliptic 2-dimensional distribution. (right) Gaussian 2-dimensional distribution.

Figure 5.3.4 shows the blast-wave model fitting results of the proton spectra, the colored solid line represents the fitting result of the boost-invariant blast-wave model, the dotted line is fitted by the non-boost-invariant blast-wave model. Comparison of the ratios of the fit and the data reveals that both models can better describe the p_T spectra.

The parameters (T_{kin} and $\langle\beta_T\rangle$) obtained from the non-boost-invariant blast-wave model are shown in Fig 5.3.5. At 0-10% Au + Au collisions, when we consider the distribution of fireballs, the average radial flow velocity $\langle\beta_T\rangle$ will become larger, especially at the target rapidity, but the temperature is essentially the same. At 40-80% collisions, we find that at mid-rapidity, the $\langle\beta_T\rangle$ obtained for Gaussian boundary is larger than the usual results, while the results for elliptic boundary are on the small side. In addition, there is a tendency for the temperature T_{kin} of the target rapidity to increase. But overall, the differences between the different fitted functions are very small.

We used the equation with elliptic shape to fit the light hadron (π, K, and p) p_T spectra simultaneously, and the results showed that the parameters (T_{kin} and $\langle\beta_T\rangle$) are consistent with traditional blast-wave model. $\eta_{\max}$ increases slightly from central ($\eta_{\max} = 1.32 \pm 0.17$) to peripheral collisions ($\eta_{\max} = 1.8 \pm 0.25$). The value of $\eta_{\max}$ obtained from light nuclei is consistent within the uncertainty with light hadron.

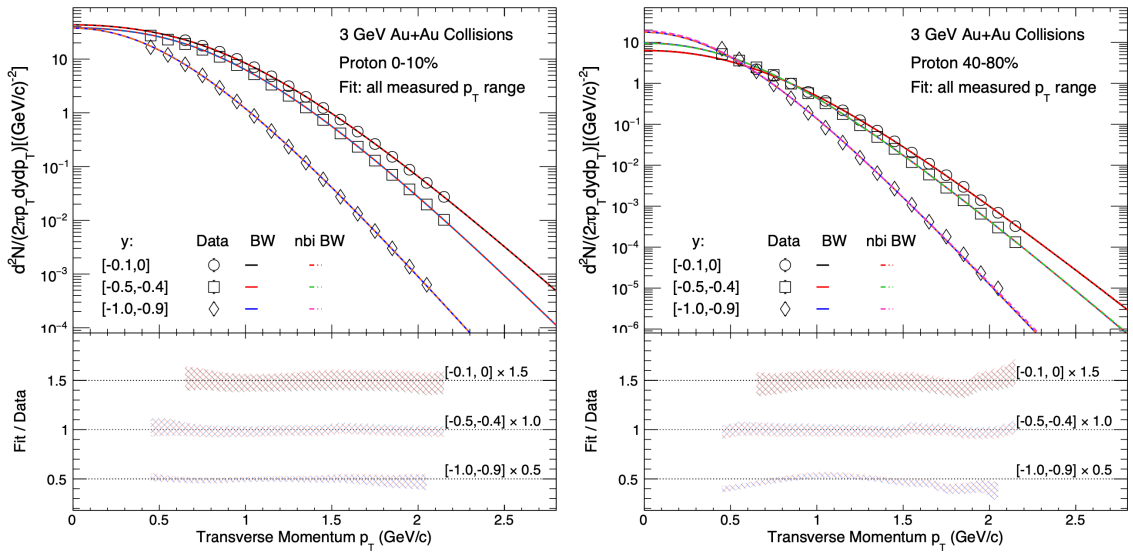

Figure 5.3.4: Transverse momentum spectra (p_T) of protons. Colored dotted line shows the result of the non-boost-invariant blast-wave model.

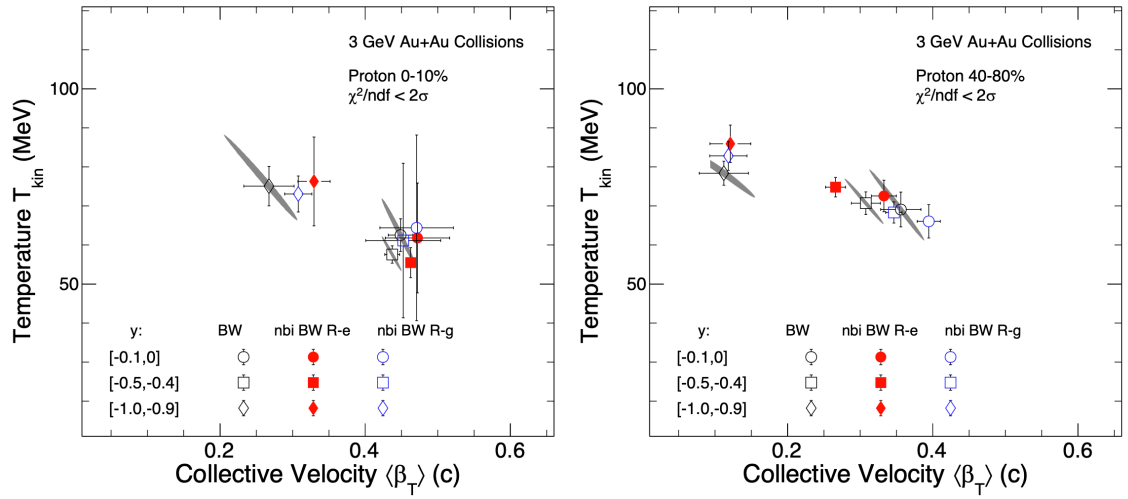

Figure 5.3.5: $T_{\rm kin}$ *vs.* $\langle\beta_T\rangle$ of protons. The black open marker and gray contour shows the mean value and 2σ contour of boost-invariant blast-wave model, the red solid marker and blue open marker show the results for the fireball with elliptical and Gaussian shape, respectively.

Chapter 6

Summary and Outlook

6.1 Summary

In summary, we report the comprehensive measurement of protons (p) and light nuclei (d, t, ^{3}He, and ^{4}He) production from middle to target rapidity in Au+Au collisions at $\sqrt{s_{\rm NN}}$ = 3 GeV by the STAR experiment, the data were collected in the fixed-target mode in 2018. The p_T spectra, dN/dy, $\langle p_T \rangle$, particle yield ratios (d/p, t/p,^{3}He/p, ^{4}He/p), and coalescence parameters (B_2, B_3) are presented as a function of rapidity and collision centrality. The 4π yields are extracted based on the measured rapidity distributions of dN/dy. It is observed that the mid-rapidity dN/dy of protons and light nuclei can be well described by the exponential dependence of the particle mass via the Boltzmann factor $e^{(m_N-\mu_B)/T}$ [43]. The penalty factor is about 6.1 $\pm$ 0.5 and 10.5 $\pm$ 0.8 for the most central and peripheral Au+Au collisions at $\sqrt{s_{\rm NN}}$ = 3 GeV, which are much lower than the results for high-energy collisions. The contributions from spectator fragmentations become more pronounced in peripheral collisions, especially at the target rapidity region.

The compound yield ratio $N_p \times N_t/N_d^2$ shows no centrality dependence for both mid-rapidity and target rapidity. Calculations of $N_p \times N_t/N_d^2$ from coalescence-based UrQMD and SMASH transport models show significant increasing trends from central to peripheral collisions, which fail to describe the experimental data [135, 137]. At this energy stage, the abundance of light nuclei production is also provided for the measurement of higher order compound yield ratios containing ^{3}He and ^{4}He. Furthermore, the increasing trend of the yield ratio $N_p \times N_t/N_d^2$ at energies below 4 GeV, which cannot be explained by thermal model or transport model calculations, suggests the presence of additional physics beyond the scope of these models. A recent AMPT calculation [136] incorporating a first-order phase transition

can reproduce this increasing trend at low energies. The systematic measurements of the production of protons and light nuclei at 3 GeV provide valuable insights into the production dynamics of light nuclei and our understanding of the QCD phase structure at high baryon density.

An intriguing finding that we have observed based on the blast-wave model is that the kinetic freeze-out parameters T_{kin} and $\langle\beta_T\rangle$ from $\sqrt{s_{\rm NN}} = 3$ GeV show a completely different trend compared to those from high energies. The T_{kin} ($\langle\beta_T\rangle$) of the d is systematically higher (lower) than that of the p. A similar trend is seen in the SMASH model calculation. All of the above implies that the hot and dense medium created in 3 GeV collisions may have a different equation of state (EoS) than that at high-energy collisions.

6.2 Outlook

6.2.1 Upgrades on STAR Detertor

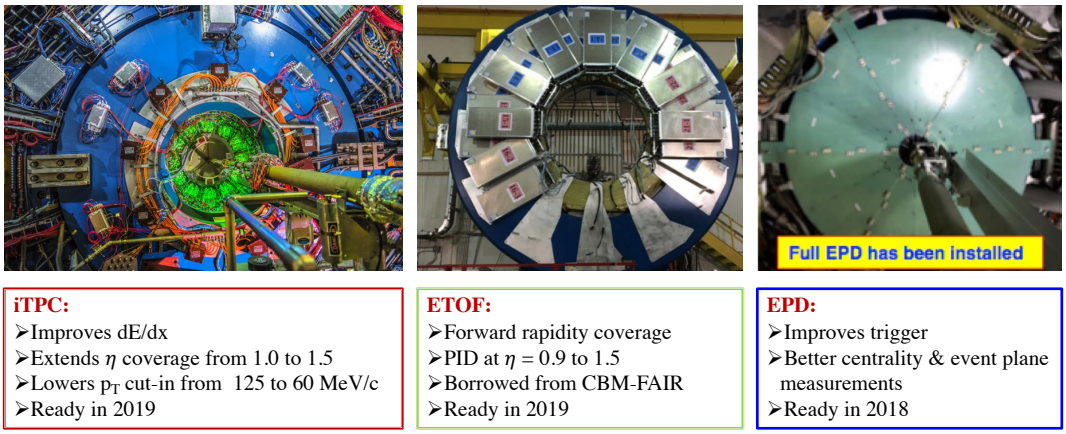

Figure 6.2.1: The BES-II upgrades on the STAR sub-detectors of iTPC, ETOF and EPD.

Since 2018, STAR has upgraded its three sub-detectors (Fig. 6.2.1), including inner TPC detector (iTPC), Endcap TOF detector (ETOF), and Event Plane Detector (EPD). The upgrade of iTPC enhances the dE/dx resolution, increases the η coverage up to 1.5, and also allows particle identification to reach a lower $p_T = 0.06$ GeV/c. The upgrade of ETOF increases the rapidity and η coverage, which will be described in more detail later. The upgrade of EPD is ready in 2018, it improves the trigger, and gives the better centrality and event plane measurements.

6.2.2 Endcap Time Of Flight Detector

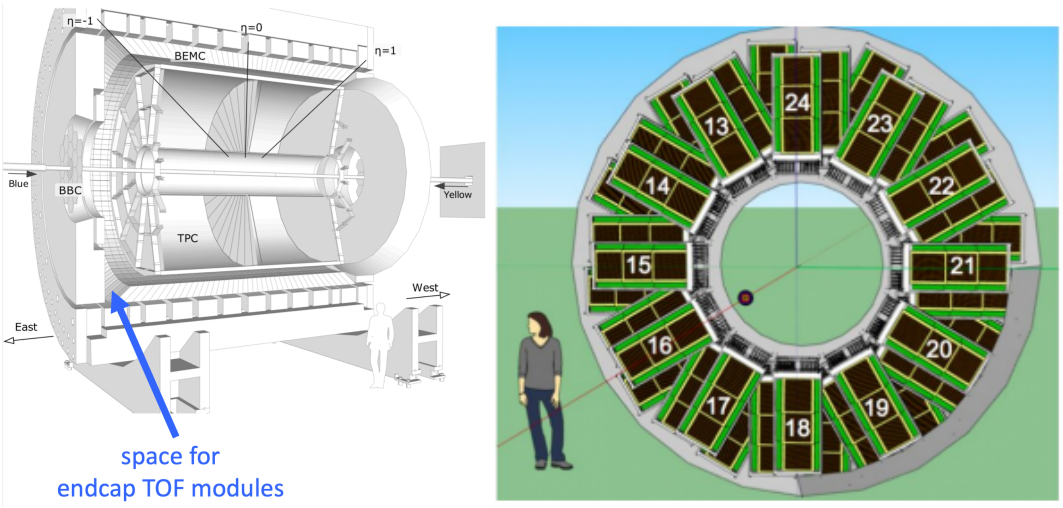

Figure 6.2.2: (left) The Endcap Time of Flight detectors with STAR detectors. (right) The modules structure of ETOF.

The BES-II of STAR covers the collision energy range from 3.0 to 19.6 GeV. Among them, in the collider mode part of the energy scan of 7.7-19.6 GeV, the PID rapidity coverage range is only 0.8. The fixed target procedure enables energy scan covering 3.0 to 7.7 GeV, however this procedure loses particle information in the mid-rapidity region. The endcap time-of-flight detector (ETOF) upgrade will provide particle identification (PID) to the main tracking chamber [99] over the extended pseudo-rapidity range provided by the iTPC upgrade [152], enabling precise studies of critical bulk property observables, which is essential for BES-II research.

The endcap time-of-flight detector (ETOF) is positioned at the endcap of the TOF detector as shown in Fig 6.2.2. It consists of 36 modules that use similar signal amplification techniques as the BTOF, however, the end-cap modules employ a modern, improved readout design. The ETOF upgrade will extend particle identification (PID) for pions, kaons, and protons to a rapidity of 1.2 in the collider mode part, and provide essential mid-rapidity PID for the 4.5 to 7.7 GeV portion of the scan in fixed-target mode.

ETOF was installed in 2018 as part of the STAR forward upgrade, and has been operating at BES-II since 2019. I test the acceptance of protons and light nuclei with the data of 9.2 GeV Au + Au collisions in the collider mode. Figure 6.2.3 shows the atomic mass number normalized transverse momentum p_T/A versus center-of-mass rapidity distribution for each particle. For protons, deuterons, tritons, and ^{3}He, the part of particle identification performed by ETOF is

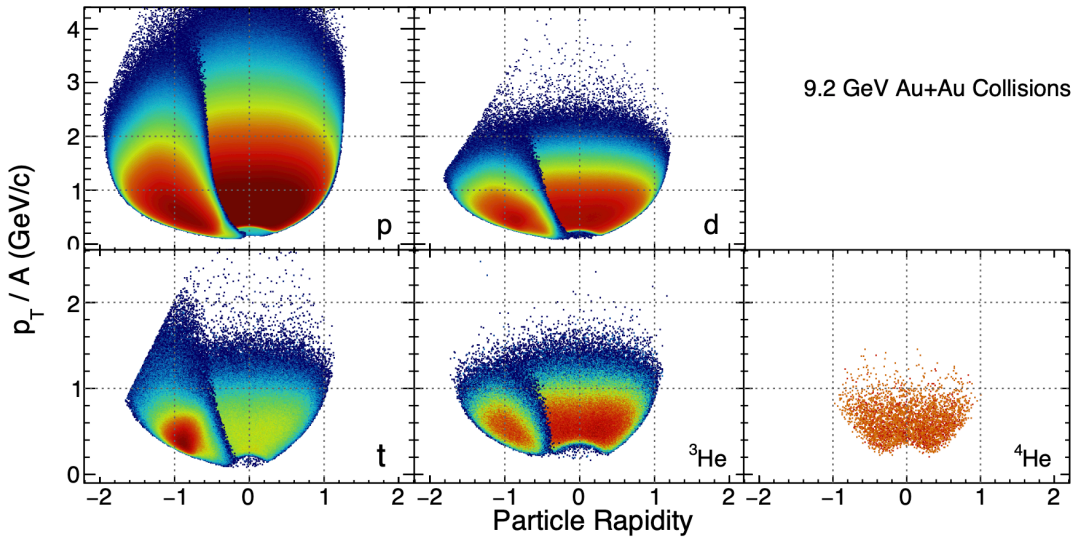

Figure 6.2.3: Atomic mass number normalized transverse momentum (p_T/A) versus rapidity distributions for identified protons, deuterons, tritons, ^{3}He, and ^{4}He. For each particle (except ^{4}He), the portion superimposed on the left part is identified by ETOF.

superimposed on the distribution of the corresponding particles. The statistics of ^{4}He are very small and cannot be detected by ETOF. This shows that in addition to the key observation quantities such as pion and kaon, ETOF also provides the possibility for more accurate research on light nuclei.

In data analysis, accurate calculation of efficiency cannot be ignored in order to obtain reliable results. The installation position of ETOF means that it has a special distribution of rapidity and pseudo-rapidity. Figure 6.2.4 shows the distribution of V_Z versus η of protons. Scanning V_Z and η respectively, we calculated the ETOF matching efficiency in different intervals as shown in the Fig 6.2.5. The left figure shows the efficiency as a function of momentum at $-1.5 < \eta < -1.4$. Compare the results for different V_Z ranges, it can be found that at this energy, the ETOF mattching efficiency reaches up to 60%. In addition, the efficiency of $V_Z < 0$ is generally higher than that of $V_Z > 0$. The right figure shows the efficiency as a function of momentum with $20 < V_Z < 40$ cm. In the range of $-1.7 < \eta < -1.3$, the efficiency is relatively stable. However, in the range of $\eta < -1.7$ and $\eta > -1.3$, the efficiency drops off a cliff, this is due to the inconsistent acceptance of ETOF and TPC within these η ranges. Thus in the future analyses, the calculation of ETOF matching efficiency requires careful estimation.

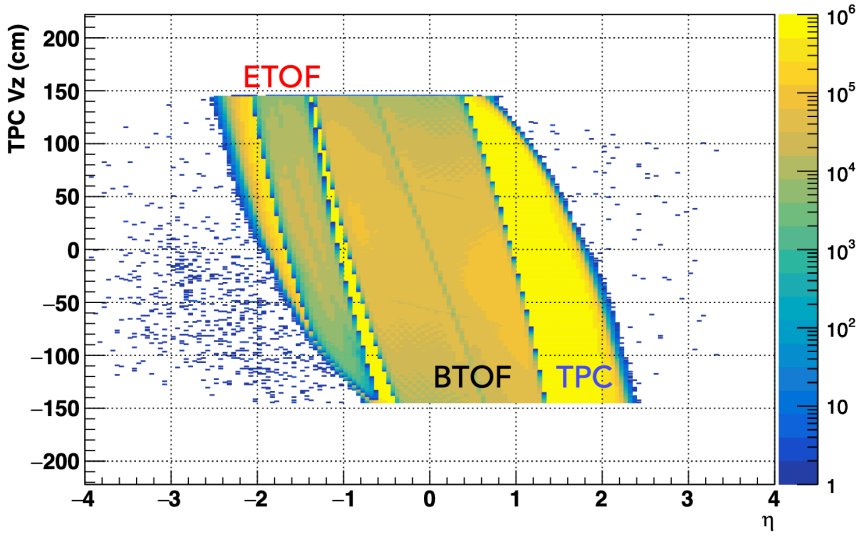

Figure 6.2.4: TPC vertex Z (V_Z) versus η distribution in Au + Au collisions at $\sqrt{s_{NN}}$ = 9.2 GeV with collider mode. The three color patches represent the parts identified by TPC, BTOF, and ETOF respectively.

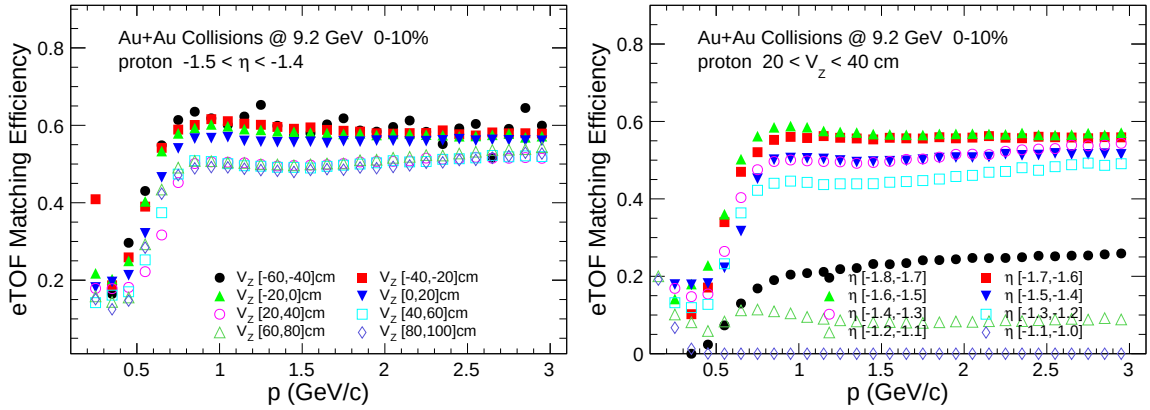

Figure 6.2.5: (left) The ETOF matching efficiency of particles at $-1.5 < \eta < -1.4$ in Au+Au collisions at $\sqrt{s_{NN}}$ = 9.2 GeV. Different colored markers indicate the results of different Vz cutoffs. (right) The ETOF matching efficiency of particles at $20 < V_Z < 40$ cm in Au+Au collisions at $\sqrt{s_{NN}}$ = 9.2 GeV. Different colored markers indicate the results of different η windows.

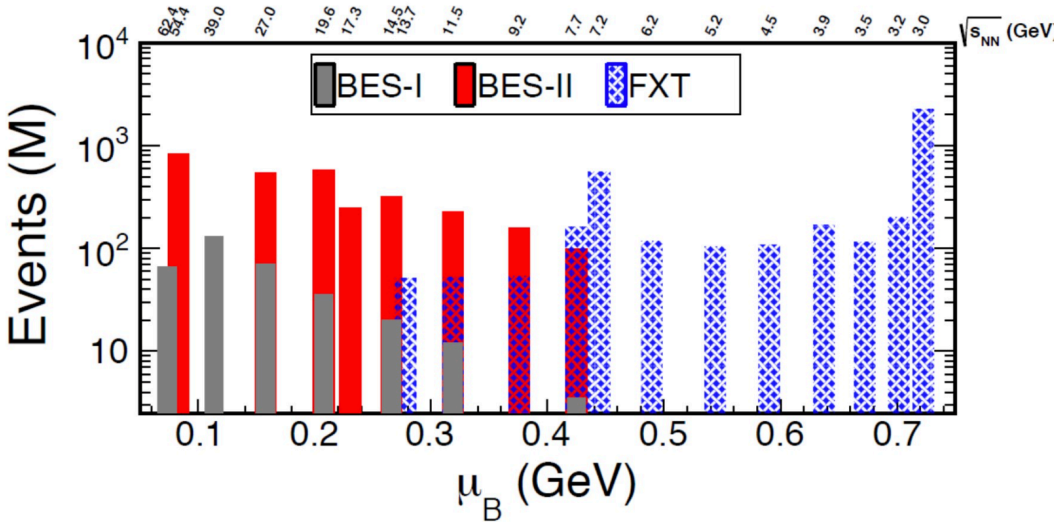

Figure 6.2.6: The number of events for the STAR beam energy scan program. The BES-I data sets are shown in gery bars. The BES-II data sets are shown in red bars. The FXT data sets are shown in blue grid bars.

6.2.3 Beam Energy Scan Program

With the upgrade of the STAR detector, high statistics data of Au+Au collisions have been collected from the BES-II and Fixed-Target programs, as shown in Fig. 6.2.6, those data have at least twice the statistics of BES-I and with more collision energies, which will greatly reduce the uncertainties in previous observations. It's worth noting that the 3 GeV data involved in this analysis, within the new dataset, see its statistics soar to 2 billion, which will greatly improve the accuracy of each observed quantity. The FXT program has an energy coverage of $\sqrt{s_{\rm NN}}$ = 3.0 - 13.7 GeV, which extends the baryon density potential μ_B up to 750 MeV. Therefore, with the upgrade of the STAR detector and the collection of these high-statistics data, more precise measurements and extensive physical studies at lower energies will follow in succession.

Bibliography

[1] https://texample.net/tikz/examples/model-physics/.

[2] Harald Fritzsch and Murray Gell-Mann. Current Algebra: Quarks and What Else? *eConf*, C720906V2:135–165, 1972.

[3] Maria Elena Tejeda-Yeomans. Heavy-Ion Physics: Freedom to do Hot, Dense, Exciting QCD. *CERN Yellow Rep. School Proc.*, 2:137, 2021.

[4] R. L. Workman et al. Review of Particle Physics. *PTEP*, 2022:083C01, 2022.

[5] Xiaofeng Luo, Shusu Shi, Nu Xu, and Yifei Zhang. A Study of the Properties of the QCD Phase Diagram in High-Energy Nuclear Collisions. *Particles*, 3(2):278–307, 2020.

[6] P. Danielewicz. Shock Waves In a Hydrodynamic Model of Central Heavy Ion Collisions. *Nucl. Phys. A*, 314:465–484, 1979.

[7] J. Pochodzalla et al. Probing the Nuclear Liquid - Gas Phase Transition. *Phys. Rev. Lett.*, 75:1040–1043, 1995.

[8] Yu-Gang Ma. Application of Information Theory in Nuclear Liquid Gas Phase Transition. *Phys. Rev. Lett.*, 83:3617–3620, 1999.

[9] B. Borderie and J. D. Frankland. Liquid–Gas Phase Transition in Nuclei. *Prog. Part. Nucl. Phys.*, 105:82–138, 2019.

[10] Y. Aoki, G. Endrodi, Z. Fodor, S. D. Katz, and K. K. Szabo. The Order of the Quantum Chromodynamics Transition Predicted by the Standard Model of Particle Physics. *Nature*, 443:675–678, 2006.

[11] A. Bazavov et al. The Chiral and Deconfinement Aspects of the QCD Transition. *Phys. Rev. D*, 85:054503, 2012.

[12] R. Bellwied, S. Borsanyi, Z. Fodor, J. Günther, S. D. Katz, C. Ratti, and K. K. Szabo. The QCD Phase Diagram From Analytic Continuation. *Phys. Lett. B*, 751:559–564, 2015.

[13] Szabolcs Borsanyi, Zoltan Fodor, Jana N. Guenther, Ruben Kara, Sandor D. Katz, Paolo Parotto, Attila Pasztor, Claudia Ratti, and Kalman K. Szabo. QCD Crossover at Finite Chemical Potential from Lattice Simulations. *Phys. Rev. Lett.*, 125(5):052001, 2020.

[14] Misha A. Stephanov, K. Rajagopal, and Edward V. Shuryak. Signatures of the Tricritical Point in QCD. *Phys. Rev. Lett.*, 81:4816–4819, 1998.

[15] Misha A. Stephanov, K. Rajagopal, and Edward V. Shuryak. Event-by-Event Fluctuations in Heavy Ion Collisions and the QCD Critical Point. *Phys. Rev. D*, 60:114028, 1999.

[16] S. Jeon and V. Koch. Fluctuations of Particle Ratios and the Abundance of Hadronic Resonances. *Phys. Rev. Lett.*, 83:5435–5438, 1999.

[17] Masayuki Asakawa, Ulrich W. Heinz, and Berndt Muller. Fluctuation Probes of Quark Deconfinement. *Phys. Rev. Lett.*, 85:2072–2075, 2000.

[18] V. Koch, A. Majumder, and J. Randrup. Baryon-Strangeness Correlations: A Diagnostic of Strongly Interacting Matter. *Phys. Rev. Lett.*, 95:182301, 2005.

[19] S. Ejiri, F. Karsch, and K. Redlich. Hadronic Fluctuations at the QCD Phase Transition. *Phys. Lett. B*, 633:275–282, 2006.

[20] Shinji Ejiri. Canonical Partition Function and Finite Density Phase Transition in Lattice QCD. *Phys. Rev. D*, 78:074507, 2008.

[21] https://u.osu.edu/vishnu/2014/08/06/sketch-of-relativistic-heavy-ion-collisions/.

[22] G. M. Ter-Akopian et al. Problems to be Clarified by Means of Radioactive ion Beams Provided by the Acculinna-2 Separator. In *8th International Symposium on Exotic Nuclei*, pages 380–389, 2017.

[23] Sourendu Gupta, Xiaofeng Luo, Bedangadas Mohanty, Hans Georg Ritter, and Nu Xu. Scale for the phase diagram of quantum chromodynamics. *Science*, 332(6037):1525–1528, 2011.

[24] Xiaofeng Luo and Nu Xu. Search for the QCD Critical Point with Fluctuations of Conserved Quantities in Relativistic Heavy-Ion Collisions at RHIC : An Overview. *Nucl. Sci. Tech.*, 28(8):112, 2017.

[25] J. Adam et al. Nonmonotonic Energy Dependence of Net-Proton Number Fluctuations. *Phys. Rev. Lett.*, 126(9):092301, 2021.

[26] Mohamed Abdallah et al. Cumulants and Correlation Functions of Net-Proton, Proton, and Antiproton Multiplicity Distributions in Au + Au Collisions at Energies Available at the BNL Relativistic Heavy Ion Collider. *Phys. Rev. C*, 104(2):024902, 2021.

[27] M. S. Abdallah et al. Measurements of Proton High Order Cumulants in $\sqrt{s_{\rm NN}} = 3$ GeV Au + Au Collisions and Implications for the QCD Critical Point. *Phys. Rev. Lett.*, 128(20):202303, 2022.

[28] Mohamed Abdallah et al. Higher-Order Cumulants and Correlation Functions of Proton Multiplicity Distributions in $\sqrt{s_{NN}}$ =3 GeV Au + Au Collisions at the RHIC STAR Experiment. *Phys. Rev. C*, 107(2):024908, 2023.

[29] P. J. Siemens and Joseph I. Kapusta. Evidence for a Soft Nuclear Matter Equation of State. *Phys. Rev. Lett.*, 43:1486–1489, 1979.

[30] L. P. Csernai and Joseph I. Kapusta. Entropy and Cluster Production in Nuclear Collisions. *Phys. Rept.*, 131:223–318, 1986.

[31] Pawel Danielewicz and Qiu-bao Pan. Blast of Light Fragments from Central Heavy Ion Collisions. *Phys. Rev. C*, 46:2002–2011, 1992.

[32] Akira Ono. Cluster Production within Antisymmetrized Molecular Dynamics. *EPJ Web Conf.*, 122:11001, 2016.

[33] Apiwit Kittiratpattana, Michael F. Wondrak, Medina Hamzic, Marcus Bleicher, Christoph Herold, and Ayut Limphirat. Deuteron and Antideuteron Coalescence in Heavy-Ion Collisions: Energy Dependence of the Formation Geometry. *Eur. Phys. J. A*, 56(10):274, 2020.

[34] Edward Shuryak and Juan M. Torres-Rincon. Light-Nuclei Production and Search for the QCD Critical Point. *Eur. Phys. J. A*, 56(9):241, 2020.

[35] S. Nagamiya, M. C. Lemaire, E. Moller, S. Schnetzer, G. Shapiro, H. Steiner, and I. Tanihata. Production of Pions and Light Fragments at Large Angles in High-Energy Nuclear Collisions. *Phys. Rev. C*, 24:971–1009, 1981.

[36] J. E. Finn et al. Nuclear Fragment Mass Yields From High-energy Proton - Nucleus Interactions. *Phys. Rev. Lett.*, 49:1321, 1982.

[37] W. Reisdorf et al. Systematics of Central Heavy Ion Collisions in the 1 A GeV Regime. *Nucl. Phys. A*, 848:366–427, 2010.

[38] J. Adamczewski-Musch et al. Directed, Elliptic, and Higher Order Flow Harmonics of Protons, Deuterons, and Tritons in Au + Au Collisions at $\sqrt{s_{NN}} = 2.4$ GeV. *Phys. Rev. Lett.*, 125:262301, 2020.

[39] J. Barrette et al. Production of Light Nuclei in Relativistic Heavy Ion Collisions. *Phys. Rev. C*, 50:1077–1084, 1994.

[40] M. J. Bennett et al. Light Nuclei Production in Relativistic Au + Nucleus Collisions. *Phys. Rev. C*, 58:1155–1164, 1998.

[41] L. Ahle et al. Proton and Deuteron Production in Au + Au Reactions at 11.6 A GeV/c. *Phys. Rev. C*, 60:064901, 1999.

[42] J. Barrette et al. Light Fragment Yields from Au + Au Collisions at 11.5 A GeV/c. *Phys. Rev. C*, 61:044906, 2000.

[43] T. A. Armstrong et al. Mass Dependence of Light Nucleus Production in Ultrarelativistic Heavy Ion Collisions. *Phys. Rev. Lett.*, 83:5431–5434, 1999.

[44] T. A. Armstrong et al. Measurements of Light Nuclei Production in 11.5 A GeV/c Au + Pb Heavy Ion Collisions. *Phys. Rev. C*, 61:064908, 2000.

[45] T. A. Armstrong et al. Anti-Deuteron Yield at the AGS and Coalescence Implications. *Phys. Rev. Lett.*, 85:2685–2688, 2000.

[46] S. Albergo et al. Light Nuclei Production in Heavy Ion Collisions at Relativistic Energies. *Phys. Rev. C*, 65:034907, 2002.

[47] Jehanne Simon-Gillo et al. Deuteron and Anti-Deuteron Production in CERN Experiment NA44. *Nucl. Phys. A*, 590:483C–486C, 1995.

[48] S. V. Afanasiev et al. Deuteron Production in Central Pb + Pb Collisions at 158 A GeV. *Phys. Lett. B*, 486:22–28, 2000.

[49] I. G. Bearden et al. Deuteron and Triton Production with High Energy Sulphur and Lead Beams. *Eur. Phys. J. C*, 23:237–247, 2002.

[50] R. Arsenescu et al. An Investigation of the Anti-Nuclei and Nuclei Production Mechanism in Pb + Pb Collisions at 158 A GeV. *New J. Phys.*, 5:150, 2003.

[51] T. Anticic et al. Energy and Centrality Dependence of Deuteron and Proton Production in Pb + Pb Collisions at Relativistic Energies. *Phys. Rev. C*, 69:024902, 2004.

[52] V. I. Kolesnikov. Anti-Nuclei and Nuclei Production in Pb + Pb Collisions at CERN SPS Energies. *J. Phys. Conf. Ser.*, 110:032010, 2008.

[53] T. Anticic et al. Antideuteron and Deuteron Production in Mid-Central Pb + Pb Collisions at 158 *A* GeV. *Phys. Rev. C*, 85:044913, 2012.

[54] C. Adler et al. Anti-Deuteron and Anti-He-3 Production in $\sqrt{s_{NN}}$ = 130 GeV Au + Au Collisions. *Phys. Rev. Lett.*, 87:262301, 2001. [Erratum: Phys.Rev.Lett. 87, 279902 (2001)].

[55] S. S. Adler et al. Deuteron and Antideuteron Production in Au + Au Collisions at $\sqrt{s_{NN}}$ = 200 GeV. *Phys. Rev. Lett.*, 94:122302, 2005.

[56] S. Afanasiev et al. Elliptic Flow for Phi Mesons and (Anti)Deuterons in Au + Au Collisions at $\sqrt{s_{NN}}$ = 200 GeV. *Phys. Rev. Lett.*, 99:052301, 2007.

[57] B. I. Abelev et al. Yields and Elliptic Flow of d(Anti-d) and He-3(Anti-He-3) in Au + Au Collisions at $\sqrt{s_{NN}}$ = 200 GeV. *arXiv: 0909.0566*, 9 2009.

[58] H. Agakishiev et al. Observation of the Antimatter Helium-4 Nucleus. *Nature*, 473:353, 2011. [Erratum: Nature 475, 412 (2011)].

[59] Jaroslav Adam et al. Beam Energy Dependence of (Anti-)Deuteron Production in Au + Au Collisions at the BNL Relativistic Heavy Ion Collider. *Phys. Rev. C*, 99(6):064905, 2019.

[60] J. Adam et al. Beam-Energy Dependence of the Directed Flow of Deuterons in Au + Au Collisions. *Phys. Rev. C*, 102(4):044906, 2020.

[61] M. S. Abdallah et al. Light Nuclei Collectivity from $\sqrt{s_{NN}}$ = 3 GeV Au + Au Collisions at RHIC. *Phys. Lett. B*, 827:136941, 2022.

[62] Muhammad Abdulhamid et al. Beam Energy Dependence of Triton Production and Yield Ratio ($N_t \times N_p/N_d^2$) in Au + Au Collisions at RHIC. *Phys. Rev. Lett.*, 130:202301, 2023.

[63] B. Alper et al. Large Angle Production of Stable Particles Heavier Than the Proton and a Search for Quarks at the Cern Intersecting Storage Rings. *Phys. Lett. B*, 46:265–268, 1973.

[64] S. Henning et al. Production of Deuterons and Anti-Deuterons in Proton Proton Collisions at the CERN ISR. *Lett. Nuovo Cim.*, 21:189, 1978.

[65] T. Alexopoulos et al. Cross-Sections for Deuterium, Tritium, and Helium Production in p + p Collisions at $\sqrt{s_{\rm NN}}$ = 1.8-TeV. *Phys. Rev. D*, 62:072004, 2000.

[66] A. Aktas et al. Measurement of Anti-Deuteron Photoproduction and a Search for Heavy Stable Charged Particles at HERA. *Eur. Phys. J. C*, 36:413–423, 2004.

[67] Jaroslav Adam et al. Precision Measurement of the Mass Difference between Light Nuclei and Anti-Nuclei with the ALICE Experiment at the LHC. *Nature Phys.*, 11(10):811–814, 2015.

[68] Jaroslav Adam et al. Production of Light Nuclei and Anti-Nuclei in pp and Pb + Pb Collisions at Energies Available at the CERN Large Hadron Collider. *Phys. Rev. C*, 93(2):024917, 2016.

[69] Shreyasi Acharya et al. Measurement of Deuteron Spectra and Elliptic Flow in Pb + Pb Collisions at $\sqrt{s_{\rm NN}} = 2.76$ TeV at the LHC. *Eur. Phys. J. C*, 77(10):658, 2017.

[70] Shreyasi Acharya et al. Production of Deuterons, Tritons, ^{3}He Nuclei and Their Antinuclei in pp Collisions at $\sqrt{s} = 0.9$, 2.76 and 7 TeV. *Phys. Rev. C*, 97(2):024615, 2018.

[71] Shreyasi Acharya et al. Multiplicity Dependence of Light (Anti-)Nuclei Production in p + Pb Collisions at $\sqrt{s_{\rm NN}} = 5.02$ TeV. *Phys. Lett. B*, 800:135043, 2020.

[72] S. Acharya et al. (Anti-)Deuteron Production in p + p Collisions at $\sqrt{s} = 13$ TeV. *Eur. Phys. J. C*, 80(9):889, 2020.

[73] Shreyasi Acharya et al. Light (Anti)Nuclei Production in Pb + Pb Collisions at $\sqrt{s_{NN}}$ = 5.02 TeV. *Phys. Rev. C*, 107(6):064904, 2023.

[74] Joseph I. Kapusta. Mechanisms for Deuteron Production in Relativistic Nuclear Collisions. *Phys. Rev. C*, 21:1301–1310, 1980.

[75] H. Sato and K. Yazaki. On the Coalescence Model for High-Energy Nuclear Reactions. *Phys. Lett. B*, 98:153–157, 1981.

[76] S. Mrowczynski. Deuteron Formation Mechanism. *J. Phys. G*, 13(9):1089–1097, 1987.

[77] Stanislaw Mrowczynski. Anti-Deuteron Production and the Size of the Interaction Zone. *Phys. Lett. B*, 248:459–463, 1990.

[78] Carl B. Dover, Ulrich W. Heinz, Ekkard Schnedermann, and Joszef Zimanyi. Relativistic Coalescence Model for High-Energy Nuclear Collisions. *Phys. Rev. C*, 44:1636–1654, 1991.

[79] Rudiger Scheibl and Ulrich W. Heinz. Coalescence and Flow in Ultrarelativistic Heavy Ion Collisions. *Phys. Rev. C*, 59:1585–1602, 1999.

[80] Yongseok Oh, Zi-Wei Lin, and Che Ming Ko. Deuteron Production and Elliptic Flow in Relativistic Heavy Ion Collisions. *Phys. Rev. C*, 80:064902, 2009.

[81] J. Steinheimer, K. Gudima, A. Botvina, I. Mishustin, M. Bleicher, and H. Stocker. Hypernuclei, Dibaryon and Antinuclei Production in High Energy Heavy Ion Collisions: Thermal Production versus Coalescence. *Phys. Lett. B*, 714:85–91, 2012.

[82] N. Shah, Y. G. Ma, J. H. Chen, and S. Zhang. Production of Multistrange Hadrons, Light Nuclei and Hypertriton in Central Au + Au Collisions at $\sqrt{s_{NN}} = 11.5$ and 200 GeV. *Phys. Lett. B*, 754:6–10, 2016.

[83] Francesca Bellini and Alexander Philipp Kalweit. Testing Production Scenarios for (Anti-)(Hyper-)Nuclei and Exotica at Energies Available at the CERN Large Hadron Collider. *Phys. Rev. C*, 99(5):054905, 2019.

[84] A. Andronic, P. Braun-Munzinger, J. Stachel, and H. Stocker. Production of Light Nuclei, Hypernuclei and Their Antiparticles in Relativistic Nuclear Collisions. *Phys. Lett. B*, 697:203–207, 2011.

[85] J. Cleymans, S. Kabana, I. Kraus, H. Oeschler, K. Redlich, and N. Sharma. Antimatter Production in Proton-Proton and Heavy Ion Collisions at Ultrarelativistic Energies. *Phys. Rev. C*, 84:054916, 2011.

[86] Anton Andronic, Peter Braun-Munzinger, Krzysztof Redlich, and Johanna Stachel. Decoding the Phase Structure of QCD via Particle Production at High Energy. *Nature*, 561(7723):321–330, 2018.

[87] Benjamin Dönigus. Light Nuclei in the Hadron Resonance Gas. *Int. J. Mod. Phys. E*, 29(05):2040001, 2020.

[88] Lie-Wen Chen, Che Ming Ko, and Bao-An Li. Light Clusters Production as a Probe to the Nuclear Symmetry Energy. *Phys. Rev. C*, 68:017601, 2003.

[89] R. Bond, P. J. Johansen, S. E. Koonin, and S. Garpman. Breakup Densities of Nuclear Fireballs. *Phys. Lett. B*, 71:43–47, 1977.

[90] Edward Shuryak and Juan M. Torres-Rincon. Baryon Preclustering at the Freeze-out of Heavy Ion Collisions and Light Nuclei Production. *Phys. Rev. C*, 101(3):034914, 2020.

[91] A. Andronic, P. Braun-Munzinger, and J. Stachel. Hadron Production in Central Nucleus-Nucleus Collisions at Chemical Freeze-out. *Nucl. Phys. A*, 772:167–199, 2006.

[92] Peter Braun-Munzinger and Benjamin Dönigus. Loosely-Bound Objects Produced in Nuclear Collisions at the LHC. *Nucl. Phys. A*, 987:144–201, 2019.

[93] Kai-Jia Sun, Lie-Wen Chen, Che Ming Ko, and Zhangbu Xu. Probing QCD Critical Fluctuations from Light Nuclei Production in Relativistic Heavy Ion Collisions. *Phys. Lett. B*, 774:103–107, 2017.

[94] Kai-Jia Sun, Lie-Wen Chen, Che Ming Ko, Jie Pu, and Zhangbu Xu. Light Nuclei Production as a Probe of the QCD Phase Diagram. *Phys. Lett. B*, 781:499–504, 2018.

[95] https://www.bnl.gov/newsroom/news.php?a=119262.

[96] https://www.bnl.gov/rhic/complex.php.

[97] Ferdinand Willeke. Electron Ion Collider Conceptual Design Report 2021. 2 2021.

[98] https://www.bnl.gov/rhic/images.php.

[99] M. Anderson et al. The Star Time Projection Chamber: A Unique Tool for Studying High Multiplicity Events at RHIC. *Nucl. Instrum. Meth. A*, 499:659–678, 2003.

[100] Xin Dong. *Single Electron Transverse Momentum and Azimuthal Anisotropy Distributions: Charm Hadron Production at RHIC*. PhD thesis, Hefei, CUST, 2005.

[101] W. J. Llope. The Large-Area Time-of-Flight Upgrade for STAR. *Nucl. Instrum. Meth. B*, 241:306–310, 2005.

[102] https://drupal.star.bnl.gov/STAR/system/files/tof-5-24-2004.pdf.

[103] Kathryn C. Meehan. The Fixed-Target Experiment at STAR. *J. Phys. Conf. Ser.*, 742(1):012022, 2016.

[104] J. Adam et al. Flow and Interferometry Results from Au + Au Collisions at $\sqrt{s_{NN}} = 4.5$ GeV. *Phys. Rev. C*, 103(3):034908, 2021.

[105] F. S. Bieser et al. The STAR Trigger. *Nucl. Instrum. Meth. A*, 499:766–777, 2003.

[106] W. J. Llope. Multigap RPCs in the STAR Experiment at RHIC. *Nucl. Instrum. Meth. A*, 661:S110–S113, 2012.

[107] M. Shao, Olga Yu. Barannikova, X. Dong, Y. Fisyak, L. Ruan, P. Sorensen, and Z. Xu. Extensive Particle Identification with TPC and TOF at the STAR Experiment. *Nucl. Instrum. Meth. A*, 558:419–429, 2006.

[108] https://drupal.star.bnl.gov/STAR/starnotes/private/PSN0806.

[109] C. Adler et al. Measurement of Inclusive Anti-Protons from Au + Au Collisions at $\sqrt{s_{NN}}$ = 130 GeV. *Phys. Rev. Lett.*, 87:262302, 2001.

[110] Jaroslav Adam et al. Strange Hadron Production in Au + Au Collisions at $\sqrt{s_{\rm NN}}$ = 7.7, 11.5, 19.6, 27, and 39 GeV. *Phys. Rev. C*, 102(3):034909, 2020.

[111] K. Adcox et al. Measurement of the Lambda and Anti-Lambda Particles in Au + Au Collisions at $\sqrt{s_{NN}}$ = 130 GeV. *Phys. Rev. Lett.*, 89:092302, 2002.

[112] T. Anticic et al. Centrality Dependence of Proton and Antiproton Spectra in Pb + Pb Collisions at 40 A GeV and 158 A GeV Measured at the CERN SPS. *Phys. Rev. C*, 83:014901, 2011.

[113] Dmytro Oliinychenko, Chun Shen, and Volker Koch. Deuteron Production in Au + Au Collisions at $\sqrt{s_{NN}}$ = 7–200 GeV via Pion Catalysis. *Phys. Rev. C*, 103(3):034913, 2021.

[114] M. S. Abdallah et al. Probing Strangeness Canonical Ensemble with K−, ϕ(1020) and Ξ− Production in Au + Au Collisions at $\sqrt{s_{NN}}$ = 3 GeV. *Phys. Lett. B*, 831:137152, 2022.

[115] Gao-Chan Yong, Bao-An Li, Zhi-Gang Xiao, and Zi-Wei Lin. Probing the High-Density Nuclear Symmetry Energy with the Ξ−/Ξ0 Ratio in Heavy-Ion Collisions at $\sqrt{s_{NN}}\approx$3 GeV. *Phys. Rev. C*, 106(2):024902, 2022.

[116] Ekkard Schnedermann, Josef Sollfrank, and Ulrich W. Heinz. Thermal Phenomenology of Hadrons from 200 A GeV S + S Collisions. *Phys. Rev. C*, 48:2462–2475, 1993.

[117] P. Moulin and Juan Liu. Analysis of multiresolution image denoising schemes using generalized gaussian and complexity priors. *IEEE Transactions on Information Theory*, 45(3):909–919, 1999.

[118] Geert Verdoolaege and Paul Scheunders. Geodesics on the Manifold of Multivariate Generalized Gaussian Distributions with an Application to Multicomponent Texture Discrimination. *International Journal of Computer Vision*, 95(3):265–286, 2011.

[119] Geert Verdoolaege and Paul Scheunders. On the geometry of multivariate generalized gaussian models. *Journal of Mathematical Imaging and Vision*, 43(3):180–193, 2012.

[120] J. P. Bondorf, A. S. Botvina, A. S. Ilinov, I. N. Mishustin, and K. Sneppen. Statistical Multifragmentation of Nuclei. *Phys. Rept.*, 257:133–221, 1995.

[121] Wenbin Zhao, Lilin Zhu, Hua Zheng, Che Ming Ko, and Huichao Song. Spectra and Flow of Light Nuclei in Relativistic Heavy Ion Collisions at Energies Available at the BNL Relativistic Heavy Ion Collider and at the CERN Large Hadron Collider. *Phys. Rev. C*, 98(5):054905, 2018.

[122] Susanne Gläßel, Viktar Kireyeu, Vadim Voronyuk, Jörg Aichelin, Christoph Blume, Elena Bratkovskaya, Gabriele Coci, Vadim Kolesnikov, and Michael Winn. Cluster and Hypercluster Production in Relativistic Heavy Ion Collisions within the Parton-Hadron-Quantum-Molecular-Dynamics Approach. *Phys. Rev. C*, 105(1):014908, 2022.

[123] Elena Bratkovskaya, Susanne Glässel, Viktar Kireyeu, Jörg Aichelin, Marcus Bleicher, Christoph Blume, Gabriele Coci, Vadim Kolesnikov, Jan Steinheimer, and Vadim Voronyuk. Midrapidity Cluster Formation in Heavy Ion Collisions. *EPJ Web Conf.*, 276:03005, 2023.

[124] S. Das Gupta and A. Z. Mekjian. The Thermodynamic Model for Relativistic Heavy Ion Collisions. *Phys. Rept.*, 72:131–183, 1981.

[125] P. Braun-Munzinger and J. Stachel. Production of Strange Clusters and Strange Matter in Nucleus-Nucleus Collisions at the AGS. *J. Phys. G*, 21:L17–L20, 1995.

[126] J. L. Nagle, B. S. Kumar, D. Kusnezov, H. Sorge, and R. Mattiello. Coalescence of Deuterons in Relativistic Heavy Ion Collisions. *Phys. Rev. C*, 53:367–376, 1996.

[127] T. Anticic et al. Production of Deuterium, Tritium, and He3 in Central Pb + Pb Collisions at 20 A, 30 A, 40 A, 80 A , and 158 A GeV at the CERN Super Proton Synchrotron. *Phys. Rev. C*, 94(4):044906, 2016.

[128] L. Adamczyk et al. Bulk Properties of the Medium Produced in Relativistic Heavy-Ion Collisions from the Beam Energy Scan Program. *Phys. Rev. C*, 96(4):044904, 2017.

[129] B. I. Abelev et al. Systematic Measurements of Identified Particle Spectra in pp, d^+ Au and Au + Au Collisions from STAR. *Phys. Rev. C*, 79:034909, 2009.

[130] V. Vovchenko, V. V. Begun, and M. I. Gorenstein. Hadron Multiplicities and Chemical Freeze-out Conditions in Proton-Proton and Nucleus-Nucleus Collisions. *Phys. Rev. C*, 93(6):064906, 2016.

[131] Volodymyr Vovchenko, Benjamin Dönigus, Behruz Kardan, Manuel Lorenz, and Horst Stoecker. Feeddown Contributions from Unstable Nuclei in Relativistic Heavy Ion Collisions. *Phys. Lett.*, B:135746, 2020.

[132] S. T. Butler and C. A. Pearson. Deuterons from High-Energy Proton Bombardment of Matter. *Phys. Rev.*, 129:836–842, 1963.

[133] Ning Yu, Dingwei Zhang, and Xiaofeng Luo. Search for QCD Critical Point by Transverse Velocity Dependence of Anti-Deuteron to Deuteron Ratio. *Chin. Phys. C*, 44(1):014002, 2020.

[134] Alberto Polleri, Jakob P. Bondorf, and Igor N. Mishustin. Effects of Collective Expansion on Light Cluster Spectra in Relativistic Heavy Ion Collisions. *Phys. Lett. B*, 419:19–24, 1998.

[135] Wenbin Zhao, Kai-jia Sun, Che Ming Ko, and Xiaofeng Luo. Multiplicity Scaling of Light Nuclei Production in Relativistic Heavy Ion Collisions. *Phys. Lett. B*, 820:136571, 2021.

[136] Kai-Jia Sun, Wen-Hao Zhou, Lie-Wen Chen, Che Ming Ko, Feng Li, Rui Wang, and Jun Xu. Spinodal Enhancement of Light Nuclei Yield Ratio in Relativistic Heavy Ion Collisions. *arXiv: 2205.11010*, 5 2022.

[137] Kai-Jia Sun, Che Ming Ko, and Benjamin Dönigus. Suppression of Light Nuclei Production in Collisions of Small Systems at the Large Hadron Collider. *Phys. Lett. B*, 792:132–137, 2019.

[138] G. Ropke. Light Nuclei Quasiparticle Energy Shift in Hot and Dense Nuclear Matter. *Phys. Rev. C*, 79:014002, 2009.

[139] John Adams et al. Experimental and Theoretical Challenges in the Search for the Quark Gluon Plasma: The STAR Collaboration's Critical Assessment of the Evidence from RHIC Collisions. *Nucl. Phys. A*, 757:102–183, 2005.

[140] P. V. Ruuskanen. Transverse Hydrodynamics With a First Order Phase Transition in Very High-energy Nuclear Collisions. *Acta Phys. Polon. B*, 18:551, 1987.

[141] Betty Abelev et al. Centrality Dependence of π, K, p Production in Pb + Pb Collisions at $\sqrt{s_{NN}} = 2.76$ TeV. *Phys. Rev. C*, 88:044910, 2013.

[142] Harald Dobler, Josef Sollfrank, and Ulrich W. Heinz. Kinetic Freezeout and Radial Flow in 11.6 GeV/A Au + Au Collisions. *Phys. Lett. B*, 457:353–358, 1999.

[143] Sudhir Pandurang Rode, Partha Pratim Bhaduri, Amaresh Jaiswal, and Ankhi Roy. Kinetic Freeze-out Conditions in Nuclear Collisions with $2A$ - $158A$ GeV Beam Energy within a Non-Boost-Invariant Blast-Wave Model. *Phys. Rev. C*, 98(2):024907, 2018.

[144] L. Ahle et al. Simultaneous Multiplicity and Forward Energy Characterization of Particle Spectra in Au + Au Collisions at 11.6 A GeV/c. *Phys. Rev. C*, 59:2173–2188, 1999.

[145] Roger Lacasse et al. Hadron Yields and Spectra in Au + Au Collisions at the AGS. *Nucl. Phys. A*, 610:153C–164C, 1996.

[146] S. Ahmad et al. Lambda Production by 11.6 A GeV/c Au Beam on Au Target. *Phys. Lett. B*, 382:35–39, 1996. [Erratum: Phys.Lett.B 386, 496–496 (1996)].

[147] J. L. Klay et al. Charged Pion Production in 2 to 8 A GeV Central Au + Au Collisions. *Phys. Rev. C*, 68:054905, 2003.

[148] J. L. Klay et al. Longitudinal Flow from 2 A GeV to 8 A GeV Au + Au Collisions at the Brookhaven AGS. *Phys. Rev. Lett.*, 88:102301, 2002.

[149] S. V. Afanasiev et al. Energy Dependence of Pion and Kaon Production in Central Pb + Pb Collisions. *Phys. Rev. C*, 66:054902, 2002.

[150] C. Alt et al. Directed and Elliptic Flow of Charged Pions and Protons in Pb + Pb Collisions at 40 A GeV and 158 A GeV. *Phys. Rev. C*, 68:034903, 2003.

[151] C. Alt et al. Pion and Kaon Production in Central Pb + Pb Collisions at 20 A and 30 A GeV: Evidence For the Onset of Deconfinement. *Phys. Rev. C*, 77:024903, 2008.

[152] Chi Yang. Prototype Sector Production for the STAR Inner TPC Upgrade. *J. Phys. Conf. Ser.*, 779(1):012082, 2017.

Appendix

A 博士论文中文简介

量子色动力学 (QCD) 是描述夸克和胶子之间的强相互作用的理论，1972 年由默里 · 盖尔曼 (Murray Gell-Mann) 和哈拉尔德 · 弗里奇 (Harald Fritzsch) 提出。在高温高密下，强相互作用物质会发生相变 (QCD 相变)，此时禁闭在核子中的夸克、胶子自由度将从核子中逃逸出来，形成由夸克和胶子自由度组成的夸克胶子等离子体 (QGP)。在相对论重离子碰撞实验中，通过不同加速能量加速初始重离子的碰撞，获得不同的温度和重子化学势，来研究极端条件下 QCD 相图和强相互作用核物质的特性。QCD 相图以重子化学势 (μ_B) 为横坐标，以热力学参数温度 (T) 为纵坐标表，描绘了核物质的相结构及相变过程。第一性原理有限温度下的格点量子色动力学 (Lattice QCD) 预测，在相图上的高温低重子密度区，从强子物质相到夸克胶子等离子体 (QGP) 相的转变是连续的平滑穿越。而在低温，高重子密度区，两相之间是一阶相变。一阶相变的终结点，被称为 QCD 临界点 (CP)。寻找一阶相边界和临界点是高能重离子实验的一个主要目的。

理论研究表明，在临界点附近，系统的关联长度 (ξ) 发散，此时系统中的局域重子数密度会出现不同程度的涨落。因此实验上通过测量守恒荷的高阶累积量来反映关联长度的发散行为，被作为寻找核物理中 QCD 临界点的敏感观测量。在相对论重离子碰撞 (RHIC) 能量扫描第一阶段 (BES-I), STAR 采集了质心碰撞能量从 7.7 到 200 GeV 的数据，在该能区的研究发现，净质子数 (质子数-反质子数) 的四阶涨落在最中心碰撞存在非单调的能量依赖趋势。另一方面，在这一能区对轻核的研究也发现，轻核产额比 ($N_t \times N_p/N_d^2$) 最中心碰撞的结果在 20 GeV 附近也存在较为显著的非单调能量依赖趋势。轻核 (至少包含一个中子和一个质子) 是在相对论重离子碰撞系统中可以被直接测量到的粒子，其产额比可以有效地消除单个轻核产额中的体积，温度等效应，与系统的中子数密度涨落直接相关，是 QCD 临界点和一阶相变的又一个敏感观测量。这些研究为 QCD 相图的研究提供了非常重要的信息，但是其研究结果还存在较大的误差。RHIC-STAR 第二能量扫描阶段增大了数据统计量，为进一步精确实验结果，准确寻找临界点提供了条件。此外，STAR 固定靶实验采集了碰撞能量低至 3.0 GeV 的实验数据，对较低碰撞能量的实验研究将会是探索高重子化学势区域 QCD 相结构的重要任务。

自 2018 年，STAR 正式开始采集固定靶模式下金核 + 金核碰撞的实验数据，质心系能量 3.0 GeV (对应每个核子约 3.85 GeV) 的实验数据最先被用于实验数据分析。该能量将重子化学势的范围扩大到约 750 MeV，基于最高能量 200 GeV 的数据，我们可以研究 QCD 相图上，重子化学势从 750 到 25 MeV 的很宽范围。对于研究一阶相变边界和寻找临界点有着重要的作用。本论文将给出 3.0 GeV 金核 + 金核碰撞实验中质子及轻核的测量过程及结果，计算该能量下粒子产额比和有关轻核产生机制的观测量，与较高碰撞能量的实验结果进行对比，讨论在这一能区相结构的性质。

论文分为以下几个章节：

第 1 章介绍论文的研究背景，研究动机，并对基本的实验观测量进行了简单介绍。

研究背景、研究动机：宇宙大爆炸是从一个高温高密的状态迅速膨胀的过程，在大爆炸后的微秒级别的演化过程中，宇宙逐渐冷却，膨胀，形成我们所熟知的宇宙。在宇宙大爆炸的整个过程中，基本粒子起着关键的作用，它是构成物质世界最基本的组成部分。在初始的高温高密环境中，基本粒子和反粒子反复地产生，湮灭，形成“热平衡态”。随着宇宙的冷却和膨胀，基本粒子的相互作用逐渐变弱。自然界的基本相互作用有以下四种：强相互作用、电磁相互作用、弱相互作用和引力相互作用。强相互作用是这里提到的主要相互作用力，也是高能物理实验的主要研究对象。

量子色动力学及相变临界点：1972 年，默里 · 盖尔曼（Murray Gell-Mann）提出量子色动力学（QCD）来描述强相互作用。它是描述夸克和胶子之间强相互作用的标准动态理论。它有两个独特的性质：色禁闭和渐近自由。在低能量时，夸克和胶子的相互作用很强，它们被限制在强子物质中。例如，一个夸克和反夸克组成介子，三个夸克组成重子。渐近自由是大卫 · 乔纳森 · 格罗斯（David Jonathan Gross）、弗兰克 · 安东尼 · 维尔切克（Frank Anthony Wilczek）和休 · 大卫 · 波利策（Hugh David Politzer）于 1973 年发现的 QCD 的一个重要性质。他们发现，强相互作用只在极短距离内起作用，而在长距离内，色荷之间的相互作用会变弱。量子色动力学耦合常数是描述夸克和胶子之间相互作用强度的参数，在低能量尺度下，耦合常数变大，导致夸克和胶子之间的强相互作用；而在高能量尺度下，由于渐近自由，耦合常数变小，表明夸克和胶子几乎像自由粒子一样运动。换句话说，在高温高密条件下，强相互作用物质会发生相变 (QCD 相变)，此时禁闭在核子中的夸克、胶子将从核子中逃逸出来，形成由夸克和胶子组成的夸克胶子等离子体 (QGP)。QCD 相图通常绘制在温度-重子化学势的二维平面上。在零重子化学势时，从第一性原理出发，格点 QCD 预测高温低重子密度区，从强子物质相到夸克胶子等离子体 (QGP) 相的转变是连续的平滑穿越。而在低温，高重子密度区，两相之间是一阶相变。一阶相变的终结点，被称为 QCD 临界点 (CP)。理解和研究 QCD 相结构，寻找和确定相图上一阶相边界和临界点的位置是高能物理实验上一个活跃的研究领域。相对论重离子碰撞实验中，两个以相反方向运动的原子核被加速到接近光速，当它们在极高能量下碰撞时，会产生相当高的局部温度和能量密度。模拟早期宇宙条件，在这种高温和高密度条件下，物质发生夸克胶子等离子体和强子物质间的转化。在临界点附近，系统涨落的相关长度会急剧增加，空间

相关性趋向于长程相关性，从而导致系统的临界涨落。守恒量，如净重子 (B) 数、净电荷（Q）数和净奇异（S）数等逐事件分布的高阶累积量，对关联长度高度敏感，是寻找 QCD 相变临界点的灵敏观测量。同样，在临界点附近也会出现中子密度涨落，然而，中子不带电，不易被探测器探测到。因此，需要找到一种能够反映中子密度涨落的观测指标。

轻核的产生：轻核通常是指质子数小于 20 的原子核，从广义上讲，轻核包括氢（H）、氦（He）、锂（Li）、铍（Be）、硼（B）等元素及其相应的同位素。一方面，轻核是至少含有一个质子和一个中子的原子团，可以被探测器直接探测到。另一方面，轻核的结合能较小，其形成和存在很大程度上反映系统中核物质的性质。因此，研究轻核可以探索核力，发现丰富的核结构。轻核的形成机制是轻核产生的重点研究方向之一，目前的两种主流机制分别为：核子聚合产生和热发射。聚合产生的原理是当核子在坐标空间和动量空间相互靠近时，核子会聚集在一起并“凝聚”成一个复合粒子。因此轻核的形成会受到系统局域重子数密度涨落的影响，从而反映系统中物质的相变和临界现象。热力学统计模型认为轻核与质子，中子等类似，是在系统演化过程中直接发射出来的。该模型假定系统处于局域热平衡，粒子的产率对化学冻结温度和化学势很敏感。目前实验条件已经可以精确测量到氘核，氚核，氦-3，氦-4 等，锂，铍等包含更多核子数的轻核也已经可以被测量到。轻核的测量将会更精确的反映系统局域密度涨落的信息。

第 2 章介绍 STAR 实验装置，测量中用到的主要探测器以及固定靶碰撞模式。

相对论重离子对撞机：位于美国长岛的布鲁克海文国家实验室是研究宇宙物质演化的重要实验室。该实验室的相对论重离子对撞机 (RHIC) 是高能物理领域的实验装置之一。重离子从电子束离子源加速器 (EBIS) 发射，随后，离子前进到圆形助推器，在那里它们经历连续加速，每次通过都达到更高的能量水平。然后离子进入交替梯度同步加速器，并通过专用束线注入 RHIC 的两个环中。在 RHIC 加速环内，光束通过无线电波接收最终的能量提升。一旦加速，离子就可以在环内运行很长时间。RHIC 环于 1999 年完工，周长约为 2.4 英里。该环包括四个探测器，分别是 BRAHMS，STAR，PHENIX 和 PHOBOS。在过去的二十年里，RHIC 成功地加速并碰撞了不同的光束类型：质子 + 质子、质子 + 铝、质子 + 金核、氦核 + 金核、铜核 + 铜核、铜核 + 金核、金核 + 金核、铀 + 铀。这些探测器获取碰撞系统的信息，以揭示可见物质、夸克和胶子的基本组成部分。

STAR 探测器：STAR 探测器是 RHIC 加速环上目前还在运行的一个重要的探测器，它具有非常大且均匀的接受度，覆盖中心快度周围很宽的方位角。STAR 实验的主要目的是探索极高能量密度下新物质态的存在，并研究量子色动力学（QCD）相结构。该探测器可利用高空间和时间分辨率进行粒子识别和动量分析，并可以测量宽立体角的强子产物。时间投影室 (TPC) 和飞行时间探测器 (TOF) 是 STAR 探测器上的主要跟踪装置。TPC 是一个长 4.2 米，直径为 4 米的圆柱体，被放置在一个磁场强度为 0.5 T 的大体积螺线管磁铁中，其内部放置了一个场强约为 135 V/cm 的均匀漂移电场。TPC 通过识别粒子路径上的电离簇，确定各自的 X、Y 和 Z 空间坐标，重建初始粒子的轨迹。它可以记录粒子轨迹，测量粒子动量，并根据粒子在 TPC 内的电离能量损失（dE/dx）来识别粒子。TOF 是安装在 TPC 外围的桶装结构，在 2010 年

投入使用，极大地扩展了 STAR 探测器的覆盖范围。TOF 通过记录粒子经过该探测器的时间，结合 TPC 探测器测得的粒子移动路径长度和动量，获得粒子的飞行速度及质量，从而识别粒子种类。

STAR 固定靶实验： STAR 固定靶装置将金靶 (厚度为 0.25 毫米的金箔) 安装在真空管道内，位于 TPC 的几何中心西侧约 200.7 厘米，中心轴线向下 2 厘米的位置。不同于对撞时两束束流均携带能量，固定靶模式通过加速粒子撞击固定金靶，旨在采集更低碰撞能量，更高重子密度区的数据。同时，碰撞发生于 TPC 的一端，因此末态粒子的径迹可以覆盖更大的快度和赝快度范围。

第 3 章介绍数据筛选，粒子的鉴别和效率修正等。

数据的筛选及中心度定义： 本分析中使用的数据集来自 STAR 实验在单束能量为 3.85 GeV 的金核 + 金核碰撞的固定靶程序，对应的质心系能量约为 3 GeV。使用触发器 ID 为 620052 的最小偏差事件，数据集序号（Run ID）为 19151029 至 19155022。在对数据质量分析筛选后，去除了 35 兆质量较差的数据，最终被应用于分析的数据有 260 兆。考虑固定金靶的安装位置，顶点的选择条件为 x, y 平面半径为 2 厘米的圆形区域（$V_x^2 + (V_y + 2)^2 < 2^2$），z 方向 200±2 厘米的区域（$198 < V_z < 202$）。实验数据的中心度由带电粒子多重数来定义，其方式是将带电粒子多重数的分布图积分，按照总值的百分比来划分不同的碰撞中心度。在碰撞实验中，越中心的碰撞事件就会有越多的末态粒子被探测到。因此，中心 0-10% 的数据即带电粒子多重数最大的 10% 所对应的区域。

粒子鉴别： 本分析中粒子的鉴别主要是通过时间投影室和飞行时间探测器完成的。由于不同粒子的质量差别，在系统中的运行轨迹会有差别。在低动量或低横动量区，通过 TPC 获取的电离能量损失分布可以很好的区分不同粒子。方法是将电离损失的能量与 Bichsel 模型给出的对应粒子的能量损失值进行比较，如公式 3.2.1，得到对应粒子的信号分布 (质子：$n\sigma_p$，轻核：Z)。$n\sigma_p$ 和 Z 分布基本符合均值为零的高斯分布，因此通过高斯分布拟合粒子信号来获得低横动量的粒子数。在高动量或高横动量区，由于粒子损失的能量非常接近，无法通过上述方法很好的区分粒子类别。因此，使用 TOF 记录的粒子的飞行时间，结合粒子的运行长度和动量信息，通过公式 3.2.3计算粒子的质量，增加粒子对应的质量信息鉴别条件，从而得到更高纯度的粒子信息。分析发现，粒子的质量平方分布可以由学生-t 公式很好地描述，因此在高动量区，通过该公式提取对应粒子数。

效率修正： 由于各探测器的分辨率，粒子鉴别过程中的背景污染，以及实验材料等影响，最终的实验结果需要经过对应的效率修正，一般来说，对产额的分析需要进行 TPC 跟踪效率修正，TOF 匹配效率修正，能量损失修正，吸收校正和由于高能粒子与探测器材料或束流管相互作用产生的背景污染的修正。TPC 跟踪效率和接受度是通过所谓的嵌入技术确定的。该技术是在给定的运动学范围内，将使用 STAR 探测器和探测器响应模拟器的 GEANT 模型模拟的蒙特卡罗（MC）轨迹采样嵌入到原始数据级的真实事件中，以确定重建嵌入轨迹的质量和数量。接受和重构效率最终由重构轨道与嵌入 MC 轨道的比率给出。在 TOF 上记录轨迹的主要算法

包括将 TOF 上的测量点与 TPC（全局）轨迹进行匹配。如果 TPC 中的多条轨道同时出现在 TOF 的单个读取垫上，则不会记录 TOF 测得的这些轨道。当一个轨道对应 TOF 中的多个命中点时，会选择最接近的命中点。因此，TOF 匹配效率是 TOF 匹配的轨迹数与 TPC 识别的轨迹数的比值。低动量粒子在穿越探测器材料时会损失大量能量。因此，有必要对这些粒子，尤其是较重粒子的能量损失进行修正。能量损失效率通过比较重建的和嵌入的 MC 轨道之间的横动量差值来计算。此外，在重离子碰撞中，奇异重子（如 Λ 和 Ξ 及其反粒子）通过弱衰变将衰变为（反）质子，影响其最终产率。要得到（反）质子的原始产率，就必须减去弱衰变的贡献。通过将测量到的 Λ 和 Ξ 的结果作为输入，考虑对应粒子的衰变通道以及分支比，来获取弱衰变的贡献率。最终计算结果表明，在 3 GeV 下（Λ、Σ^+、Ξ^-, 和 Ξ^0）弱衰变对质子产率的最大贡献约为 2%。

第 4 章展示了 3 GeV 碰撞能量下的分析结果。我们系统地测量了质子 (p) 和轻核 (d, t, ^{3}He, 和 ^{4}He) 从中心到边缘 (0-10%，10-20%，20-40%，和 40-80%) 碰撞的横动量 (p_T) 谱，并首次将快度范围扩展到靶向快度进行测量。计算了平均横动量及粒子产额的中心度和快度依赖。基于从中心快度到前/后向快度的测量结果，给出了较为精确的粒子的全空间产额。同时发现在靶向快度，质量较大的轻核更容易形成，其贡献主要来自于核碎片。在 3 GeV 对轻核的复合产额比的计算中，首先给出了不同中心度和快度范围内包含质子 (p)，氘核 (d)，和氚核 (t) 的比值。其次，基于该能量下轻核的丰度，还计算了包含氦核 (^{3}He 和 ^{4}He) 的复合产额比。这些比值给出了基本一致的中心度和快度依赖趋势。计算发现，$N_t \times N_p/N_d^2$ 没有展示出明显的中心度依赖行为，这与普通输运模型所显示的从中心碰撞到边缘碰撞逐渐增大的趋势不同。然而当我们在输运模型 (AMPT) 中加入一阶相变的状态方程时，却展示出与实验一致的平坦的中心度依赖趋势。另外，该输运模型也展示出与实验观测一致的能量依赖趋势。这为研究低碰撞能量下轻核的形成机制，以及研究高重子密度区的 QCD 相结构特性提供了重要的实验依据。

第 5 章对爆炸波模型进行了讨论。爆炸波模型是一个理论框架，用于描述高能重离子碰撞中产生的粒子的集体运动，特别是在相对论重离子物理学中。该模型假定，在碰撞的早期阶段，系统可以用流体力学，特别是相对论流体力学来描述。然后利用爆炸波来模拟系统从初始状态到最终冻结构型的演变过程，从而了解碰撞中产生的高密度热物质的特性。与爆炸产生的爆炸波类似，爆炸波模型将膨胀粒子源近似为经历快速爆炸膨胀的流体。在碰撞过程的凝固阶段，系统中产生的粒子不再发生强烈的相互作用，而是逃离系统。不同粒子的横动量分布反映了物质在运动学冻结阶段，即弹性碰撞停止后的性质。此时，粒子进入弹性碰撞阶段，其动量信息不会发生变化。通过使用爆炸波模型提取运动学冻结温度和横向集体速度，发现 3 GeV 的温度整体低于 BES-I（碰撞能量为 7.7 – 200 GeV）的温度，且 3 GeV 的温度 vs. 速度的趋势与高能量明显不同，因此考虑在低能系统有着不同的状态方程，为更多低能的分析提供了参考价值。

第 6 是对整个分析的总结与展望。本论文展示了 3 GeV 质子和轻核产生的全面的测量结果，首次计算了几乎全空间的粒子产额。发现旁观者碎片的贡献在低碰撞能量，尤其是边缘碰撞中更加明显。在 3 GeV 对质子和轻核的产生进行的系统测量，为我们了解轻核的产生机制以

及高重子密度下的 QCD 相结构提供了重要的实验依据。2018 年起，STAR 对子探测器进行了升级，包括内部 TPC 探测器（iTPC）、端盖 TOF 探测器（ETOF）和事件平面探测器（EPD）。这些子探测器的升级，利用这些探测器，将有助于鉴别到更低横动量，更大快度和赝快度的粒子，将会大大提高测量结果的精确度。

B Signal Extraction for particles

Figure B.1 - Fig. B.4 show the distribution of $n\sigma_p$ and m^2 for protons at different p_T bins, rapidity windows, and collision centralities.

Figure B.5 - Fig. B.8 show the distribution of Z_d and m^2 for deuterons at different p_T bins, rapidity windows, and collision centralities.

Figure B.9 - Fig. B.12 show the distribution of Z_t and m^2 for tritons at different p_T bins, rapidity windows, and collision centralities.

Figure B.13 - Fig. B.16 show the m^2 distribution for ^{3}He, at different p_T bins, rapidity windows, and collision centralities.

Figure B.17 - Fig. B.20 show the m^2 distribution for ^{4}He, at different p_T bins, rapidity windows, and collision centralities.

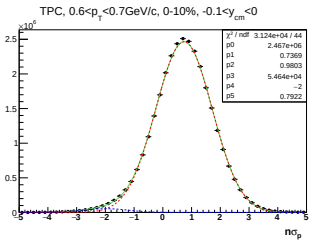
TPC, 0.6<p_T<0.7GeV/c, 0-10%, -0.1<y_cm<0
nσ_p

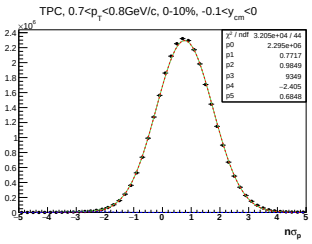
TPC, 0.7<p_T<0.8GeV/c, 0-10%, -0.1<y_cm<0
nσ_p

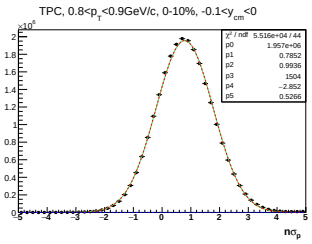
TPC, 0.8<p_T<0.9GeV/c, 0-10%, -0.1<y_cm<0
nσ_p

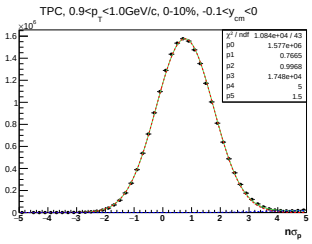
TPC, 0.9<p_T<1.0GeV/c, 0-10%, -0.1<y_cm<0
nσ_p

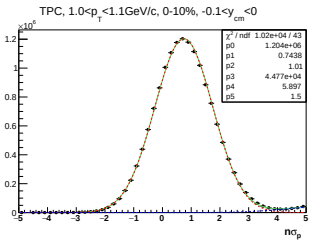
TPC, 1.0<p_T<1.1GeV/c, 0-10%, -0.1<y_cm<0
nσ_p

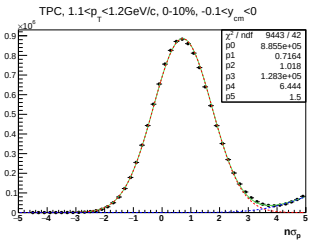
TPC, 1.1<p_T<1.2GeV/c, 0-10%, -0.1<y_cm<0
nσ_p

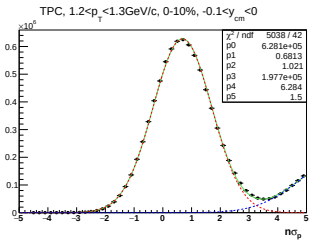
TPC, 1.2<p_T<1.3GeV/c, 0-10%, -0.1<y_cm<0
nσ_p

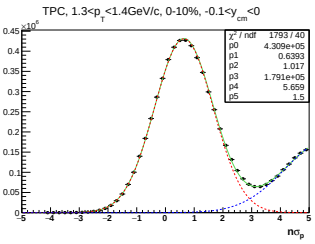
TPC, 1.3<p_T<1.4GeV/c, 0-10%, -0.1<y_cm<0
nσ_p

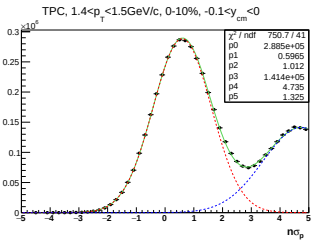
TPC, 1.4<p_T<1.5GeV/c, 0-10%, -0.1<y_cm<0
nσ_p

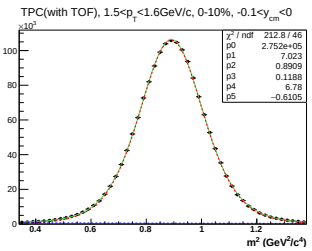
TPC(with TOF), 1.5<p_T<1.6GeV/c, 0-10%, -0.1<y_cm<0
m² (GeV²/c⁴)

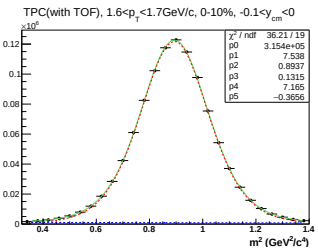
TPC(with TOF), 1.6<p_T<1.7GeV/c, 0-10%, -0.1<y_cm<0
m² (GeV²/c⁴)

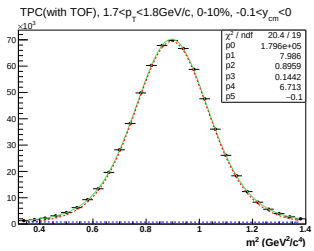
TPC(with TOF), 1.7<p_T<1.8GeV/c, 0-10%, -0.1<y_cm<0
m² (GeV²/c⁴)

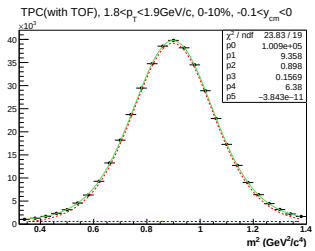
TPC(with TOF), 1.8<p_T<1.9GeV/c, 0-10%, -0.1<y_cm<0
m² (GeV²/c⁴)

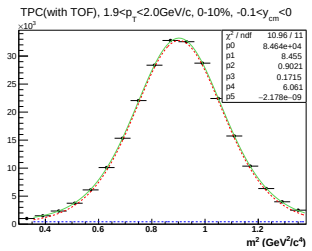
TPC(with TOF), 1.9<p_T<2.0GeV/c, 0-10%, -0.1<y_cm<0
m² (GeV²/c⁴)

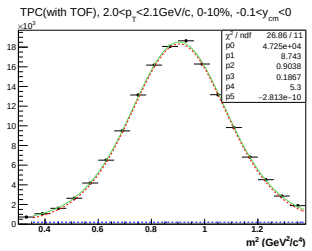
TPC(with TOF), 2.0<p_T<2.1GeV/c, 0-10%, -0.1<y_cm<0
m² (GeV²/c⁴)

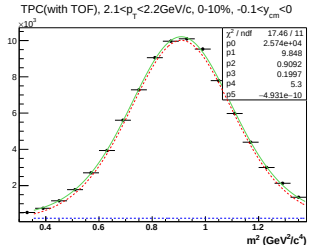

Figure B.1: $n\sigma_p$ and m^2 distributions of proton at $-0.1 < y < 0$ rapidity range in 0-10% Au+Au collisions at $\sqrt{s_{\rm NN}} = 3$ GeV. The red lines indicate the signal fits. The blue lines indicate the background fits. The green lines represent the result of the simultaneous fitting of signal and background.

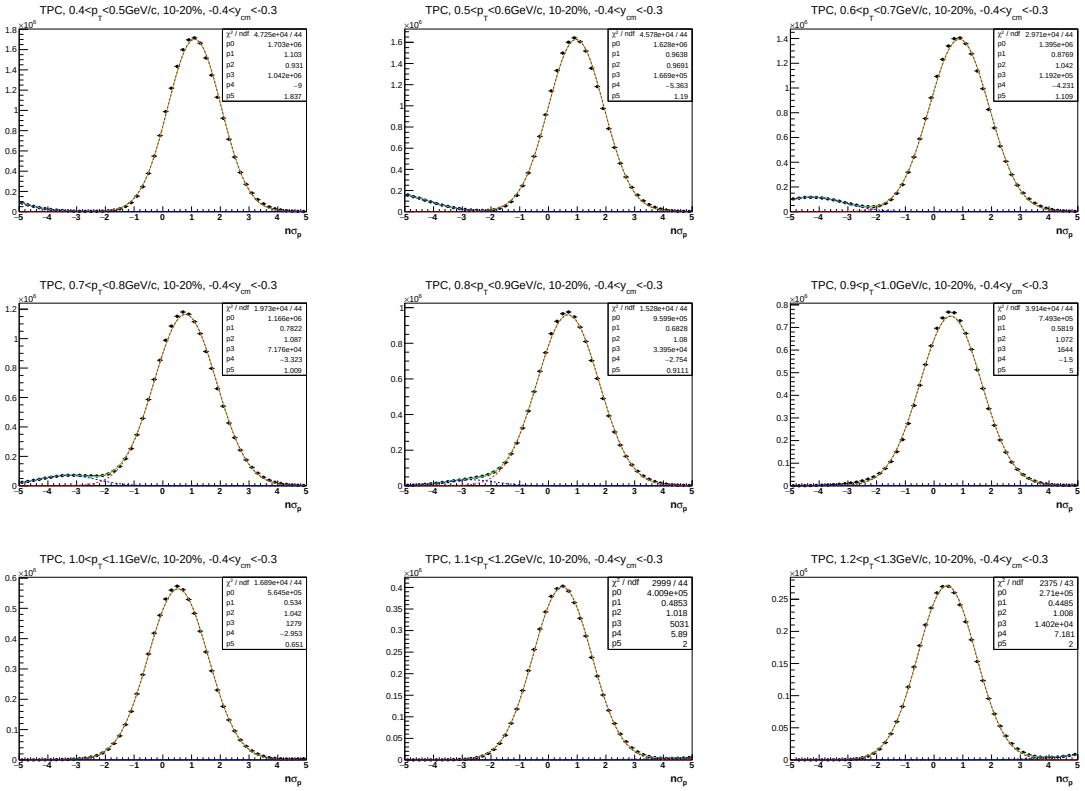

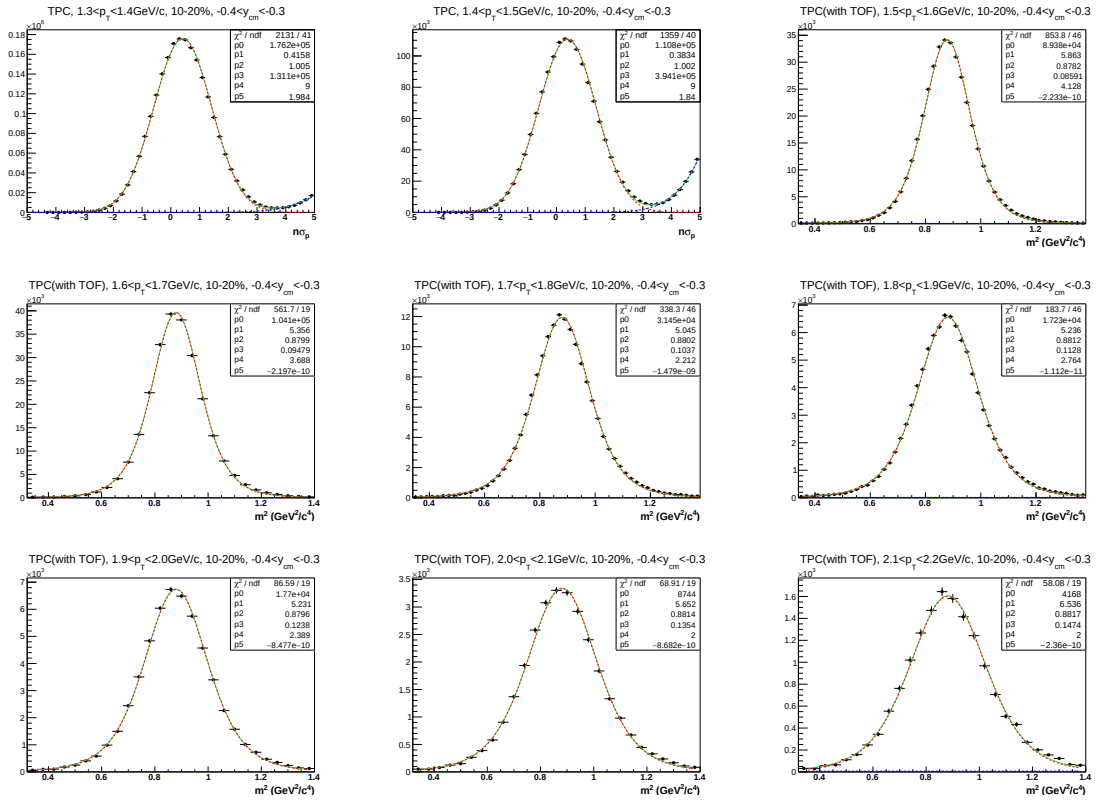

Figure B.2: $n\sigma_p$ and m^2 distributions of proton at $-0.4 < y < -0.3$ rapidity range in 10-20% Au+Au collisions at $\sqrt{s_{\rm NN}} = 3$ GeV. The red lines indicate the signal fits. The blue lines indicate the background fits. The green lines represent the result of the simultaneous fitting of signal and background.

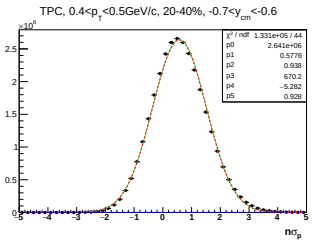
TPC, 0.4<p_T<0.5GeV/c, 20-40%, -0.7<y_cm<-0.6
nσ_p

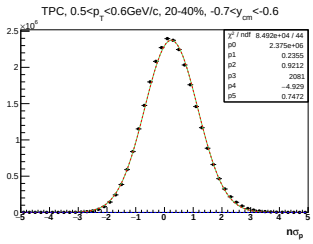
TPC, 0.5<p_T<0.6GeV/c, 20-40%, -0.7<y_cm<-0.6
nσ_p

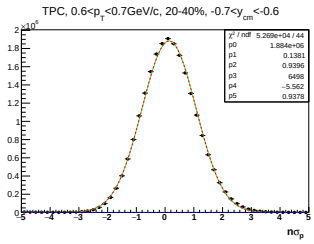
TPC, 0.6<p_T<0.7GeV/c, 20-40%, -0.7<y_cm<-0.6
nσ_p

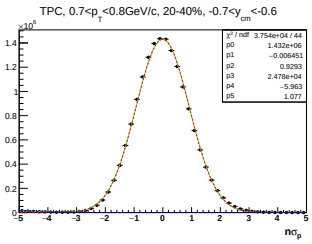
TPC, 0.7<p_T<0.8GeV/c, 20-40%, -0.7<y_cm<-0.6
nσ_p

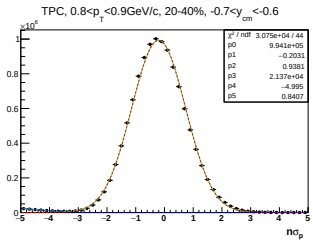
TPC, 0.8<p_T<0.9GeV/c, 20-40%, -0.7<y_cm<-0.6
nσ_p

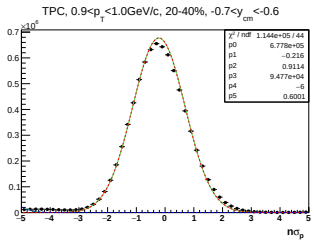
TPC, 0.9<p_T<1.0GeV/c, 20-40%, -0.7<y_cm<-0.6
nσ_p

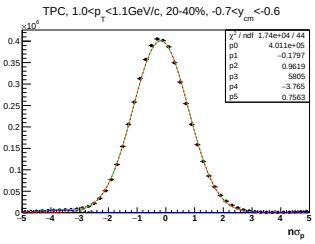
TPC, 1.0<p_T<1.1GeV/c, 20-40%, -0.7<y_cm<-0.6
nσ_p

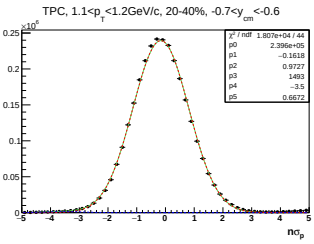
TPC, 1.1<p_T<1.2GeV/c, 20-40%, -0.7<y_cm<-0.6
nσ_p

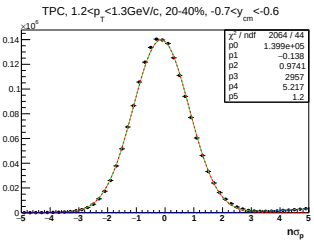
TPC, 1.2<p_T<1.3GeV/c, 20-40%, -0.7<y_cm<-0.6
nσ_p

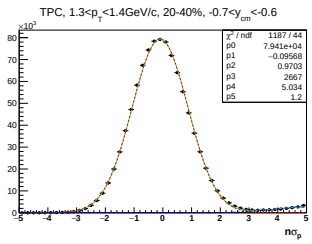
TPC, 1.3<p_T<1.4GeV/c, 20-40%, -0.7<y_cm<-0.6
nσ_p

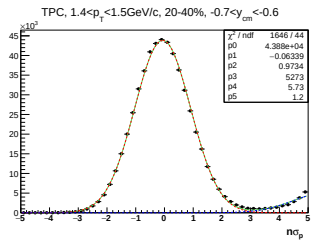
TPC, 1.4<p_T<1.5GeV/c, 20-40%, -0.7<y_cm<-0.6
nσ_p

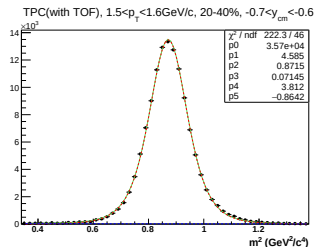
TPC(with TOF), 1.5<p_T<1.6GeV/c, 20-40%, -0.7<y_cm<-0.6
m² (GeV²/c⁴)

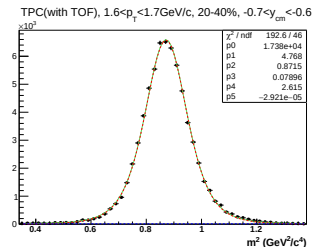
TPC(with TOF), 1.6<p_T<1.7GeV/c, 20-40%, -0.7<y_cm<-0.6
m² (GeV²/c⁴)

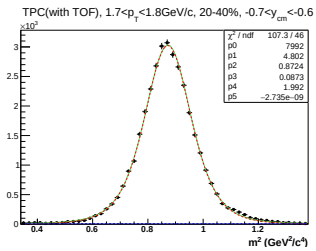
TPC(with TOF), 1.7<p_T<1.8GeV/c, 20-40%, -0.7<y_cm<-0.6
m² (GeV²/c⁴)

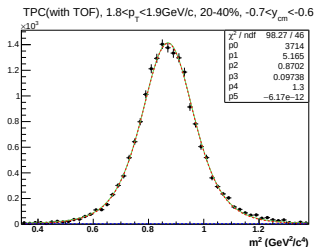
TPC(with TOF), 1.8<p_T<1.9GeV/c, 20-40%, -0.7<y_cm<-0.6
m² (GeV²/c⁴)

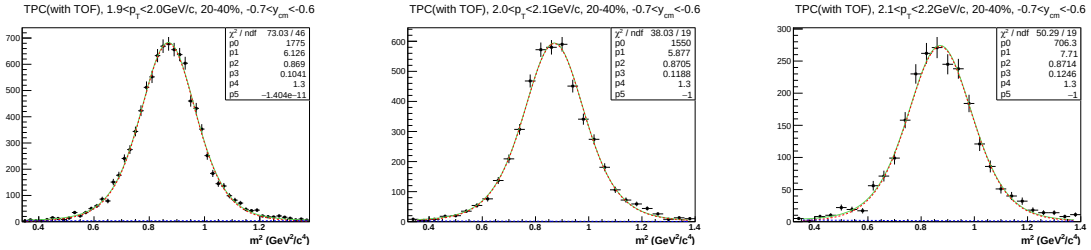

Figure B.3: $n\sigma_p$ and m^2 distributions of proton at $-0.7 < y < -0.6$ rapidity range in 20-40% Au+Au collisions at $\sqrt{s_{\rm NN}} = 3$ GeV. The red lines indicate the signal fits. The blue lines indicate the background fits. The green lines represent the result of the simultaneous fitting of signal and background.

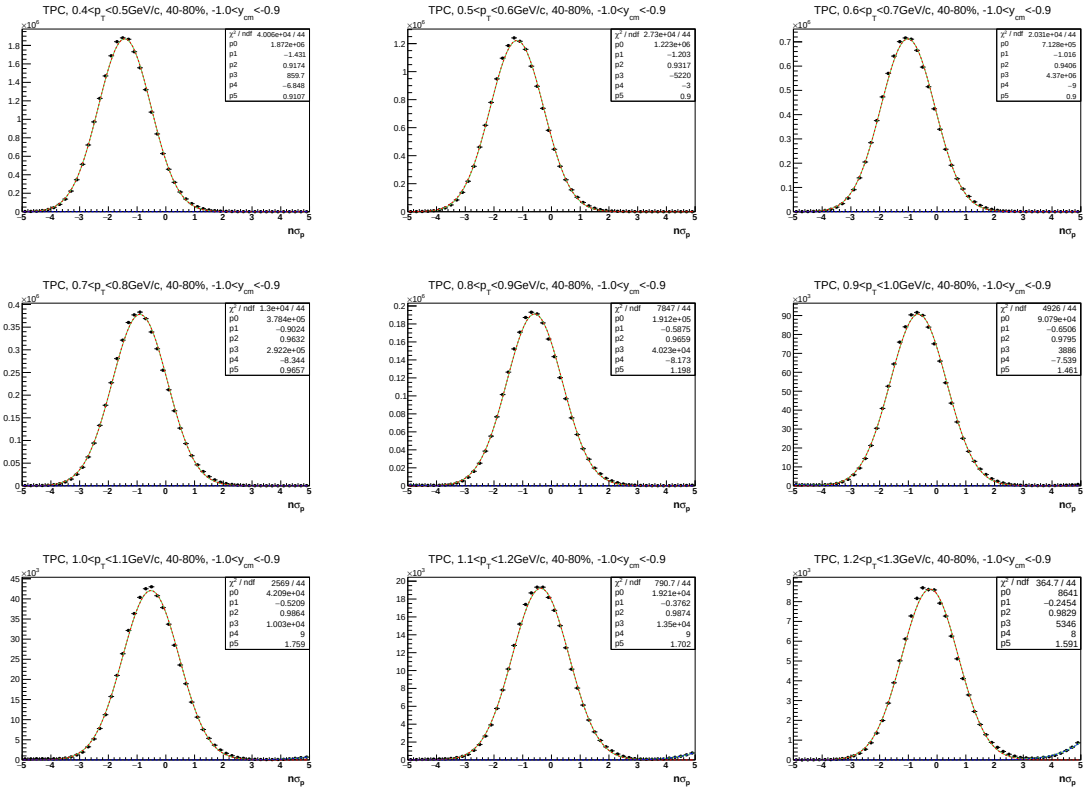

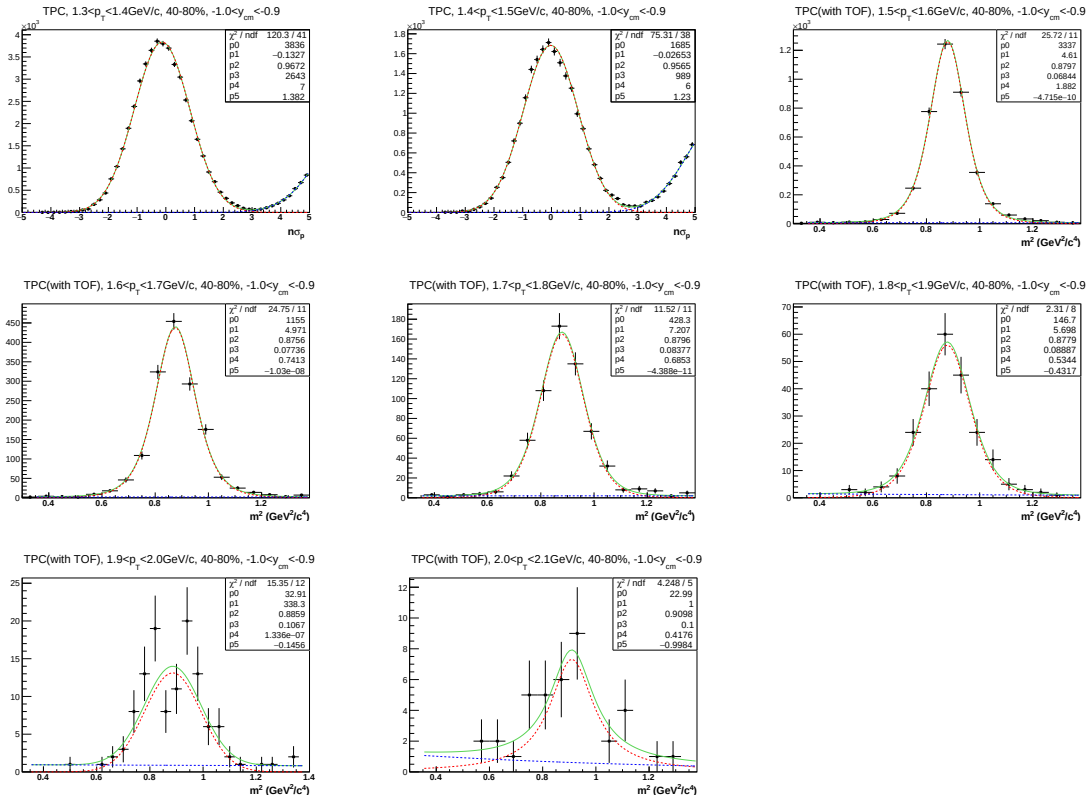

Figure B.4: $n\sigma_p$ and m^2 distributions of proton at $-1.0 < y < -0.9$ rapidity range in 40-80% Au+Au collisions at $\sqrt{s_{\rm NN}} = 3$ GeV. The red lines indicate the signal fits. The blue lines indicate the background fits. The green lines represent the result of the simultaneous fitting of signal and background.

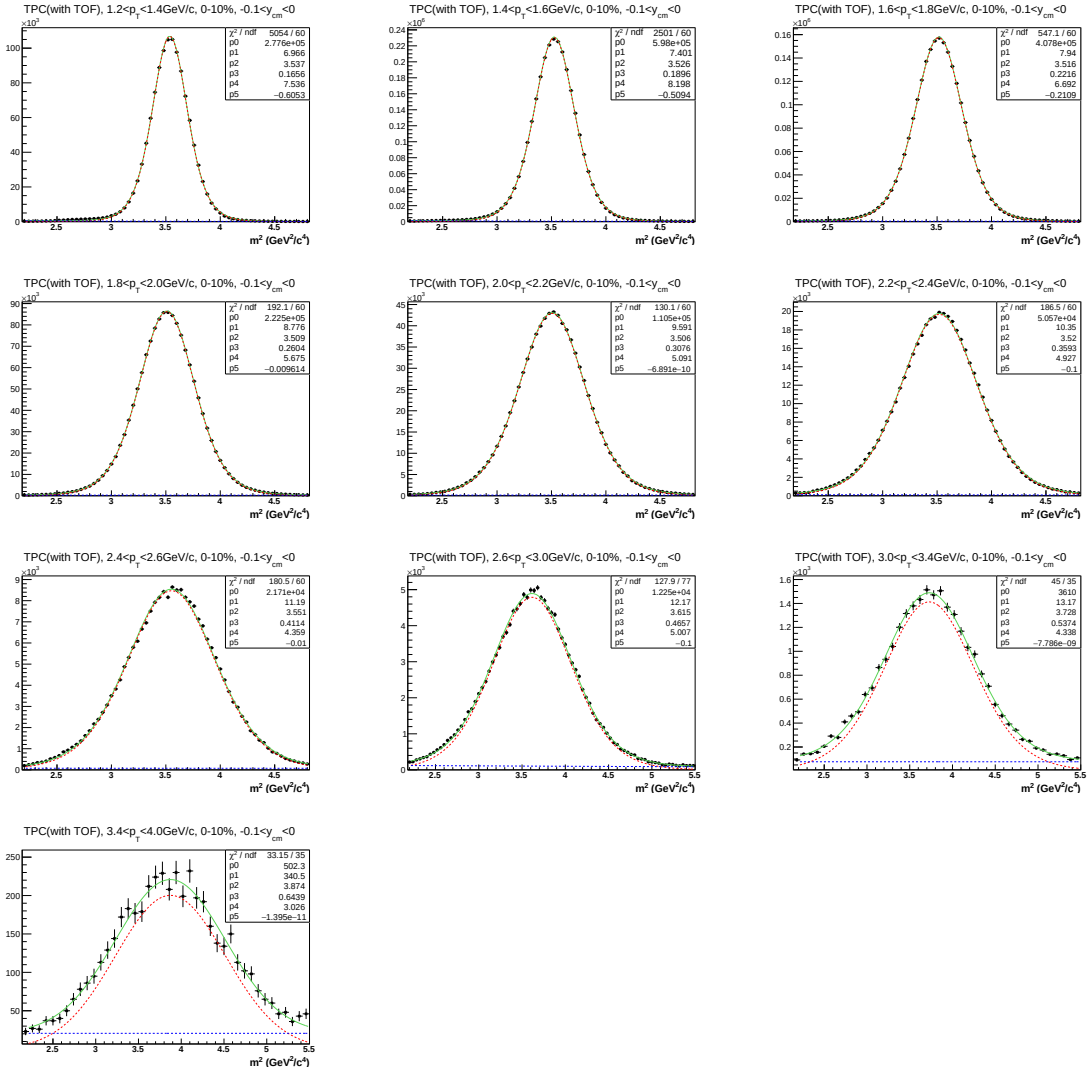

Figure B.5: Z_d and m^2 distributions of deuteron at $-0.1 < y < 0$ rapidity range in 0-10% Au+Au collisions at $\sqrt{s_{\rm NN}} = 3$ GeV. The red lines indicate the signal fits. The blue lines indicate the background fits. The green lines represent the result of the simultaneous fitting of signal and background.

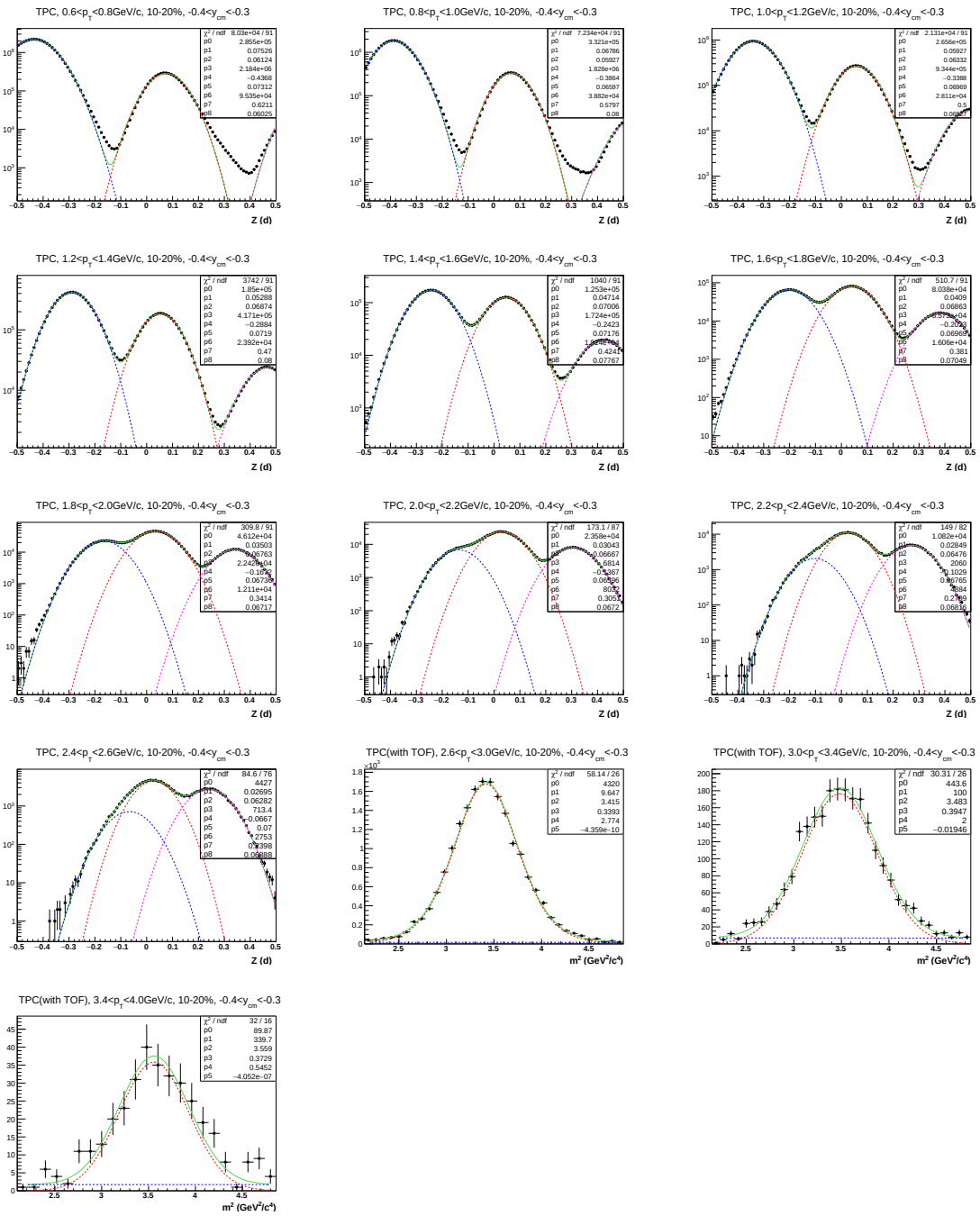

Figure B.6: Z_d and m^2 distributions of deuteron at $-0.4 < y < -0.3$ rapidity range in 10-20% Au+Au collisions at $\sqrt{s_{\rm NN}} = 3$ GeV. The red lines indicate the signal fits. The blue lines indicate the background fits. The green lines represent the result of the simultaneous fitting of signal and background.

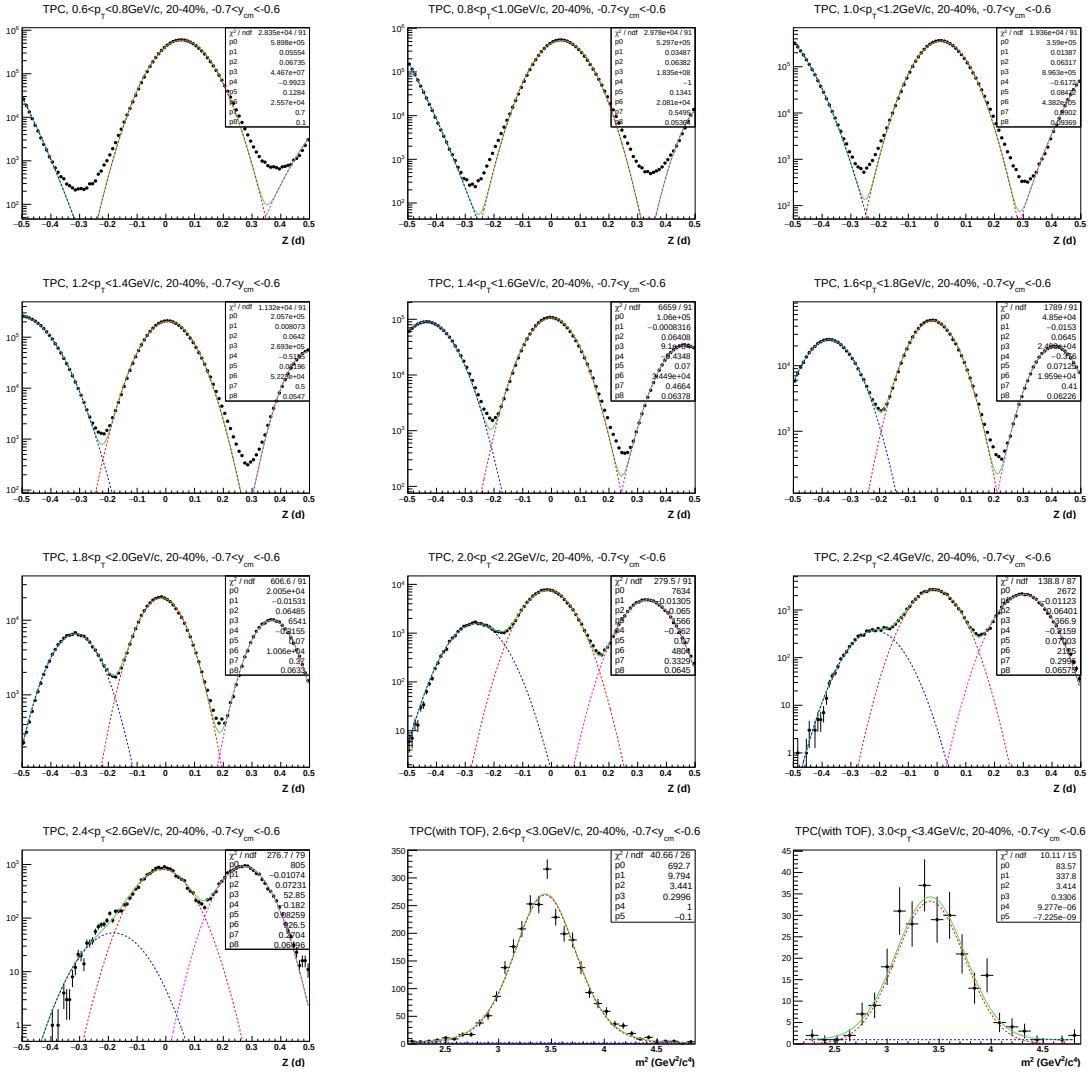

Figure B.7: Z_d and m^2 distributions of deuteron at $-0.7 < y < -0.6$ rapidity range in 20-40% Au+Au collisions at $\sqrt{s_{\rm NN}} = 3$ GeV. The red lines indicate the signal fits. The blue lines indicate the background fits. The green lines represent the result of the simultaneous fitting of signal and background.

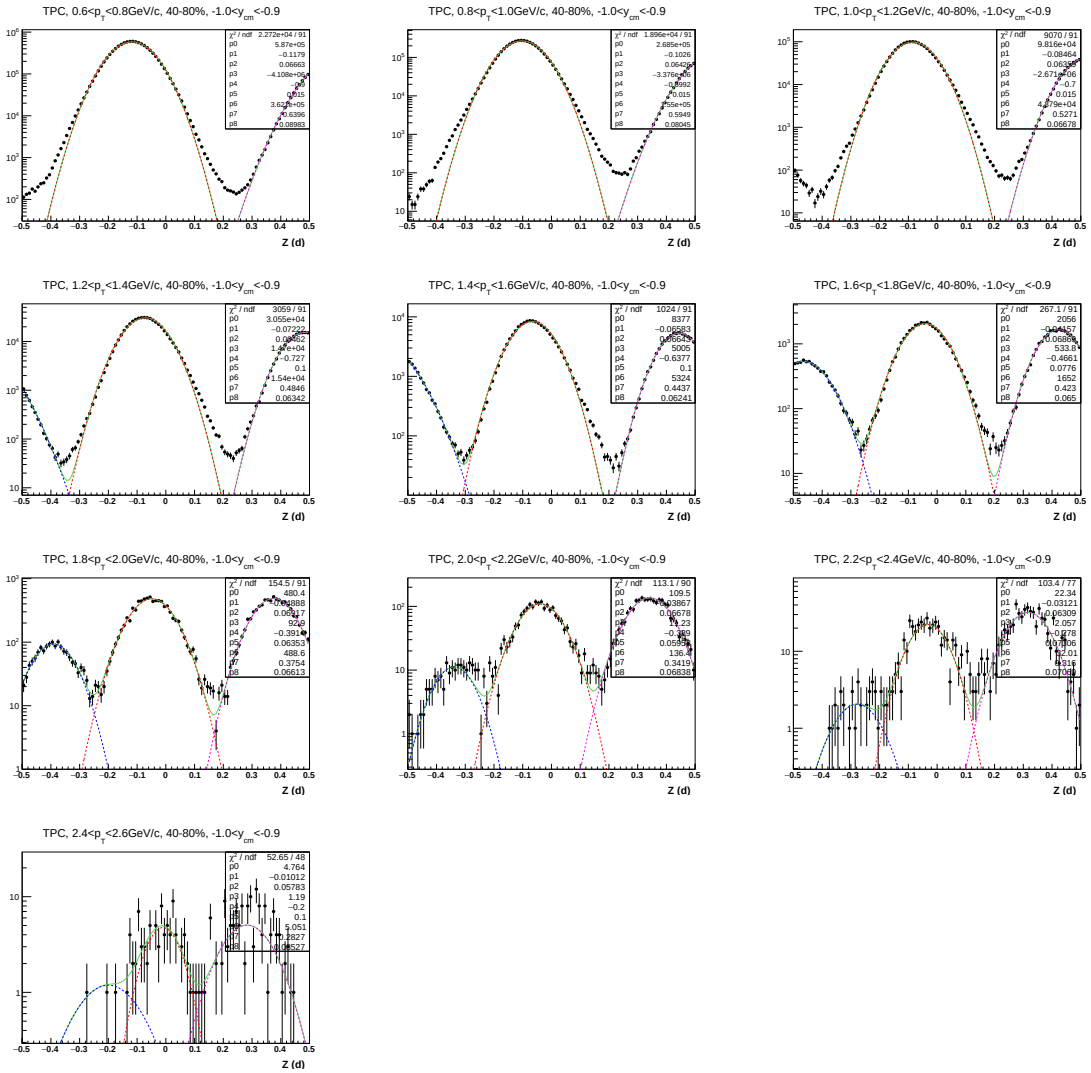

Figure B.8: Z_d and m^2 distributions of deuteron at $-1.0 < y < -0.9$ rapidity range in 40-80% Au+Au collisions at $\sqrt{s_{\rm NN}} = 3$ GeV. The red lines indicate the signal fits. The blue lines indicate the background fits. The green lines represent the result of the simultaneous fitting of signal and background.

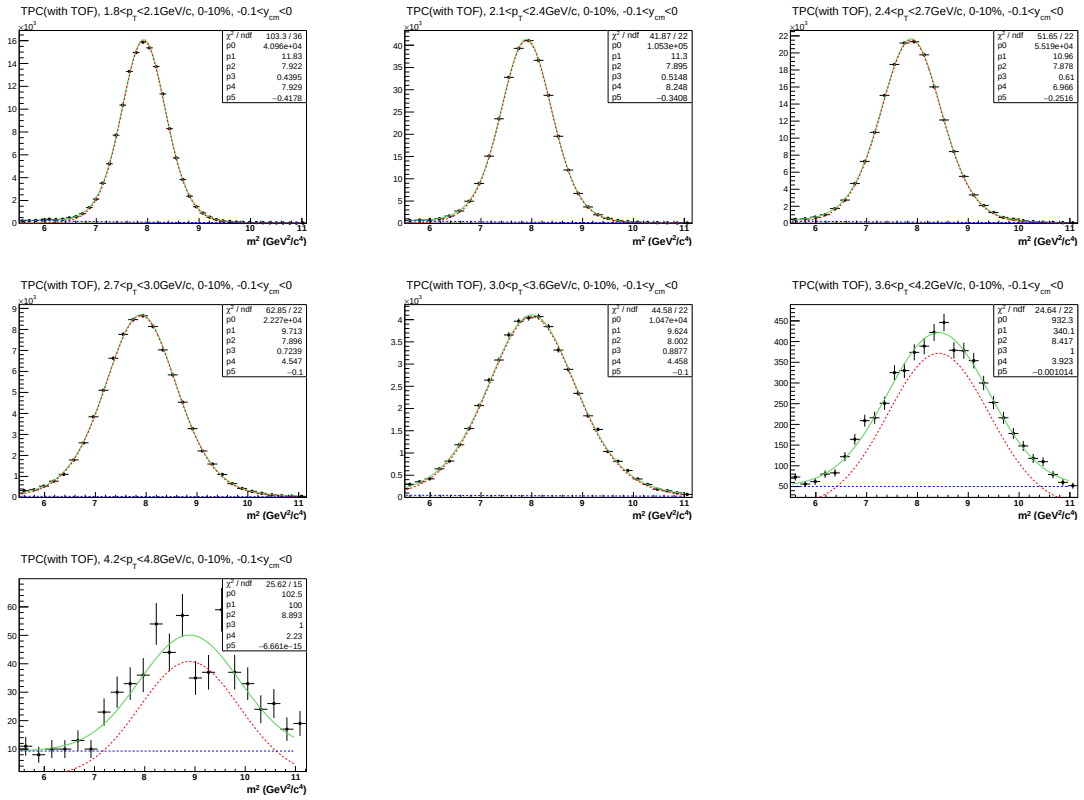

Figure B.9: Z_t and m^2 distributions of triton at $-0.1 < y < 0$ rapidity range in 0-10% Au+Au collisions at $\sqrt{s_{\rm NN}} = 3$ GeV.

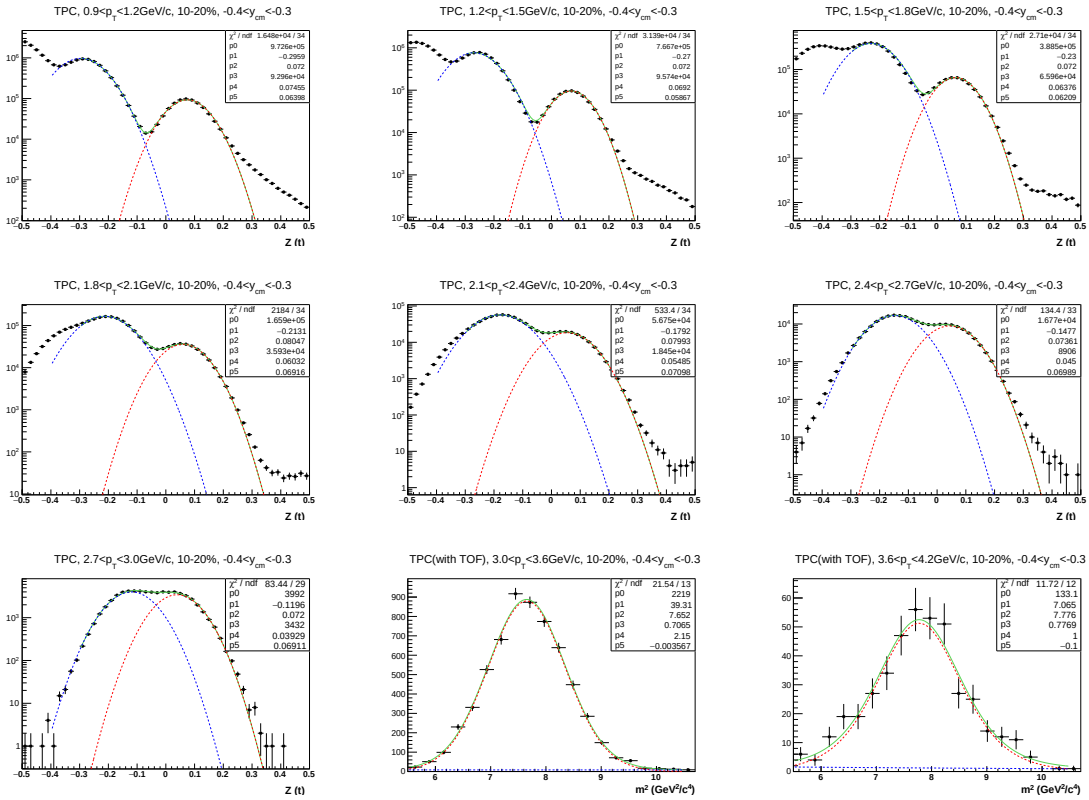

Figure B.10: Z_t and m^2 distributions of triton at $-0.4 < y < -0.3$ rapidity range in 10-20% Au+Au collisions at $\sqrt{s_{\rm NN}} = 3$ GeV.

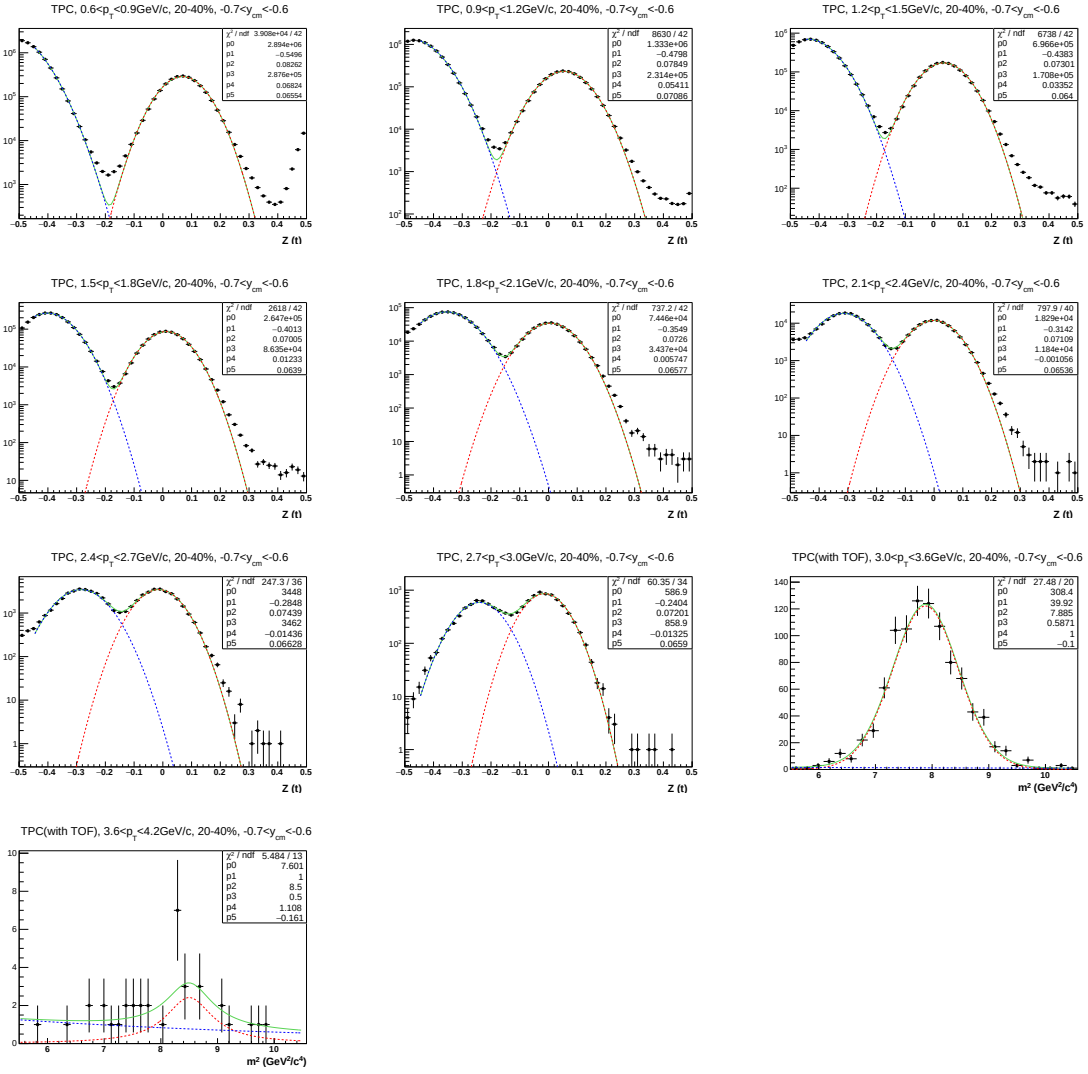

Figure B.11: Z_t and m^2 distributions of triton at $-0.7 < y < -0.6$ rapidity range in 20-40% Au+Au collisions at $\sqrt{s_{\rm NN}} = 3$ GeV.

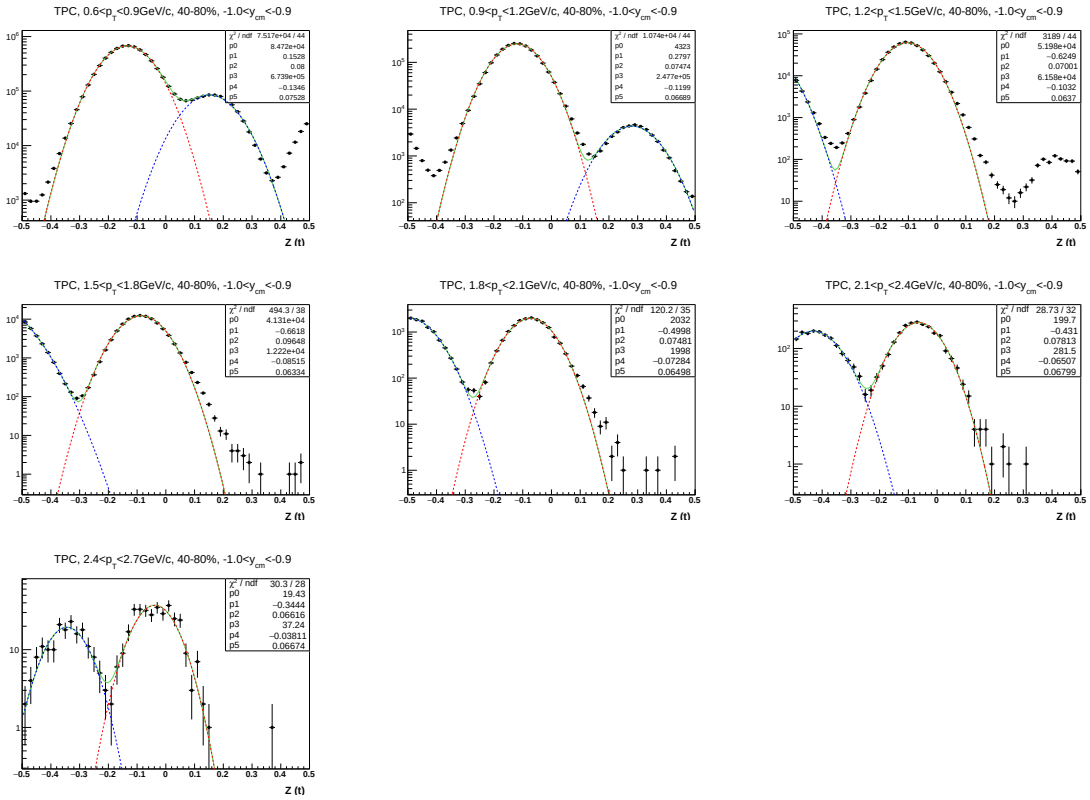

Figure B.12: Z_t and m^2 distributions of triton at $-1.0 < y < -0.9$ rapidity range in 40-80% Au+Au collisions at $\sqrt{s_{\rm NN}} = 3$ GeV.

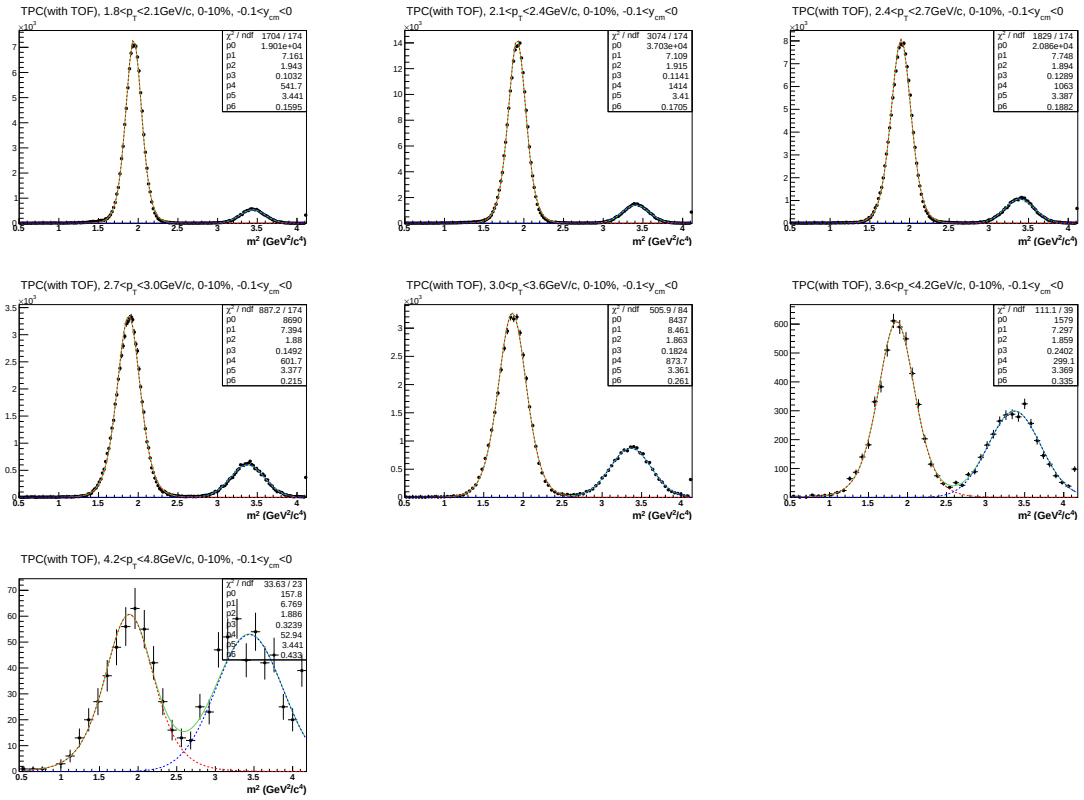

Figure B.13: m^2 distributions of ^{3}He at $-0.1 < y < 0$ rapidity range in 0-10% Au+Au collisions at $\sqrt{s_{\rm NN}} = 3$ GeV.

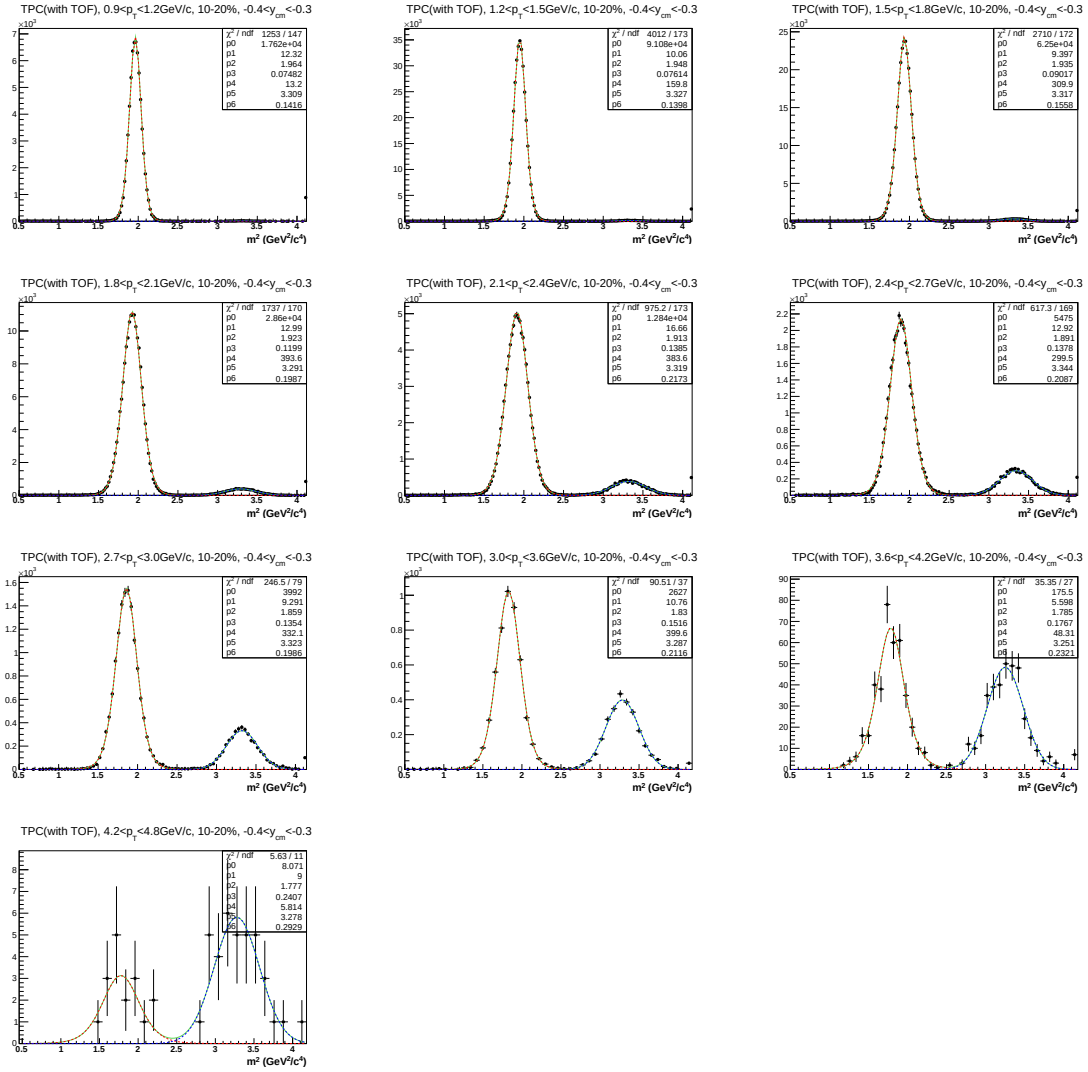

Figure B.14: m^2 distributions of ^{3}He at $-0.4 < y < -0.3$ rapidity range in 10-20% Au+Au collisions at $\sqrt{s_{\rm NN}} = 3$ GeV.

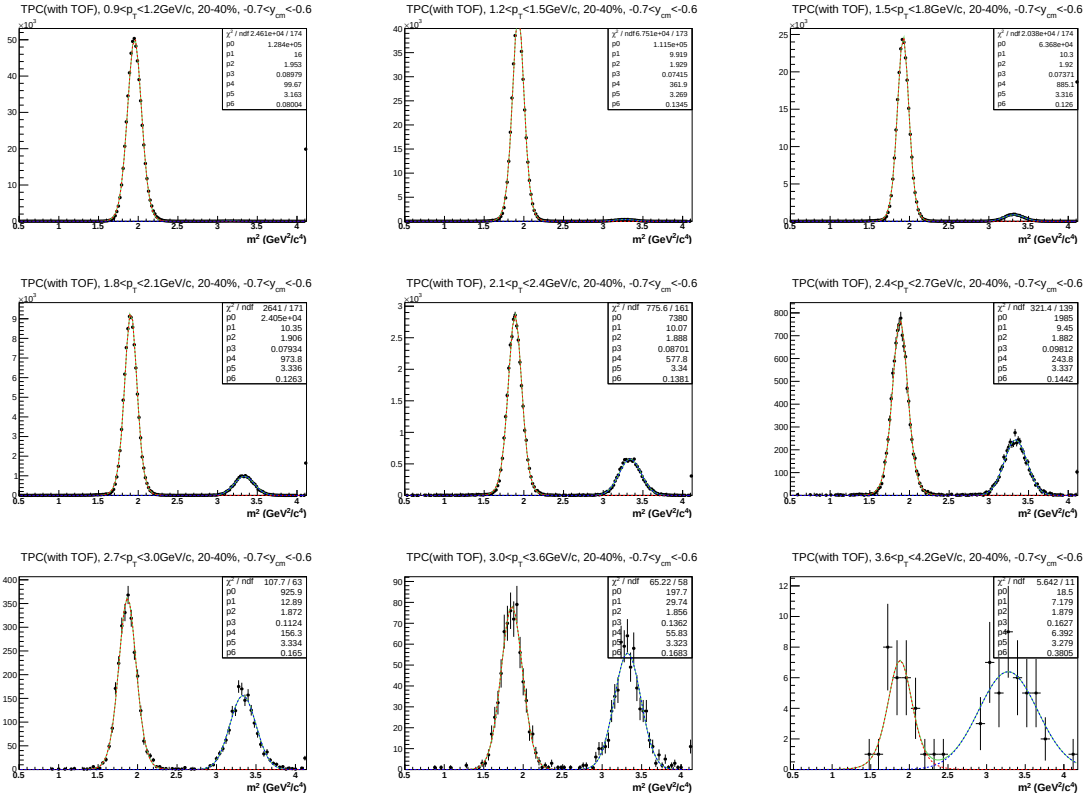

Figure B.15: m^2 distributions of ^{3}He at $-0.7 < y < -0.6$ rapidity range in 20-40% Au+Au collisions at $\sqrt{s_{\rm NN}} = 3$ GeV.

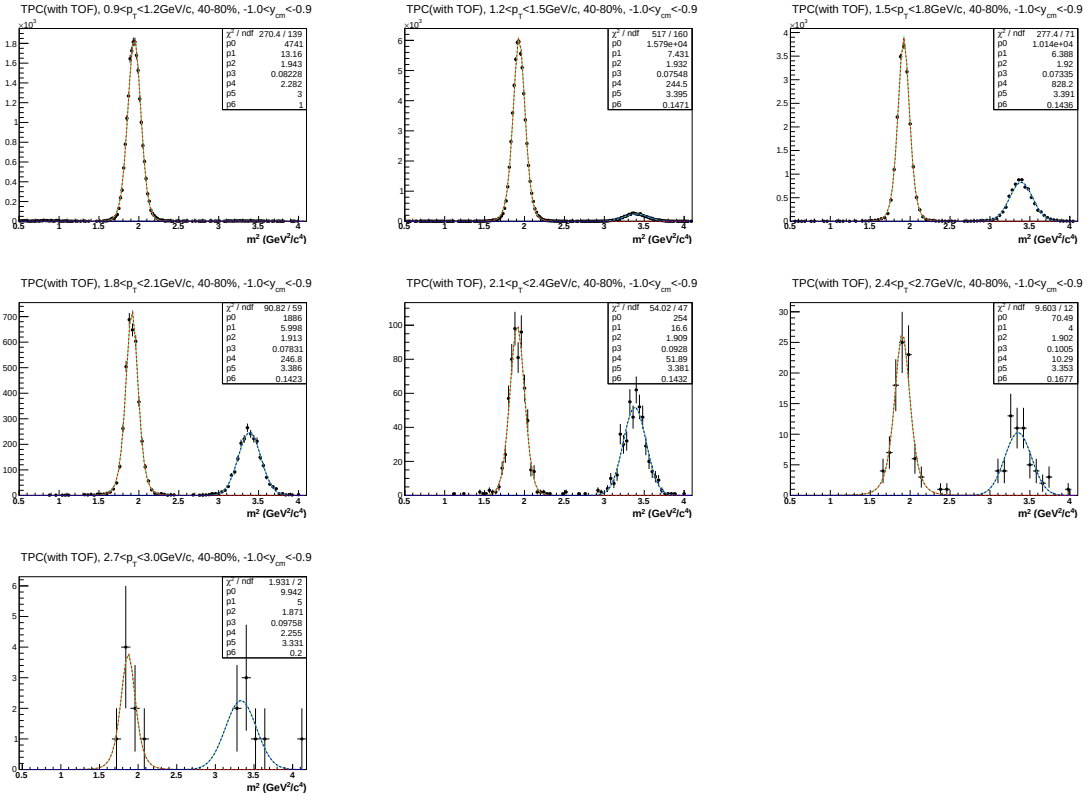

Figure B.16: m^2 distributions of ^{3}He at $-1.0 < y < -0.9$ rapidity range in 40-80% Au+Au collisions at $\sqrt{s_{\rm NN}} = 3$ GeV.

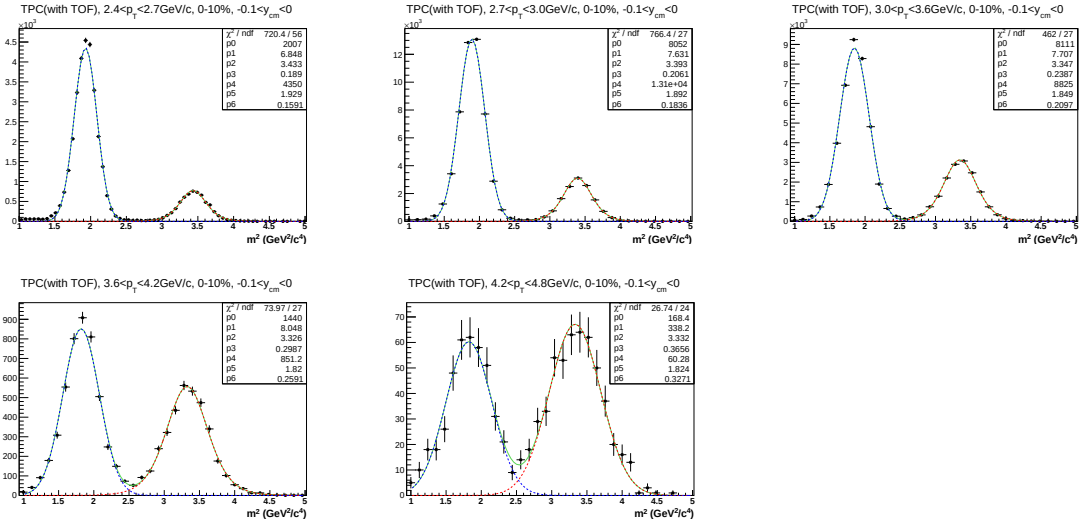

Figure B.17: m^2 distributions of ^{4}He at $-0.1 < y < 0$ rapidity range in 0-10% Au+Au collisions at $\sqrt{s_{\rm NN}} = 3$ GeV.

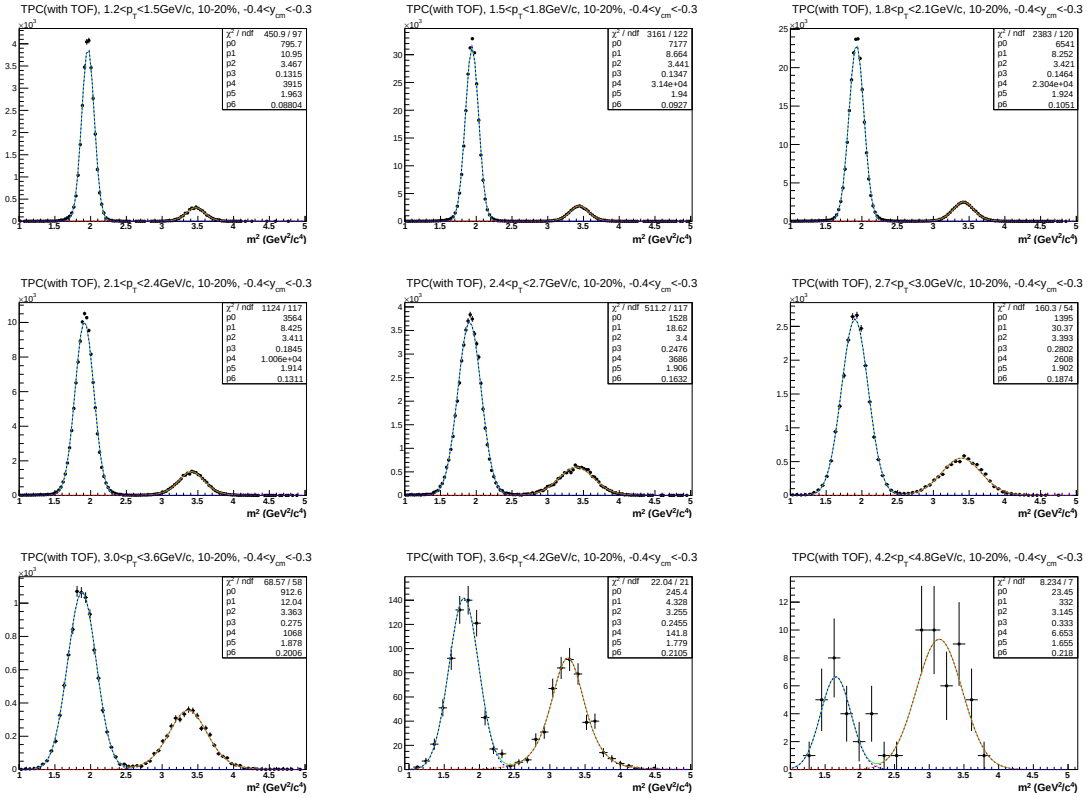

Figure B.18: m^2 distributions of ^{4}He at $-0.4 < y < -0.3$ rapidity range in 10-20% Au+Au collisions at $\sqrt{s_{\rm NN}} = 3$ GeV.

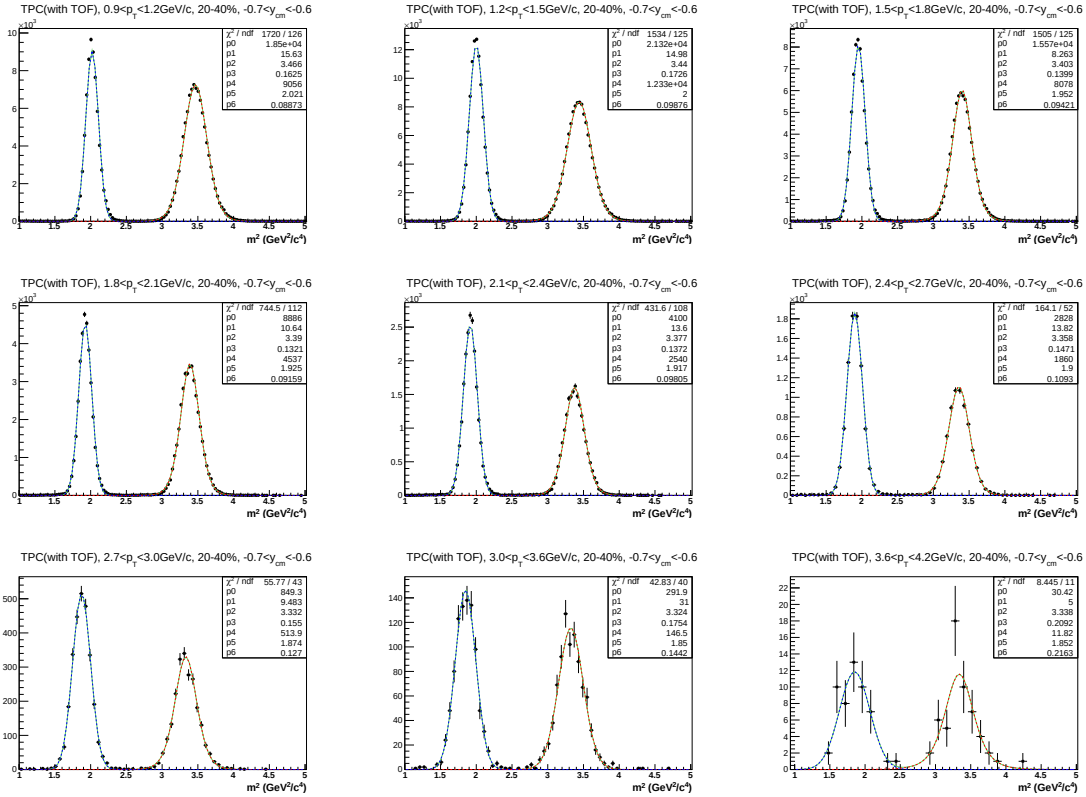

Figure B.19: m^2 distributions of ^{4}He at $-0.7 < y < -0.6$ rapidity range in 20-40% Au+Au collisions at $\sqrt{s_{\rm NN}} = 3$ GeV.

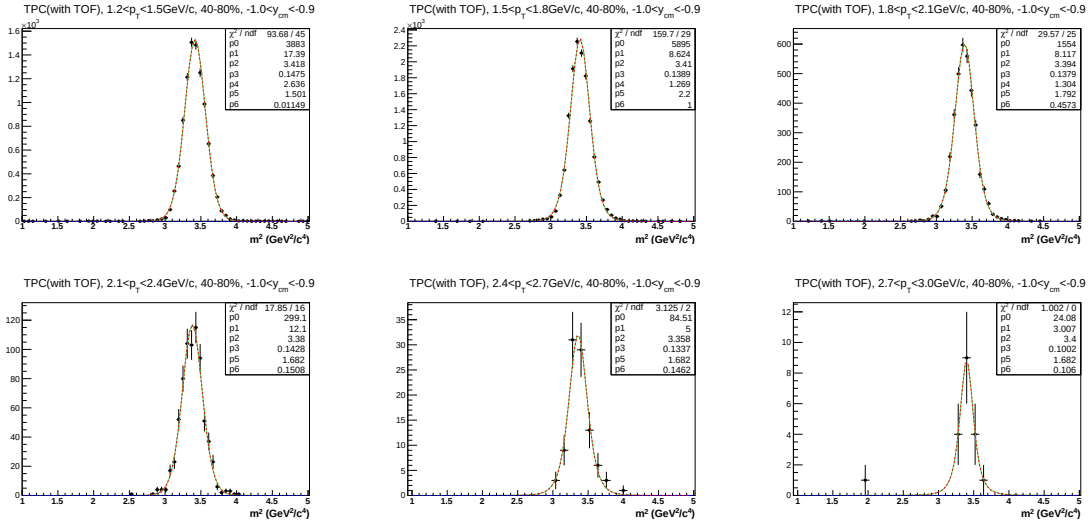

Figure B.20: m^2 distributions of ^{4}He at $-1.0 < y < -0.9$ rapidity range in 40-80% Au+Au collisions at $\sqrt{s_{\rm NN}} = 3$ GeV.

Publications and Presentations

Publications:

1. Production of Protons and Light Nuclei in Au+Au Collisions at $\sqrt{s_{\rm NN}} = 3\,\text{GeV}$ with the STAR Detector
   (STAR Collaboration) arXiv:2311.11020 (2023)

2. Beam Energy Dependence of Triton Production and Yield Ratio ($\mathbf{N}_t \times \mathbf{N}_p/\mathbf{N}_d^2$) in Au+Au Collisions at RHIC
   (STAR Collaboration) *Phys. Rev. Lett.* **130**, 202301 (2023)

3. Measurement of Light Nuclei Production in Heavy-ion Collisions by the STAR experiment
   Hui Liu (for the STAR Collaboration) *Acta Phys. Pol. B Proc. Suppl.* **16**, 1-A148 (2023)

4. Light Nuclei Production in Au+Au Collisions at $\sqrt{s_{\rm NN}} = 3\,\text{GeV}$ from the STAR experiment
   Hui Liu (for the STAR Collaboration) *SciPost Phys. Proc.* **10**, 040 (2022)

5. Effects of centrality fluctuation and deuteron formation on the proton number cumulant in Au+Au collisions at $\sqrt{s_{\rm NN}} = 3\,\text{GeV}$ from the JAM model
   Arghya Chatterjee, Yu Zhang, Hui Liu, Ruiqin Wang, Shu He and Xiaofeng Luo *Chinese Phys. C* **45**, 064003 (2021)

6. Effects of resonance weak decay and hadronic re-scattering on the proton number fluctuations in Au+Au collisions at $\sqrt{s_{\rm NN}} = 5\,\text{GeV}$ from a microscopic hadronic transpo rt (JAM) model
   Yu Zhang, Shu He, Hui Liu, Zhenzhen Yang, and Xiaofeng Luo *Phys. Rev. C* **101**, 034909 (2020)

7. Light Nuclei Production in Au+Au Collisions at $\sqrt{s_{\rm NN}} = 5$ - $200\,\text{GeV}$ from JAM Model
   Hui Liu, Dingwei Zhang, Shu He, Kai-jia Sun, Ning Yu, Xiaofeng Luo *Physics Letters*

B **805**, 135452 (2020)

Presentations:

1. Recent Results of Light (Hyper)Nuclei Production with RHIC-STAR Experiment
   4th Workshop on Anti-Matter, Hyper-Matter and Exotica Production at the LHC (EMMI 2023), February 13-17, 2023
2. Production of Light Nuclei in Au + Au Collisions at $\sqrt{s_{\rm NN}} = 3\,\text{GeV}$ with STAR
   39th CBM Collaboration Meeting, May 16-20, 2022
3. Production of Light Nuclei in Heavy-ion Collisions Measured by RHIC-STAR
   Quark Matter 2022, April 4-10, 2022
4. Light Nuclei Production in Au+Au Collisions at Fixed Target $\sqrt{s_{\rm NN}} = 3\,\text{GeV}$ from STAR
   14th workshop in the series of workshops on QCD phase transition and relativistic heavy-ion physics (QPT 2021), July 26-30, 2021
5. Light Nuclei Production in Au+Au Collisions at Fixed Target $\sqrt{s_{\rm NN}} = 3\,\text{GeV}$ from STAR
   50th International Symposium on Multiparticle Dynamics (ISMD2021), virtual conference, July 12-16, 2021
6. Light Nuclei Production in Au+Au Collisions at Fixed Target $\sqrt{s_{\rm NN}} = 3\,\text{GeV}$ from STAR
   APS April Meeting 2021, April 17–20, 2021
7. Light Nuclei (d, t) Production in Au+Au Collisions at $\sqrt{s_{\rm NN}} = 54.4\,\text{GeV}$ at STAR (Poster)
   Quark Matter 2019, November 4-9, 2019
8. Light Nuclei Production in Au+Au Collisions at $\sqrt{s_{\rm NN}} = 5$ - $200\,\text{GeV}$ from JAM model
   13th workshop in the series of workshops on QCD phase transition and relativistic heavy-ion physics (QPT 2019), August 16-20, 2019

致谢

行文至此，我的求学生涯即将结束，心中感慨万千。回忆起二零一七年只身前来武汉，我对一切充满了好奇，到如今对整个校园的轻车熟路。研究生七年时间，说长不长，说短也不短。在这七年里，我有过迷茫，有过焦虑，有过疲惫，也有过自我怀疑，但更多的是数不尽的欢乐和喜悦。这些点点滴滴充实了我的人生，让我的世界变得奇妙又生动。

在度过整个研究生生活和完成本篇论文的过程中，我要向许多人致以最诚挚的感谢。

首先，最要感谢的是我的导师罗晓峰教授。罗老师是一位年轻有为的学者，他知识渊博，学风严谨，视野宽阔，他的优秀品质深深感染着我。还记得刚入学时，罗老师带课题组的师兄师姐们一起聚餐，在饭桌上他很热心的向我介绍每一位师兄师姐的研究方向和性格特点，整个饭局轻松愉悦，帮助我很快融入了课题组的大家庭。在之后的学习和生活中，罗老师既会关注我们的学业进展，同时也不忘关怀着我们的生活琐事，这让我倍感温暖。在我开始科研分析后，罗老师更是时刻对我进行鼓励，在程序的学习，文献的阅读，数据的分析等各个方面都给了我很大的帮助。我时常在早上醒来查看邮箱时看到罗老师凌晨与 STAR 合作组其他成员交流的邮件，这也深深的影响着我热爱科研的决心。在完成这篇毕业论文上，他更是给我提出了很多的意见和建议，正是在罗老师的悉心指导下，这篇论文才得以完美的呈现。

感谢许怒教授。许老师是一位在科研上一丝不苟，在生活中不拘小节，极具反差感的顶尖学者。初次接触是听许老师的报告，他清晰严谨的逻辑和对科研问题的严格要求给我留下了很深的印象。之后有幸聚餐才发现，许老师虽然在学术上对学生很严厉，生活中却是非常平易近人的。我从许老师身上学到了许多优秀品质，真的很荣幸。

我还要感谢 Norbert Herrmann 教授。Norbert 教授认真负责，许多事情都亲力

亲为。在德国海德堡大学学习期间，Norbert 教授亲自开车带我们去参加学术会议，给我们讲解德国的生活习惯，认真了解我们的科研分析，提出了很多建设性的意见和建议。

感谢华师 STAR 组的各位老师，感谢刘峰老师、施梳苏老师、王亚平老师、李志明老师、裴骅老师，感谢他们在学习和生活上的帮助。感谢海德堡大学的 Ingo 老师在我留学德国期间对我生活和科研上的帮助。感谢喻宁老师对我进行轻核的测量分析上的指导和帮助。感谢在我求学生涯中遇到的每一位老师。

感谢在科研道路上遇到的所有同学。感谢何澍师兄在模型分析上对我的指导。感谢张定伟、张宇师兄带我踏入科研起步阶段，他们在我刚开始做分析时耐心指导，帮助我解决了很多程序上的错误和分析上的问题。感谢米柯，我们在欧洲一起打卡了许多有意思的景点和美食。感谢程甜甜，我们非常投缘，从入学至今虽然几乎没有同行，但是一直在平行线上同步前进，互相鼓励共同进步。感谢实验室一起学习，一起娱乐的同学们，感谢吴锦、周颖洁、周帅、黄仪鸽、徐永聪、綦猷全、沈乾达、刘利珂、刘佐文、金宜宣、姜夏蕾、冯瀚文、陈浏冰、付博洋、朱成豪、张珂豪、汪朝辉、宗英军、陈仕博等。感谢在德期间一起聚餐，一起爬山的伙伴们，感谢张定伟、米柯、程甜甜、路坦、卢鹏忠等，有他们的陪伴，德国的生活变得丰富多彩。

感谢我的室友吕亚楠、李项萌、宋志宏、郭新伟。谢谢你们在我迷茫困惑时给我建议，在我低落难过时给我安慰，在我生日时给我准备惊喜，我会永远记得我们在深夜时一起谈心、一起抢券出去吃好吃的、一起去唱歌，去蹦床馆狂欢，有你们在的宿舍总是充满着欢声笑语。

感谢我的父母，感谢爸爸妈妈的养育之恩。感谢你们的教导和陪伴，感谢你们在我做每一个决定时给予我的鼓励、支持和信任。感谢你们在我远离家乡在外读书期间时时刻刻的关心。感谢我的老公常绍伟，感谢你多年来的陪伴和支持，对我学业上的鼓励和生活上的帮助。

别也何堪，从此花香频入梦；情之如许，当时桂子几经秋。

再次向大家致以诚挚的感谢！

衷心祝愿大家平安喜乐，未来可期。

二零二四年五月于桂子山